

Washington University in St. Louis

Washington University Open Scholarship

Engineering and Applied Science Theses &
Dissertations

McKelvey School of Engineering

Winter 1-15-2021

Theory, Design and Implementation of Energy-Efficient Biotelemetry using Ultrasound Imaging

Sri Harsha Kondapalli
Washington University in St. Louis

Follow this and additional works at: https://openscholarship.wustl.edu/eng_etds



Part of the [Biomedical Engineering and Bioengineering Commons](#), [Communication Commons](#), and the [Electrical and Electronics Commons](#)

Recommended Citation

Kondapalli, Sri Harsha, "Theory, Design and Implementation of Energy-Efficient Biotelemetry using Ultrasound Imaging" (2021). *Engineering and Applied Science Theses & Dissertations*. 610.
https://openscholarship.wustl.edu/eng_etds/610

This Dissertation is brought to you for free and open access by the McKelvey School of Engineering at Washington University Open Scholarship. It has been accepted for inclusion in Engineering and Applied Science Theses & Dissertations by an authorized administrator of Washington University Open Scholarship. For more information, please contact digital@wumail.wustl.edu.

WASHINGTON UNIVERSITY IN ST. LOUIS
School of Engineering and Applied Science
Department of Electrical & Systems Engineering

Dissertation Examination Committee:
Shantanu Chakrabartty, Chair
Raj Jain
Joseph A. O'Sullivan
Neal Patwari
Chuan Wang
Xuan 'Silvia' Zhang

Theory, Design and Implementation of Energy-Efficient
Biotelemetry using Ultrasound Imaging
by
Sri Harsha Kondapalli

A dissertation presented to
The Graduate School
of Washington University in
partial fulfillment of the
requirements for the degree
of Doctor of Philosophy

Jan 2021
Saint Louis, Missouri

© 2021, Sri Harsha Kondapalli

Contents

List of Figures	v
List of Tables	xii
Acknowledgments	xiii
Abstract	xv
1 Introduction	1
1.1 Aims	4
1.2 Structure	5
2 Ultrasound Imaging based Telemetry	7
2.1 Ultrasound Imaging	8
2.2 Ultrasound Imaging-based Telemetry	9
2.2.1 Operation Principle	9
2.2.2 Limits of UIbT	10
2.3 Results	13
2.3.1 Experimental Setup	13
2.3.2 Methods	15
2.3.3 Link Characterization	17
2.3.4 Multi-access	20
2.4 In-vivo Studies	24
2.4.1 Ovine Model Preparation	24
2.4.2 Experimental Results	26
2.5 Discussion	26
2.6 Summary	28
3 Energy Harvesting Cardiac Valvular Perturbations	30
3.1 Introduction	31
3.2 Experimental Methods	34
3.2.1 Ovine model preparation	36
3.2.2 Experimental Setup	37
3.2.3 Data Analysis	37
3.2.4 Energy Harvesting Model	40

3.3	Results	45
3.4	Discussion	48
3.5	Summary	49
4	B-scan Imaging based Telemetry	51
4.1	Operation Principle	52
4.2	Experimental Setup	53
4.2.1	Characterization of the Ultrasound Transmitter Crystal	55
4.2.2	Echoscope and Linear Transducer Array	56
4.2.3	RF triggering, Control and Programming	56
4.2.4	Data Collection and Processing	57
4.2.5	Telemetry Decoding Algorithm	61
4.3	Results	63
4.3.1	Quality Metrics	64
4.3.2	BER Analysis	65
4.3.3	Sensitivity Analysis	65
4.3.4	Telemetry driven by Unregulated Power Source	66
4.4	Discussion	68
4.4.1	Comparison	68
4.4.2	Performance Gain	69
4.4.3	Unregulated Voltage Source	70
4.5	Summary	70
5	Variance-based Computing	71
5.1	Energy Harvesting Sensors	72
5.1.1	Variance-based Processors	73
5.2	VBL based Digital Circuits	74
5.2.1	Variance-based Logic Gates	75
5.3	Measurement Results	76
5.4	Summary	80
6	Variance based Logic	82
6.1	Digital Systems	83
6.1.1	Mean-based Logic	84
6.1.2	Variance-based Logic	84
6.1.3	Mean vs Variance	85
6.2	Energy-per-bit for MBL and VBL	86
6.2.1	Estimation of Probability of Bit Error	86
6.2.2	Estimation of Channel Capacity	88
6.2.3	Estimation of Power Dissipation	88
6.2.4	Figure-of-Merit	89
6.3	Comparison Analysis	89

6.4	Discussion and Summary	93
6.4.1	Hybrid Logic	95
7	High Dimensional VBL	96
7.1	Limits of VBL	96
7.2	Geometric Interpretation of HD-VBL	98
7.3	Numerical Results	101
7.3.1	HD-VBL with one degree-of-freedom	101
7.3.2	HD-VBL with k degrees-of-freedom	108
7.4	Summary	110
8	Conclusion	112
8.1	Thesis Contributions	114
8.2	Future Directions	115
	Bibliography	117
	Vita	126

List of Figures

1.1	Different types of in-vivo devices that require high-speed bio-telemetry links and the proposed approach where commercial ultrasound readers can be used to establish in-vivo communications. <i>Image source for different implant types: Cochlear implants, Neural implants, Retinal prosthesis, Swallow-able Imaging systems, Cardiac implants, Insulin pumps, Footdrop implants and Bone Healing monitors.</i>	2
2.1	(a) Conventional M-scan imaging using a reader that generates interrogation pings and then listens for the reflected echoes to construct a 2-D image. (b) A-scan plot reconstructed at the reader where each of the received pulses indicates the nature and the location of the tissue interface. (c) M-scan reconstructed image, generated by continuous stitching of A-scans.	8
2.2	(a) Example setting where an ultrasound reader Rx receives pulses generated by an implanted crystal Tx to generate an M-scan image shown in (b). The contrast in the image signifies the difference in the received signal levels corresponding to '1' and '0' transmissions. (c) Example settings where multiple crystals Tx1 and Tx2 are simultaneously transmitting and decoded by the reader Rx to produce an M-scan image (d). The M-scan image is post-processed to recover the transmitted data.	9
2.3	(a) Experimental setup used for verifying and characterizing the M-scan telemetry link. (b) Setup showing the piezoelectric crystals implanted inside chicken tissue. (c) Millimeter-scale piezoelectric crystal used for transmission and reception. (d) Measured transmission response with respect to frequency for a piezoelectric crystal immersed in water.	14
2.4	(a) Setup used for measuring the maximum transmitted power P_T where the crystal was modeled using its equivalent load impedance Z_T ; (b) Setup used for measuring the maximum received power P_R where the crystal is modeled as a combination of voltage source driving an impedance Z_T in series with a load resistor R_L	16
2.5	Plot showing the variation in received power with the change in distance between the transmitter and the reader.	16
2.6	Plot showing the variation in the power received at Rx by varying the transmit power at Tx when they are at a distance of 3 cm and 10 cm.	17

2.7	Comparison of the M-scan's, section of A-scan's reconstructed in case of M-scan telemetry considering (a) Water and (b) Chicken as the medium for ultrasound propagation. (c) Sample waveform showing the encoded message in M-scans.	18
2.8	M-scan image reconstructed by the reader, when multiple transmitters are trying to communicate independent data stream which were encoded using Walsh-Hadamard codes, when transmitted power is varied from $3\mu\text{W}$ to $30\mu\text{W}$.	19
2.9	Example of multi-access waveforms based on Walsh-Hadamard coding, where Rx shows the received waveform as a result of simultaneous transmission from different transmitters.	19
2.10	Bar plot showing the signal to noise ratios (SNR) and respective BER measured at the reader, when the three transmitters are sending independent data streams of encoded data at a bitrate of 800 Kbps.	21
2.11	Frequency response of the signal received by Rx when each transmitter (a) Tx1, carrying a signal of 800 KHz which is modulated using 20 KHz (b)Tx2, carrying a signal of 800 KHz which is modulated using 30 KHz (c)Tx3, carrying a signal of 800 KHz which is modulated using 50 KHz, are trying to send their data stream independently.	21
2.12	Sample wave forms corresponding to each transmitter (Tx1, Tx2 and Tx3), in case of transmitting data (a) independently and (b) pairwise. (c),(d) Shows the spectrograms retrieved by the reader for the two FDMA transmissions shown in (a), (b) respectively.	22
2.13	Experimental biotelemetry setup using an adult sheep model: (a) illustration showing piezoelectric crystals implanted in the tricuspid valve and sutured underneath the skin; (b) pictures taken during the surgery and crystal implantation (i)-(ii) and after surgery when the chest cavity has been closed (iii).	24
2.14	M-scan image corresponding to the ovine experiment where the crystal communicates (using a frequency modulation scheme) with the crystal located under-the-skin crystal and when the transmitted power is varied from $2\mu\text{W}$ to $12\mu\text{W}$.	25
2.15	Measured bit error rate, for the data shown in Fig. 2.14, as the transmitted power is varied form 2 to $12\mu\text{W}$.	26
2.16	(a) An A-scan measured by the reader illustrating the possible improvements that can be achieved using channel equalization as highlighted by the transition region shown in (b) where consecutive transmissions alias with each other.	27

3.1	Vision of the proposed research for chronic monitoring of valvular dynamics and (a) overcoming the limitations of existing hard-wired sensing technology. (b) An array of wireless millimeter-scale self-powered implants sutured on the valve can be interrogated using a commercial diagnostic ultrasound scanner. (c) Anatomy of Heart and existing techniques for harvesting heart dynamics, (d) PVDF tube wraps for extracting energy from the outer annulus of the aorta, (e) PZT ribbons for harvesting from the surface of the heart which can power pacemakers (f) Proposed harvesting method to extract energy directly on the valve.	32
3.2	Geometric placement of sonomicrometry crystals and anatomy of tricuspid valve where crystals labeled (1-5), (6-11), (12-14), (15-17) were located around the epicardium, tricuspid annulus, tricuspid leaflet edges and papillary muscle tips of the right ventricle respectively.	34
3.3	(a) 3D reconstruction of the valve using the raw data acquired using the sonomicrometry equipment at different instances showing the crystals' relative movement. (b)- (e) shows the variations of the area enclosed by the polygon formed by the crystals in each plane, respectively. (f) - (h) shows the pressure values LVP RVP and CVP, respectively, and (i) shows the processed ECG data, all collected simultaneously. The peaks are marked manually, indicating the duration of the cardiac cycle.	35
3.4	(a) Sonomicrometry crystal and (b) mechanism for harvesting energy either by replacing the suture loops or by using a piezoelectric suture to attach the crystal to the valve. (c) Suture model and parameters used in the analysis. (d) Cross-section of a valve assuming circular contour and sutured crystals tied to the boundary. At the bottom shows the model a multi-loop piezoelectric suture which reduces the effective local strain level $d\delta$ by a loop factor N . . .	38
3.5	(a) Average velocity profile at each cross section which is obtained by analyzing the data recordings from seven ovine models (black indicating the maximum and red corresponding to zero velocity). (b)-(i) Estimated change in radius, velocity, current and power on the leaflet edges based on the data collected before and after inducing tricuspid-regurgitation (TR).	39
3.6	(a)-(b) shows the variations in power values estimated on each contour across the seven datasets (ovine sheep models) before and after inducing TR respectively (assuming PZT as the material of suture). Similarly (c)-(d) shows the variations for the case of PVDF suture.	41
3.7	Power profile across the tricuspid valve showing the variations, in the normalized power, with respect to time. The power levels change rapidly with crystals located at different locations harvesting maximum power at different time-instants.	44
3.8	Flexible silver-coated PVDF sheet as a potential candidate for constructing piezoelectric sutures.	48

4.1	(a) Principle of M-scan telemetry as reported in 2; (b) Illustration of a typical M-scan image when the data is being transmitted using ON-OFF signaling. (c) BER corresponding to the M-scan telemetry link as reported in 2 when the transmit power is varied from $1\mu\text{W}$ to $12\mu\text{W}$. (d) Principle of the proposed B-scan telemetry. (e) Illustration of a typical B-scan image showing the presence of transmitted data in a 2D cross-section as well as across several B-scan frames. (f) Anticipated improvement in SNR (highlighted by star) for B-scan telemetry compared to M-scan telemetry scheme when operated around beam-angle of 0.1 radians ($\approx 5^\circ$)	52
4.2	(a) Illustration of the experimental setup used to verify and quantify the performance of B-scan telemetry in a water transmission medium. A linear transducer array is driven by (b) an echoscope which is used to acquire B-scan images which are then post-processed on a (c) computer; (d) Picture of the water-bath highlighting the interrogation depth and the relative orientation of the imager and the implant; (e) The prototype of the ultrasound transmitter implemented using a TI CC1310 board and enclosed in a sealed waterproof container. (f) RF module is used for remote programming of the submerged ultrasound.	54
4.3	Measured S_{11} characteristics of the ultrasound transmitter crystal shown in the inset.	55
4.4	Illustration of the B-scan image transformation steps using a (a) template imaging stub where the original B-scan image (b) is transformed pixel-wise into Cartesian coordinates (c); (d) Difference image recovered by high-pass filtering the B-scan image frames; (e) Pixel intensity distributions estimated for a given frame at different instances of time. (f) Anticipated change in pixel intensity distributions in the presence and absence of transmission signal. . .	57
4.5	(a) Sample B-scan image frame when the transmitter is OFF and the corresponding transformed image (b) after filtering and the (c) column-wise mean intensity vector \bar{I} ; (d) Sample B-scan image frame when the transmitter is ON and the corresponding transformed image (e) after filtering and the (f) column-wise mean intensity vector \bar{I}	58
4.6	(a)-(c) Pixel intensity distributions corresponding to different image patches (R_1, R_2, R_3) when the transmitter is OFF and (R'_1, R'_2, R'_3) when the transmitter is ON.	59
4.7	High-pass filtered B-scan image frames measured at different magnitudes of transmitted power.	60
4.8	Estimated mean and std. deviation for an image patch for different levels of transmitted power.	61
4.9	Estimated BER when the transmitted power is varied from $10 - 700$ nW. Inset highlights two operating regions ($1-20$ nW and 100nW) where sensitivity analysis has been performed.	62

4.10	Sensitivity analysis in the low BER region where the transmitted power $P_T = 101.5 \text{ nW}$: (a) Mean and std. deviation values of the image patches; (b) the estimated BER when the magnitude of the transmitted pulsed is varied in increments of 1.2 mV-12 mV.	63
4.11	Sensitivity analysis in the low BER region where the transmitted power $P_T = 0 \text{ nW}$: (a) Mean and std. deviation values of the image patches; (b) the estimated BER when the magnitude of the transmitted pulsed is varied in increments of 1.2 mV-120 mV.	64
4.12	Emulation of the ultrasound transmitter driven by an unregulated power source using (a) programmable DAC and a PWM module; (b) Comparison of estimated transmit power levels for the regulated and the unregulated case; (c) Mean, standard deviation and BER measured for levels of transmit power for the unregulated case; (d) Comparison of the BER for the regulated and the unregulated case for different values of V_{max}	67
5.1	(a) Conventional approach where energy is accumulated before the processor and communication modules are activated;(b) AC/RF based logic where the processor is directly driven by the transducer's AC signal.	72
5.2	(a) Logic representation for both conventional and AC coupled logic; (b) proposed variance based logic representation; (c) Waveforms of the signal observed at the input and output of an VBL based NOT gate.	73
5.3	(a) Implementation of a generic logic gate as a combination of measurement and transformation modules. (b)Schematic of a NOT logic gate using a conventional approach – formed using circuit for (c) measuring the signal mean and (d) transforming the output signal based on the mean. (e) Equivalent implementation of a variance-based NOT gate where (f) and (g) show the corresponding variance measurement and transformation modules.	77
5.4	Micrograph of the fabricated chip in a $0.5 \mu\text{m}$ CMOS process.	77
5.5	(a)Power source (Pwr), (b) Input signal (V_{in}) and (c)-(d) Measured output response of a VBL-based NOT gate for different values of $V_{control}$	79
5.6	Measured oscillation frequency of a 3-stage VBL ring oscillator when the frequency of power source is varied from 40 KHz to 100 KHz.	80
5.7	Simulation results of a 4 bit johnson counter using: (a) conventional logic gates; and (b) using VBL based gates.	81
6.1	Statistical representation of binary logic states '0' and '1' using (a) Mean-based Logic (MBL) and (b) Varianc-based Logic (VBL).	83
6.2	The process of logic transition corresponding to (a) MBL and (b) VBL. . .	85
6.3	Numerical estimated FOM (energy dissipated per bit) corresponding to MBL and VBL for different values of V_{th} and σ_1	90

6.4	(a) Statistical distributions and thresholds corresponding to the MBL operating at the 4.35KT per bit fundamental limit; and (b) VBL operating at sub-KT per bit fundamental limit.	90
6.5	Comparison of numerically estimated information capacity C as a function of the average probability of error p_{avg} , corresponding to MBL and VBL and for different values of V_{th} and σ_1	92
6.6	Rationale for a hybrid logic that combines MBL and VBL - (a) plot showing regions where VBL (or MBL) yields a higher SNR compared to MBL (or VBL) with 'A' being the transition point between the two logic topologies; (b) plot showing the variation in the average probability of error p_{avg} for different values of σ_1 with 'A' being the transition point to switch between MBL and VBL.	94
6.7	Transition between VBL to MBL in an energy-scavenging system.	94
7.1	Comparison of mean-based logic (MBL) and variance-based logic (VBL) representations using (a) a standard communication system model and an AWGN channel. (b) For one-dimensional MBL, the source PDF is encoded using two Dirac-delta functions located at two logic states (\mathbf{X}) 0 and 1. The receiver differentiates the two MBL levels using a decoding boundary θ that separates the PDF corresponding to the output of the AWGN channel (\mathbf{Y}). (c) For one-dimensional VBL the input logic levels are mapped into PDFs with low(0) and high(1) variances. The receiver then differentiates between the VBL levels using a decoding boundary ($\pm\theta$) that are located at the tails of the output PDFs.	99
7.2	(a) Generalization of MBL and VBL to two and three dimensions. For high-dimensional MBL (HD-MBL) the decoding hyperplane cuts through the volume of the overlapping probability density functions (PDFs), whereas for HD-VBL, the decoding boundaries lie on the surface of the overlapping high-dimensional PDFs. Note that the overlap between the PDFs determines the bit-error-rate (BER) for each representation.	100
7.3	Estimation of capacity and BER for VBL representation with a threshold-based decoder. Decision rule for estimating the probability of correct detection (p_d) is provided by the bounding cylinders ($\mathbf{T}_1, \mathbf{T}_2$).	102
7.4	(a) BER estimation in terms of a two-fold hypothesis testing based on a Chi-square distribution with degree of freedom 1. (b) Verification of analytical expression derived in equation. 7.3 for $BER_1 (= 1 - p_d)$ with Monte-Carlo simulations for a different number of dimensions (D) and parameters (SNR, θ). (c) Estimated channel capacity as a function of D in log scale. (d) Classic $BER_1 - E_b/N_0$ plot for the case of VBL with one degree-of-freedom, and comparison is made with respect to MBL_{LB}	103

7.5	Extension to the case of general HD-VBL with variable degrees-of-freedom (a) Estimation of the p_d^k using two-fold hypothesis testing for a 100-dimensional VBL representation with degrees-of-freedom $k=3$. (b) Verification of analytical BER expressions derived in equation. 7.3,7.9 with Monte-Carlo simulations for different parameter values (SNR, θ).	105
7.6	Extension to the case of general HD-VBL with variable degrees-of-freedom (a) Estimation of the p_d^k using two-fold hypothesis testing for a 100-dimensional VBL representation with degrees-of-freedom $k=10$. (b) Verification of analytical BER expressions derived in equation. 7.3,7.9 with Monte-Carlo simulations for different parameter values (SNR, θ).	105
7.7	Energy-per-bit ($EbN0$) estimated as defined in equation. 7.8 vs BER plots for the case of HD-VBL with degrees-of-freedom $k=3$ and interpolated lower bounds (VBL Bound).	106
7.8	Energy-per-bit ($Eb/N0$) estimated as defined in equation. 7.8 vs BER plots for the case of HD-VBL with degrees-of-freedom $k=10$ and interpolated lower bounds (VBL Bound).	106

List of Tables

1.1	Approximate implantation depth and telemetry rates for different implants [1]	3
2.1	Definition of parameters and approximate values for a chicken tissue	11
2.2	Reflection coefficient at different tissue interfaces and estimated minimum power that needs to be transmitted by the piezoelectric crystal	11
2.3	Specifications of the piezoelectric crystals.	13
2.4	Experimental conditions used in measurements.	15
3.1	Piezoelectric properties and parameters used in the suture model.	43
3.2	Maximum and average estimated power that can be harvested at different annular planes, under different conditions using PZT	45
3.3	Maximum and average estimated power that can be harvested at different annular planes, under different conditions using PVDF	46
4.1	Comparison of this work with previous related approaches in terms of transmit power and BER.	69

Acknowledgments

I sincerely thank my advisor Prof. Shantanu Chakrabartty for his continued support and guidance. I cherish those countless hours spent brainstorming ideas, discussing fundamental research questions, editing research papers, and conversations shared during long car rides. I also thank my friends, who helped me along the way and made my stay in St. Louis feel like home. I thank my parents, akka, bavagaru, and all my family members for being my strength and encouragement. I thank all department faculty and staff members from Electrical and Systems Engineering for providing a cordial environment on campus. I thank Prof. Xuan Silvia Zhang, who helped me kick start my research journey. I also thank Prof. Joseph O Sullivan, Prof. Neal Patwari, Prof. Chuan Wang, and Prof. Raj Jain for agreeing to be part of my dissertation committee. I extend my sincere regards to the funding agencies (NSF: CSR-1405273, CNS-1646380 and NIH: 1R21AR075242-01) and Washington University in St Louis for supporting me financially through my Ph.D. journey.

Sri Harsha Kondapalli

Washington University in Saint Louis

Jan 2021

Dedicated to my small family

ABSTRACT OF THE DISSERTATION

Theory, Design and Implementation of Energy-Efficient
Biotelemetry using Ultrasound Imaging

by

Sri Harsha Kondapalli

Doctor of Philosophy in Electrical Engineering

Washington University in St. Louis, 2021

Professor Shantanu Chakrabartty, Chair

This dissertation investigates the fundamental limits of energy dissipation in establishing a communication link with implantable medical devices using ultrasound imaging-based biotelemetry.

Ultrasound imaging technology has undergone a revolution during the last decade due to two primary innovations: advances in ultrasonic transducers that can operate over a broad range of frequencies and progresses in high-speed, high-resolution analog-to-digital converters and signal processors. Existing clinical and FDA approved bench-top ultrasound systems can generate real-time high-resolution images at frame rates as high as 10000 frames per second. On the other end of the spectrum, portable and hand-held ultrasound systems can generate high-speed real-time scans, widely used for diagnostic imaging in non-clinical environments. This dissertation's fundamental hypothesis is to leverage the massive data acquisition and

computational bandwidth afforded on these devices to establish energy-efficient bio-telemetry links with multiple in-vivo implanted devices.

In the first part of the dissertation, I investigate using a commercial off-the-shelf (COTS) diagnostic ultrasound reader to achieve reliable in-vivo wireless telemetry with millimeter-sized piezoelectric crystal transducers. I propose multi-access biotelemetry methods in which several of these crystals simultaneously transmit the data using conventional modulation and coding schemes. I validated the feasibility of in-vivo operation using two piezoelectric crystals tethered to the tricuspid valve and the skin's surface in a live ovine model. I demonstrated data rates close to 800 Kbps while consuming microwatts of power even in the presence of respiratory and cardiac motion artifacts.

In the second part of the dissertation, I investigate the feasibility of energy harvesting from cardiac valvular perturbations to self-power the wireless implantable device. In this study, I explored using piezoelectric sutures implanted in proximity to the valvular regions compared to the previous studies involving piezoelectric patches or encasings attached to the cardiac or aortic surface to exploit nonlinearity in the valvular dynamics and self-power the implanted device. My study shows that power harvested from different annular planes of the tricuspid valve could range from nano-watts to milli-watts.

In the final part of this dissertation, I investigate beamforming in B-scan ultrasound imaging to further reduce the biotelemetry energy-budget. In this context, I will study variance-based informatics in which the signal representation takes a form of signal variance instead of the signal mean for encoding and decoding. Using a modeling study, I show that compared to the mean-based logic representation, the variance-based representation can theoretically achieve a superior performance trade-off (in terms of energy dissipation) when operating at

fundamental limits imposed by thermal-noise. I will then discuss how to extend variance-based representation to higher signal dimensions. I show that when applying variance-based encoding/decoding to B-scan biotelemetry, the power-dissipation requirements can be reduced to 100 pW even while interrogating from depths greater than 10 cm in a water medium.

Chapter 1

Introduction

Ultrasound imaging technology has undergone a revolution during the last decade due to the availability of transducers that can operate over a broad range of frequencies and the availability of high-speed, high-resolution analog-to-digital converters and digital signal processors. Existing clinical and FDA approved bench-top ultrasound systems can generate real-time high-resolution images at a rate of more than 7000 frames per second [2]. In literature, ultrasound imaging systems with frame rates as high as 10000 frames per second [3], and with very high-resolution [4] [5] has also been reported. On the other end of the spectrum, portable and hand-held ultrasound systems like GE VScan, Siemens P10, Phillips Lumify, and SignosRT (shown in Fig. 1.1) can also generate high-speed real-time scans and has been used for diagnostic imaging in non-clinical environments. The large data acquisition and computational bandwidth on these portable and bench-top ultrasound imaging systems could be leveraged to establish bio-telemetry links that can be used to communicate with multiple in-vivo implanted devices. Examples of implantable devices that require high-bandwidth telemetry links are shown in Fig. 1.1, and their applications range from swallowable imaging systems [6], neural implants [7], cochlear [1], retinal prosthesis devices [8], etc. The typical

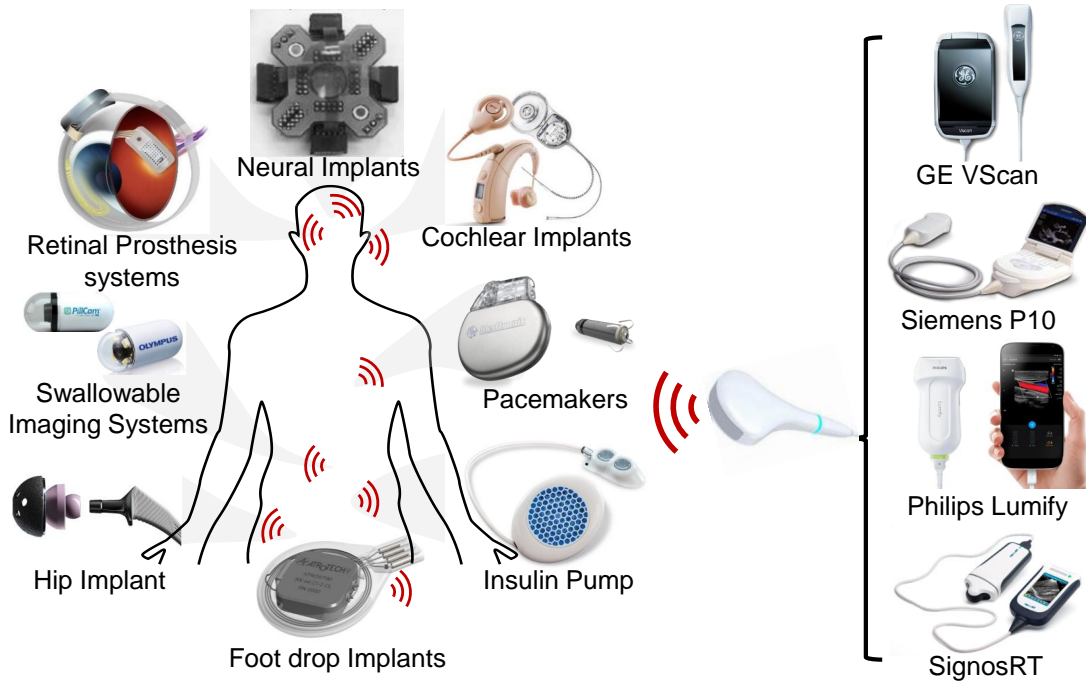


Figure 1.1: Different types of in-vivo devices that require high-speed bio-telemetry links and the proposed approach where commercial ultrasound readers can be used to establish in-vivo communications. *Image source for different implant types: Cochlear implants, Neural implants, Retinal prosthesis, Swallow-able Imaging systems, Cardiac implants, Insulin pumps, Footdrop implants and Bone Healing monitors.*

data-rates for these implants and their respective implantation depths are summarized in Table 1.1.

In literature, radio-frequency (RF) based systems have been proposed for high-speed telemetry [10]. However, traditional wireless technologies (e.g., Wi-Fi, Bluetooth) cannot be scaled to in-vivo applications. The biological tissue is majorly composed of water, which provides more significant attenuation to RF electromagnetic waves. As a consequence, RF waves need to be transmitted at higher power, which constraints the energy budgets at the implanted device. Also, their implantation depths and form-factors are constrained by medical compliance

Table 1.1: Approximate implantation depth and telemetry rates for different implants [1]

Implant	Expected Datarate	Approximate Depth
Retinal Prosthesis	60 fps (2 Mbps)	2-5 cm
Swallow-able Imaging Systems [9]	18 fps (1.2 Mbps)	7-12 cm
Neural Implant	288 Kbps	5-10 cm
Cochlear Implant	100 Kbps	2-5 cm
Cardiac Pacemakers	20 Kbps	2-5 cm
Insulin Pumps	20 Kbps	2-5 cm
Footdrop Implants	10 – 20 Kbps	2-5 cm
Bone Healing Monitors	0.1 – 1 Kbps	2-5 cm

Kbps/Mbps stands for Kilo/Mega bits per second.
fps stands for frames per second.

limits (local Joule heating). For example, an RF telemetry system reported in [11]- [12] was shown to achieve data-rates of 120-450 Kbps for implantation depths less than 2cm.

On the other hand, Ultrasound based telemetry systems can penetrate deeper into biological tissue while operating within the limits of medical compliance and without any side-effects due to long-term exposure [13]. In [14], an ultrasonic telemetry system (form factor of 10 mm) was reported to achieve data-rates of 70-700 Kbps, however, in an ex-vivo environment. Recently, [15] have demonstrated ultrasonic communication data rates of more than 20 Mbps using orthogonal frequency-division multiplexing (OFDM) technique. However, the size of the 5 MHz transducer used in [15] is relatively large for in-vivo implantation. In [16] an ultrasonic backscattering was used to achieve data-rates up to 500Kbps; however, the implantation depths that were reported were less than a cm.

In this research, I investigate the use of commercial off-the-shelf (COTS) diagnostic ultrasound readers to perform wireless telemetry with a millimeter-sized piezoelectric crystal transducer and demonstrate its feasibility as a unique platform technology. I will present my analysis

through a series of experimental and analytical modeling studies that address several challenges concerning telemetry, energy harvesting, and signal detection.

1.1 Aims

Aims are summarized as follows:

Ultrasound Imaging-based Telemetry: I investigate the use of ultrasound imaging systems to build and realize an efficient bio-telemetry system that can enable multi-access with implanted devices located at depths ranging in centimeters. I also investigate its viability using in-vivo studies and estimate the energetics required to power the telemetry front end in the presence of motion artifacts.

Energy Harvesting Cardiac Valvular Perturbations: I investigate the feasibility of harvesting energy from cardiac valvular perturbations for self-powering with a grand vision of demonstrating tether free sonomicrometry sensors.

Variance based Logic: To bridge the gap between the available harvestable power and the telemetry needs, I propose investigating variance-based logic (VBL) that can revisit fundamental limits and provide new insights for designing highly energy-efficient communication and computing systems. In this context, I also explore its extensions to higher dimensions and investigate how some of these results generalize for high dimensional VBL applicable to several other applications.

1.2 Structure

Primarily this dissertation investigates two paradigms of biotelemetry design: chapters 2-4 demonstrate the design and feasibility study on low-power implantable devices and ultrasound imaging-based telemetry platform, while chapters 5-7 detail the study on using variance-based representation schemes for realizing energy-efficient telemetry systems.

Chapter 2 presents a brief overview of ultrasound imaging and the principle of an imaging-based telemetry system. I discuss the limits on the data-rates and communication strategies for both single link and multi-access telemetry. Experimental results are presented for both in-vitro and in-vivo characterization of ultrasound imaging based telemetry using chicken tissue and a live ovine model as a target transmission medium.

Chapter 3 presents the piezoelectric suture model for harvesting energy from cardiac valvular perturbations to self-power the wireless sensors. I describe experimental methods used in gathering data on cardiac valve biomechanics from an ovine model. I provide analysis on estimating harvestable power levels on different annular planes of the tricuspid valve and present insights into sensors' optimal surgical placement.

Chapter 4 presents the B-scan telemetry system's design and implementation and provides experimental results for characterizing the communication link with particular attention to demonstrating sub-nanowatt ultrasonic biotelemetry. I present a case study on using an unregulated power source for modulating the amplitude of the transmission pulse and provide the robustness analysis in the methods used for B-scan telemetry.

Chapter 5 introduces the concept of variance-based logic (VBL) and describes the primary CMOS-based VBL circuit's topology. Using the essential VBL cells, I synthesize a digital

state-machine and demonstrate the benefits of the proposed approach in system latency. I summarize the chapter by providing details about designing a ring oscillator operating with an unregulated power source.

Chapter 6 compares the traditional bi-stable logic representation with variance-based representation and shows that the former can achieve an excellent trade-off when operating at fundamental limits imposed by the thermal noise. Performance metrics in terms of bit-error-rate (BER) and energy per bit (E_b/N_0) are analyzed for both cases, and the results were presented using monte-carlo simulations. I summarize the chapter by highlighting the advantages of variance-based representation.

Chapter 7 presents the system model and geometrical realization of the high dimensional variance-based (HDVBL) system and validates its performance using monte-carlo simulations.

The summary of this research work is presented in chapter 8. Key contributions of this dissertation are highlighted, and suggestions for future work are also presented.

Chapter 2

Ultrasound Imaging based Telemetry

This chapter investigates the use of commercially off the shelf ultrasound imagers for high-speed bio-telemetry with millimeter-sized piezoelectric crystals. These crystals are used to generate echoes that are larger in magnitude than the acoustic reflections generated at the tissue-tissue interfaces. These echoes are captured using a standard ultrasound imager, and the data is extracted using image deconvolution and deblurring algorithms. We also demonstrate the use of this method for multi-access telemetry, where several piezoelectric crystals simultaneously transmit the data using different modulation techniques. Using a live ovine model, we demonstrate that an under-the-skin piezoelectric crystal can maintain a high-speed telemetry link with another crystal implanted in the tricuspid valve in the presence of respiratory and cardiac motion artifacts. The technology could therefore enable real-time transmission of information from different monitoring devices implanted in-vivo.

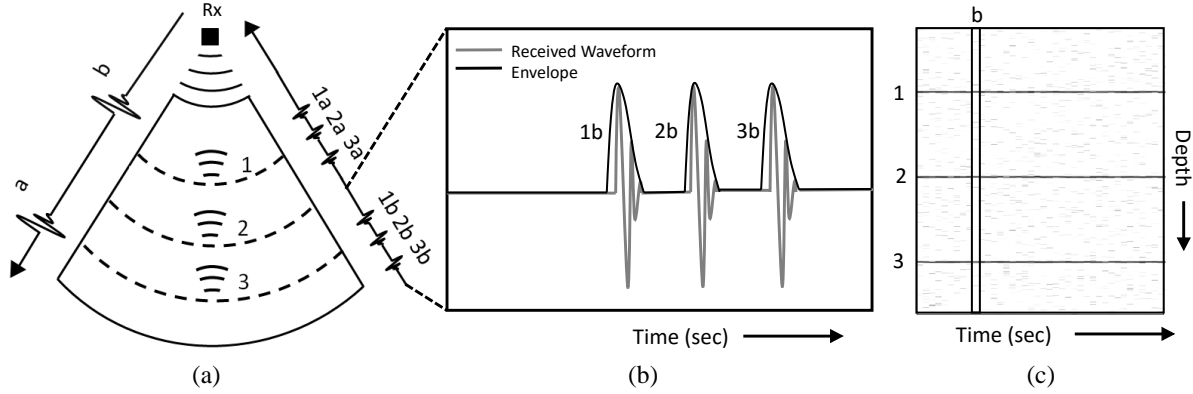


Figure 2.1: (a) Conventional M-scan imaging using a reader that generates interrogation pings and then listens for the reflected echoes to construct a 2-D image. (b) A-scan plot reconstructed at the reader where each of the received pulses indicates the nature and the location of the tissue interface. (c) M-scan reconstructed image, generated by continuous stitching of A-scans.

2.1 Ultrasound Imaging

The principle of M-scan ultrasound imaging is based on the phenomenon of pulse-echo, which is illustrated in Fig. 2.1. In a conventional imaging mode, the interrogation pulse is reflected from the tissue boundaries (labeled as '1', '2', and '3') due to a mismatch in their respective acoustic impedance. After generating an interrogation pulses (labeled as 'a' and 'b'), the ultrasound reader listens for reflected pulses (labeled as '1a-3a' and '1b-3b'). The time-of-arrival of the pulse indicates the depth of the interface. The magnitude of received pulses indicates the tissue boundary's nature (for example, muscle-blood or fat-muscle interface). A sample waveform of the received signal is shown in Fig. 2.1 (b) where the information has been mapped onto a grey-scale pixel value resulting in a single frame of an M-scan image. Information corresponding to multiple interrogation pulses are fused over time to generate a composite M-scan, as shown in Fig. 2.1(c).

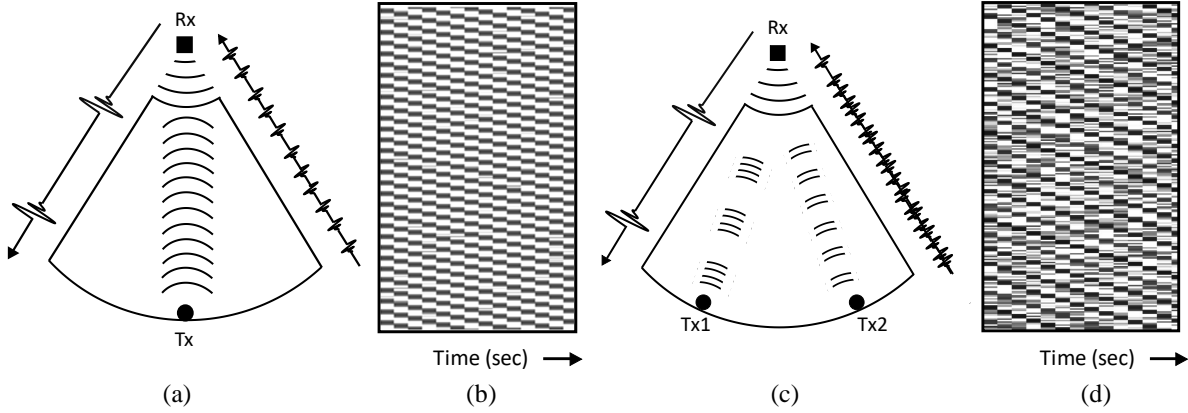


Figure 2.2: (a) Example setting where an ultrasound reader Rx receives pulses generated by an implanted crystal Tx to generate an M-scan image shown in (b). The contrast in the image signifies the difference in the received signal levels corresponding to '1' and '0' transmissions. (c) Example settings where multiple crystals Tx1 and Tx2 are simultaneously transmitting and decoded by the reader Rx to produce an M-scan image (d). The M-scan image is post-processed to recover the transmitted data.

2.2 Ultrasound Imaging-based Telemetry

2.2.1 Operation Principle

In this chapter, we exploit the process of M-scan imaging to perform telemetry with implanted ultrasonic transmitters. The principle relies on mimicking the reflected echoes using implanted piezoelectric crystals (Tx, Tx1, or Tx2), as shown in Fig. 2.2 (a),(c). As long as the magnitude of the pulses from the transmitter crystal is larger than the echoes generated in response to the ultrasonic interrogation pulses, the M-scan reader should detect and decode the data encoded in the transmitted pulses. Note that the emitted pulses' frequency falls within the bandwidth of the interrogator. A synthetic M-scan image generated using the received pulses is illustrated in Fig. 2.2 (b). Similarly, when multiple crystals are emitting pulses based on their respective data streams (as shown in Fig. 2.2 (c)), the reader generates a composite M-scan image as shown in Fig. 2.2(d). The proposed M-scan imaging framework

also supports telemetry with multiple crystals using multi-access techniques reported in standard communication literature [17] like frequency division multi-access (FDMA) or code division multi-access (CDMA). In this chapter, we have used on-off-keying (OOK) for data modulation and Walsh-Hadamard codes for demonstrating multi-access communication. An example of multi-access communication protocol is illustrated in Fig. 2.2 (d) for two crystals, where each of the crystals uses its respective FDMA based orthogonal code ('00001111' for crystal 1, '00110011' for crystal 2) to encode bit '1'. When transmitting bit '0', both the crystals do not emit any echoes. Note that the code's size determines the number of simultaneous telemetry links established with the M-scan reader and determines each crystal's maximum data-rate. Also, for the proposed telemetry method, the ultrasound reader's interrogation pulses do not play a significant role. However, in our previous work [18], we demonstrated that the interrogation pulses could be used to power the telemetry interface remotely. While this attribute is essential in realizing a fully integrated, remotely powered wireless device, our research focuses only on investigating M-scan-based ultrasound telemetry limits.

2.2.2 Limits of UIbT

From a theoretical point-of-view, there exist fundamental limits on the data-rates that can be achieved using M-scan-based telemetry. One factor that will determine the theoretical upper limit on data-rate is the maximum allowable heat dissipation in biological tissues. In literature, this limit is reported to be 7.2 mW/mm^2 [19] and any telemetry interface has to ensure that its overall power-dissipation is below this limit. Another factor that will determine the upper-limit is the channel point spread function's nature, which will allow the reader to differentiate between two independent echoes. Note that prior knowledge of the

Table 2.1: Definition of parameters and approximate values for a chicken tissue

Parameter	Definition	Example (Chicken Tissue)
f	Frequency	$1.3MHz$
d	Propagation Distance	$3cm$
P_o	Initial Pressure	$1 (N/m^2)$
α	Attenuation Parameter	0.086×10^2 $neper/(mMHz^{-\beta})$
β	Attenuation Coefficient	1.5

Table 2.2: Reflection coefficient at different tissue interfaces and estimated minimum power that needs to be transmitted by the piezoelectric crystal

Tissue Interface	η	$P_{min}(dB)$
Muscle-Blood	0.023	-7.485
Bone-Muscle	0.637	-0.903
Fat-Muscle	0.109	-4.433
Bone-Fat	0.697	-0.721
Skin-Blood	0.015	-8.347
Skin-Muscle	0.039	-6.489

channel response could apply channel equalization techniques and recover overlapping echoes. While this will not be the main focus of this research, we will illustrate channel equalization potential in section 2.5.

The minimum transmit power determines the lower-limit on the data-rate, which in turn is determined by the following two factors: (a) ultrasonic attenuation characteristics of the in-vivo medium; and by (b) the noise in the medium. The attenuation characteristics of ultrasound in-vivo has been extensively studied [20,21] and is typically modeled in terms of

pressure level (Pr) as a function of depth d and frequency f according to

$$Pr(f, d) = P_0 e^{-\alpha f^\beta d} \quad (2.1)$$

where P_0 is pressure level generated at the surface of the ultrasonic transmitter and α and β are constants which are determined by transmission media. Thus, based on the equation 2.1, the transmitter has to generate sufficient pressure to overcome channel attenuation such that a minimum detectable pressure level is received at the receiver. Table 2.1 shows typical values of the attenuation parameters obtained using a chicken tissue phantom which are consistent earlier works [22]. A first-order calculation using these parameters illustrates that at 1.3 MHz frequency, ultrasound attenuates only by 10.83 dB at a depth of 3cm. In comparison, a 1 MHz radio-frequency wave attenuates by more than 50 dB for the same depth [23].

The second factor which determines the minimum transmitted power is the level of channel noise. For the proposed M-scan based telemetry, the primary source of noise is the echoes (due to specular reflection and scattering of incident interrogation pulse) generated at the tissue interface due to acoustic impedance discontinuities. Note that changes in pressure level due to thermal vibrations will be negligible compared to the echoes' magnitude and have not been considered. Table 2.2 shows the reflection coefficient (η) corresponding to different tissue interfaces and is determined by the ratio between the intensities of the reflected and incident acoustic wave [20].

Combining equation 2.1 with the respective reflection coefficient of the tissue interface located at depth d , the minimum transmitted power (P_{min}) can be estimated (relative to the interrogation power) as

$$P_{min}(dB) = 2 \log \eta - \alpha f^\beta d \quad (2.2)$$

Table 2.3: Specifications of the piezoelectric crystals.

Parameter	Specification
Resonant Frequency	$1.3MHz$
Material	PZT-5H Teflon coated
diameter	$1.0mm$
Crystal Capacitance	$120 - 250pF$
Bandwidth	$\approx 200KHz$
Maximum Input Voltage	around $1kV$

Table 2.2 summarizes the minimum transmission power estimated using equation 2.2 for a frequency of 1.3MHz and for a depth of 3cm. While these approximate values represent the lower limit of power in dB, it only considers the specular reflections (not considering the scattering and representing the lowest upper bound) for a single tissue interface. In reality, a tissue can be more complex and may need much higher power to overcome echoes' artifacts.

2.3 Results

2.3.1 Experimental Setup

Omnidirectional piezoelectric crystals were purchased from Sonomicrometrics Inc and used in our experiments for implementing both the single element M-scan ultrasound reader ('Rx') and the implantable transmitters ('Tx 1-3'). The piezoelectric crystals shown in Fig. 2.3 (c) are made with PZT-5H ceramic material and are coated using Teflon to ensure that the crystal is biocompatible and can be chronically implanted. The impedance characteristics and the crystals' frequency response were first measured using an Omics Bode 100 vector network analyzer. Fig. 2.3 (d) shows the measured frequency response when the crystal is

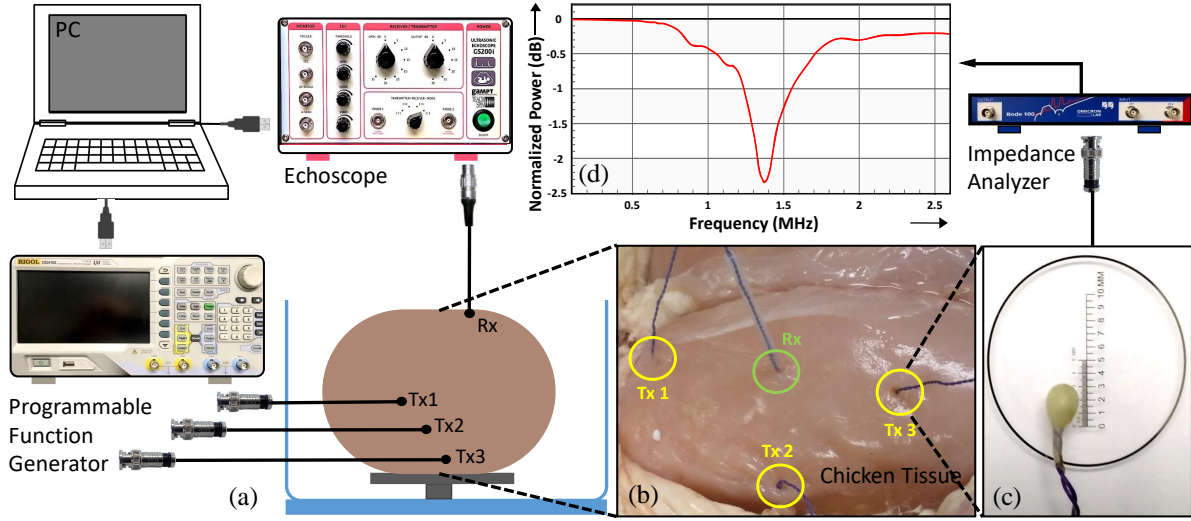


Figure 2.3: (a) Experimental setup used for verifying and characterizing the M-scan telemetry link. (b) Setup showing the piezoelectric crystals implanted inside chicken tissue. (c) Millimeter-scale piezoelectric crystal used for transmission and reception. (d) Measured transmission response with respect to frequency for a piezoelectric crystal immersed in water.

inserted in a water medium and Table 2.3 summarizes the specifications of the piezoelectric crystal. The ultrasound reader was implemented using a programmable GS200 echoscope (from gaMPT, Germany), and the ultrasonic transmitter was implemented using function generators (Tektronix DG4102, 100 MHz Arbitrary Waveform Generator), as shown in Fig. 2.3. M-scans from the echoscope were acquired using a personal computer using GS-Echoview software, an application provided by gaMPT mbH. Table 2.4 summarizes different measured parameters like transmitted power, peak to peak voltage applied to the piezo crystals, and settings of the echoscope used for the experiments reported in this chapter. In particular, 'depth' in Table 2.4 refers to the distance of implanted crystals from the surface of the skin. Product of 'Frame size' (acquisition length) and 'sampling frequency' determines the number of rows in the scan reconstructed as illustrated in Fig. 2.1 (c). 'Frame rate' refers to pulse repetition frequency, which determines the number of columns generated per second in the reconstructed image.

Table 2.4: Experimental conditions used in measurements.

Parameter	Definition
Transmitted Power	$0 - 18\mu W$
Pulse amplitude (V_{PP})	1-20 V
Pulse frequency	800 KHz
Shape	Square Pulse
depth	$3cm - 12cm$
R_x Gain	15 dB
Frame size	10- 100 μsec
Speed of sound	$1460m/sec$
sampling frequency	$10MHz - 100MHz$
Frame rate	2.5 KHz

2.3.2 Methods

This chapter has verified the proposed M-scan based telemetry using chicken tissue and live ovine model as two mediums for ultrasound propagation. The transmitted and received power at each of the crystals implanted in-vivo were measured using a source and a load resistor, respectively, as shown in Fig. 2.4 (a)-(b). P_T and P_R show the equations for the time average measure of transmitted and received power at the crystal.

The acquisition of the M-scan data was performed using an echoscope, connected to the ultrasound reader 'Rx,' preset to low transmission gain and high receive gain, which ensures the reduction of interference due to echoes generated during M-scan acquisition. Demodulating and decoding the received data from the acquired ultrasound image (M-scan) were performed using MATLAB. The post-processing involved rasterizing the 2D intensity matrix into a 1D array, which is inverse of the 2D image formation process described in Fig. 2.1. A rectangular window is then applied to the rasterized 1D array, and the windowed value is compared against a threshold to determine reconstructed bit '1' or '0'. For the results presented in this chapter,

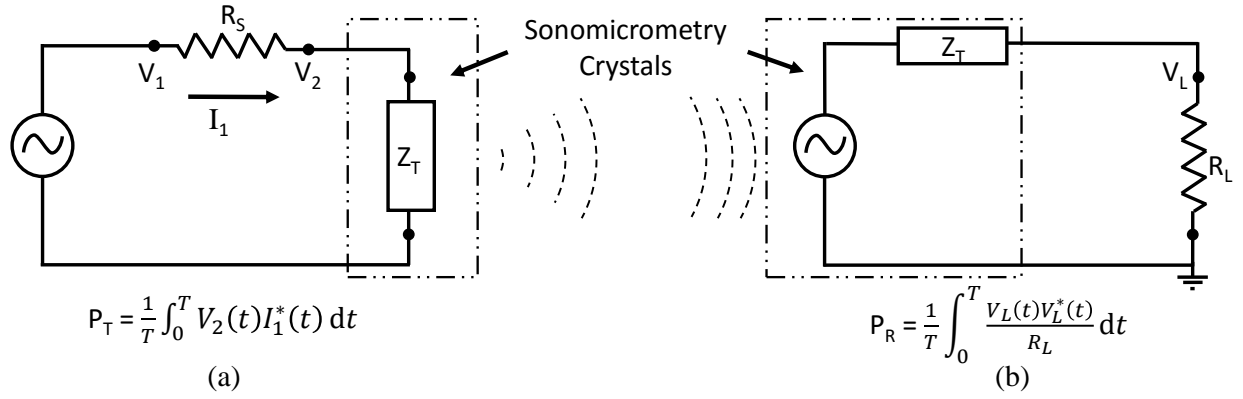


Figure 2.4: (a) Setup used for measuring the maximum transmitted power P_T where the crystal was modeled using its equivalent load impedance Z_T ; (b) Setup used for measuring the maximum received power P_R where the crystal is modeled as a combination of voltage source driving an impedance Z_T in series with a load resistor R_L .

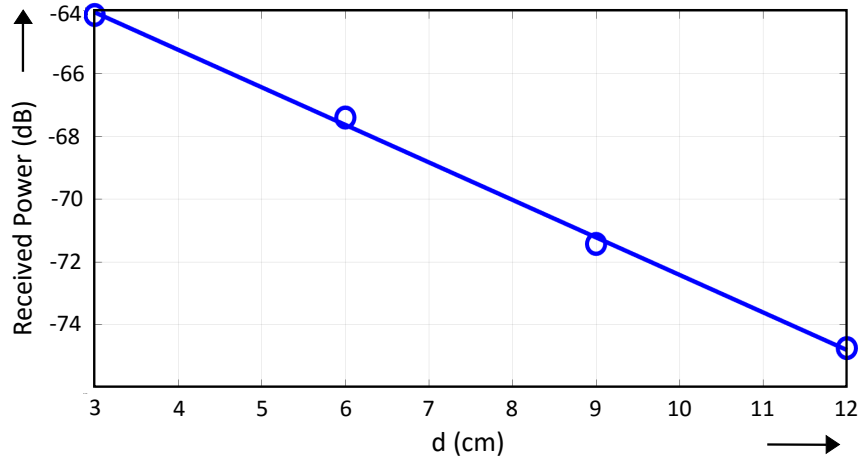


Figure 2.5: Plot showing the variation in received power with the change in distance between the transmitter and the reader.

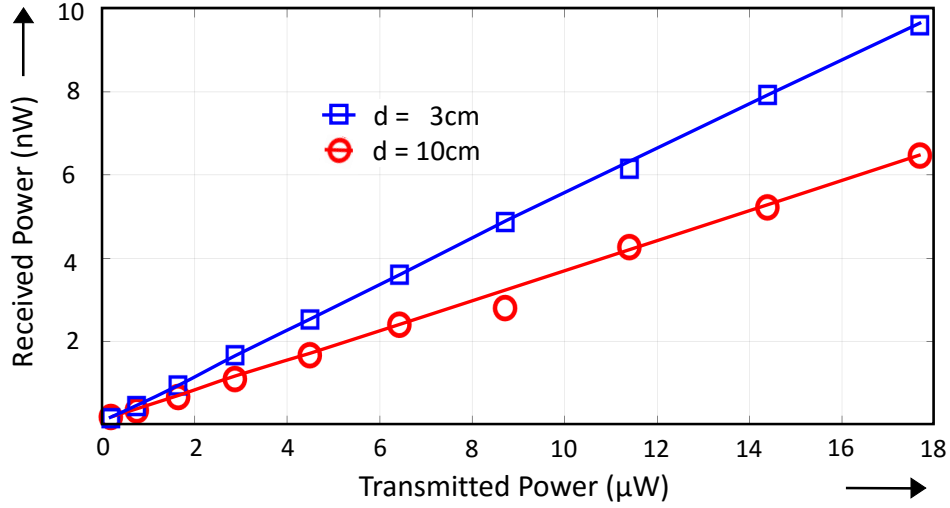


Figure 2.6: Plot showing the variation in the power received at Rx by varying the transmit power at Tx when they are at a distance of 3 cm and 10 cm.

each M-scan comprises a million pixels, and the window size varied from 10-20 pixels based on the transmitter's pulse-frequency. The reconstructed bit sequence was then compared with the transmitted bit sequence to estimate the bit-error-rate (BER). In multi-access communication, the reconstructed bits are compared with each of the encoded bit sequences, and the information from each transmitter is recovered independently.

2.3.3 Link Characterization

The first set of experiments uses a phantom constructed using chicken breast tissue, as shown in Fig. 2.3, where the transmitter crystals are labeled as 'Tx1-3,' and the reader crystal is labeled as 'Rx.' While the transmitter crystal was implanted/sutured inside the tissue at different depths, the reader crystal was mechanically stabilized by suturing the probe underneath the top tissue layer. In this manner, any acoustic impedance artifacts due to the crystal's attachment to the tissue surface were alleviated. The configuration of the function generators driving each of the transmission crystals is summarized in Table 2.4,

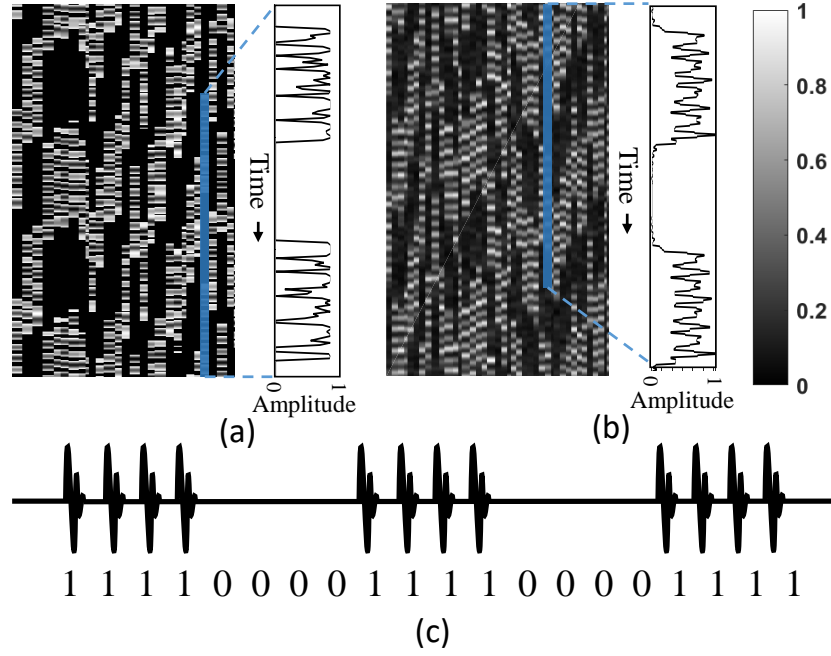


Figure 2.7: Comparison of the M-scan's, section of A-scan's reconstructed in case of M-scan telemetry considering (a) Water and (b) Chicken as the medium for ultrasound propagation. (c) Sample waveform showing the encoded message in M-scans.

where the maximum transmission power has been measured using the sensing circuit shown in Fig. 2.4(a). In the first experiment, the distance between the transmitter crystal and the reader was varied. The attenuation in the tissue was measured (using the sensing circuit shown in Fig. 2.4(b)) and is shown in Fig. 2.5 and confirms to the log-linear attenuation model given by equation 2.1. Fig 2.6 shows the measured results where the received power (to a $50\text{ K}\Omega$ resistive load) is plotted against different levels of transmitted power for two implantation depths (3 cm and 10 cm). The measured results show that for an upper-limit (7.2 mW/mm^2) on the power dissipation on the transmitter, the receiver can receive power levels of 500 nW/mm^2 and $1\text{ }\mu\text{W/mm}^2$ for respective implantation depths of 10 cm and 3 cm. These results are aligned with the experiments that were previously reported in [18] where we demonstrated that useful power could be harvested from interrogation pulses generated from an ultrasound reader.

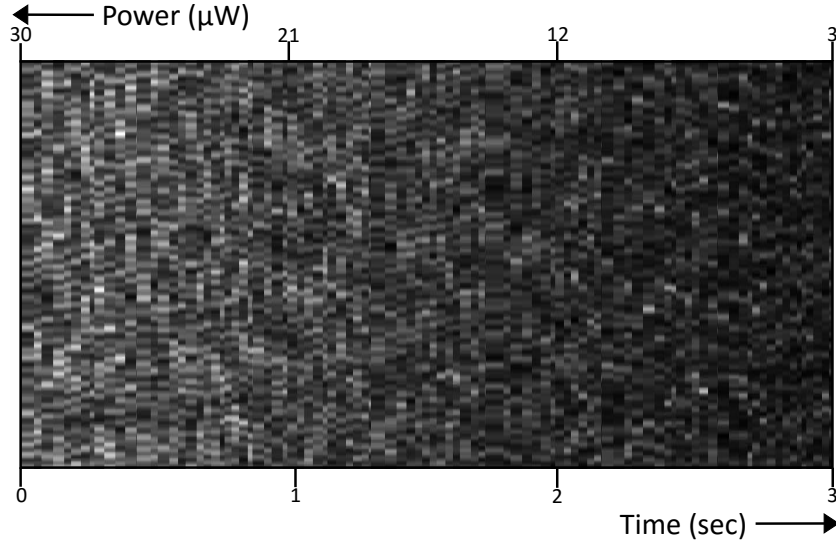


Figure 2.8: M-scan image reconstructed by the reader, when multiple transmitters are trying to communicate independent data stream which were encoded using Walsh-Hadamard codes, when transmitted power is varied from $3\mu\text{W}$ to $30\mu\text{W}$.

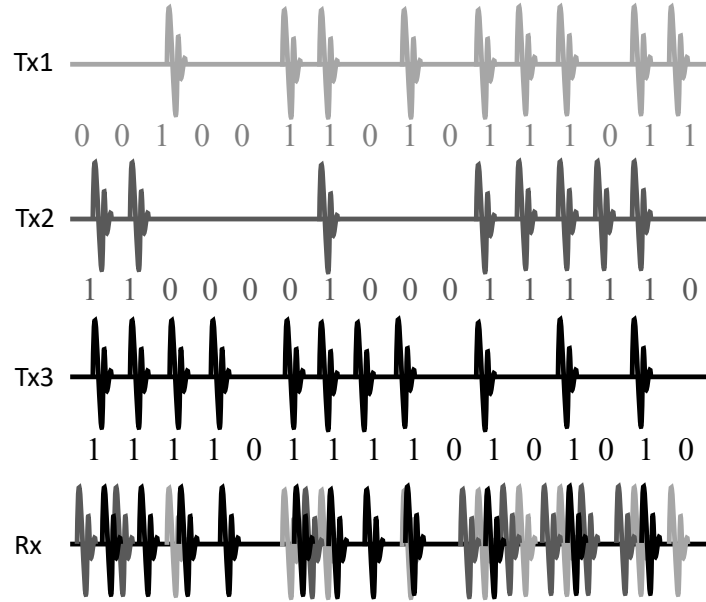


Figure 2.9: Example of multi-access waveforms based on Walsh-Hadamard coding, where Rx shows the received waveform as a result of simultaneous transmission from different transmitters.

The next set of experiments were designed to show the feasibility of ON-OFF keying using standard M-scan based telemetry. Fig. 2.7(a) and (b) show the M-scan images and the corresponding section of their A-scans for water and chicken tissue as the transmission medium, respectively. The encoded data-stream shown in Fig. 2.7(c) where '1' and '0' are encoded using ON-OFF keying. Each of the M-scan images clearly shows the modulation effect due to ON-OFF keying. However, the A-scans show that the spread around the peak is narrower in water medium as compared to the spreads when the medium is chicken tissue. The overlap between the consecutive '1's arise due to channel effects inside the tissue and also due to the pre-processing used for M-scan image generation by the echoscope. Note that for post-processing, each of the A-scan frames in the M-scan image needs to be arranged in a form of 1D array and any error in aligning these frames by the echoscope would lead to an increase in bit error-rates. Also, the limited buffer size on the echoscope will affect the quality of the M-scan which in-turn will affect the quality of the communication link. Higher sampling rate at the reader leads to better quality of the M-scan and longer frame-size leads to accommodating more number of receiver packets which improves the quality of communication link. Hence the choice of frame-size and the sampling frequency, considering a constant buffer size at the reader, becomes crucial in M-scan based telemetry. For all the results presented in this chapter, the frame-size has been chosen to be 100 μ sec and the sampling frequency has been set to 10 MHz.

2.3.4 Multi-access

Multi-access telemetry is demonstrated using three transmitters communicating with the ultrasound reader at the surface of the tissue. In the first set of multi-access experiments, a 16-bit Walsh-Hadamard orthogonal code is used to encode the transmitted data, similar

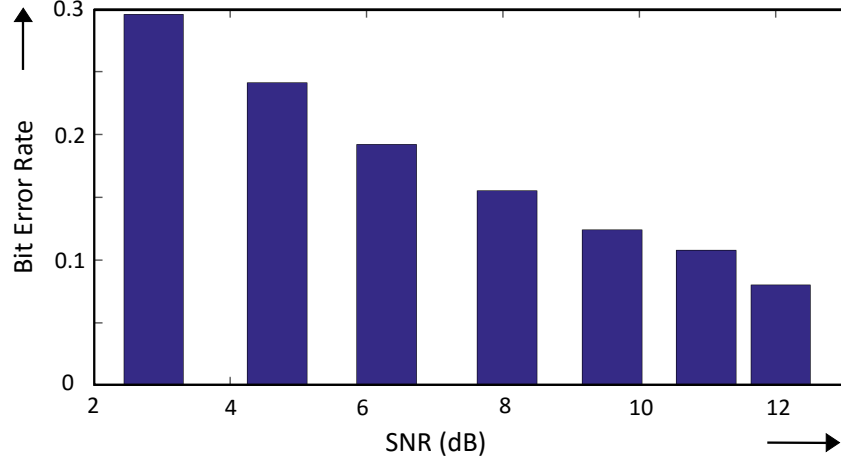


Figure 2.10: Bar plot showing the signal to noise ratios (SNR) and respective BER measured at the reader, when the three transmitters are sending independent data streams of encoded data at a bitrate of 800 Kbps.

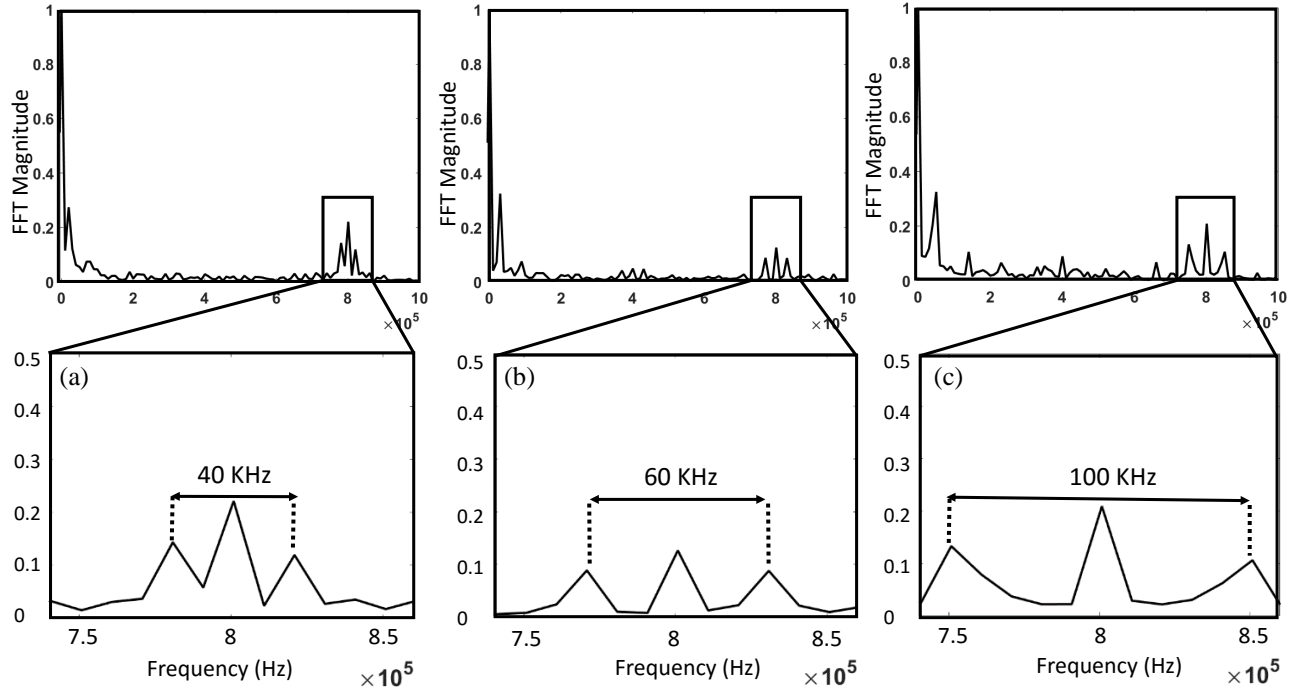


Figure 2.11: Frequency response of the signal received by Rx when each transmitter (a) Tx1, carrying a signal of 800 KHz which is modulated using 20 KHz (b)Tx2, carrying a signal of 800 KHz which is modulated using 30 KHz (c)Tx3, carrying a signal of 800 KHz which is modulated using 50 KHz, are trying to send their data stream independently.

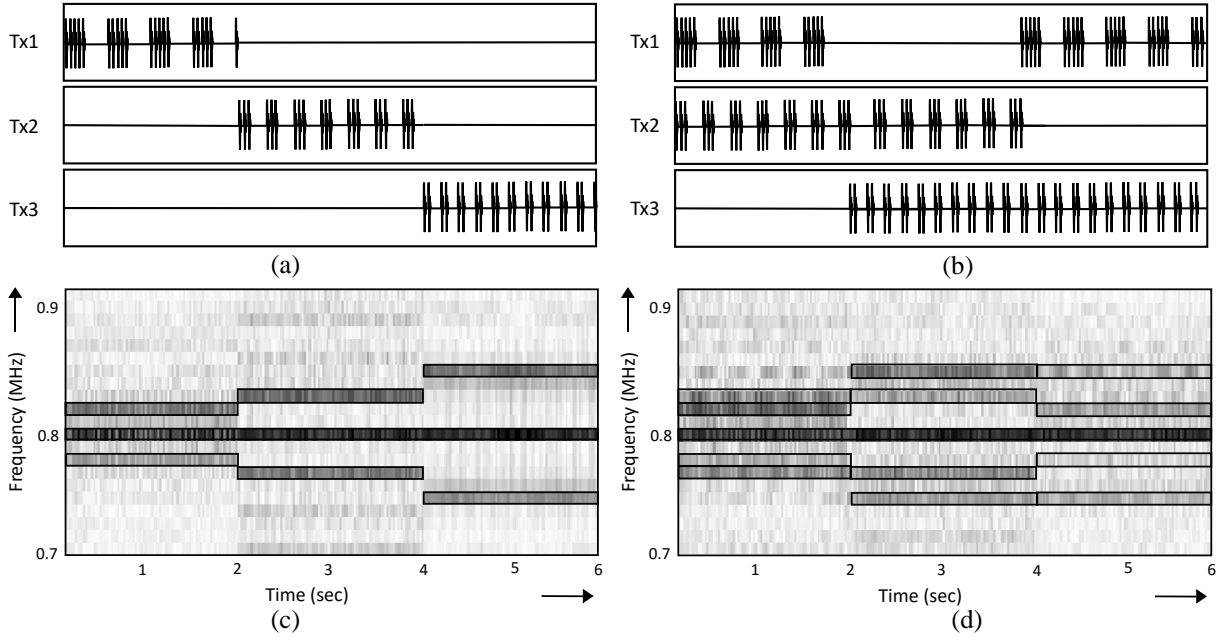


Figure 2.12: Sample wave forms corresponding to each transmitter (Tx1, Tx2 and Tx3), in case of transmitting data (a) independently and (b) pairwise. (c),(d) Shows the spectrograms retrieved by the reader for the two FDMA transmissions shown in (a), (b) respectively.

to that of a spread-spectrum based communication system. This approach is similar to the previously reported methods [14, 24], where a combination of pulse position modulation and pseudo-random codes of variable length are used to provide multi-access using ultrasound. We used a fixed length for this work, unique 16 bit codes to represent '0' and '1' at each of the transmitters. As shown in Fig. 2.9, the received data can be demodulated by correlating the received signal with the known set of code bits. This method not only gives us information about the transmitted data but can also be used to synchronize the start of a data frame. A sample M-scan image is shown in Fig. 2.8 for the condition when all the transmitters are simultaneously transmitting and their respective transmission power is reduced from $30\mu\text{W}$ to $3\mu\text{W}$. The M-scan image is then post-processed and demodulated using the orthogonal codes to recover the bitstreams corresponding to each transmitter. The cumulative system BER for a crystal implantation depth of 3 cm is shown in Fig. 2.10. Like any multi-access approach,

the system BER decreases with the increase in the transmitted power. The lower-limit of detection is determined by the quantization noise (finite resolution) of the M-scan reader.

In the next set of experiments, the transmitters are programmed to implement a multi-access scheme similar to frequency division multiple access (FDMA). The equivalent carrier frequency in FDMA was implemented using a periodic train of ultrasonic pulses at a frequency of 800 kHz. Each of the transmitters then used a periodic signal (at frequencies 20 kHz, 30 kHz, and 50 kHz) to modulate the carrier frequency. For this experiment, the Fig. 2.11 shows the spectrum obtained after post-processing the M-scan images for conditions where only one of the crystals was transmitting. The measured results clearly show spectral peaks at frequencies at 800 ± 20 kHz, 800 ± 30 kHz, and 800 ± 50 kHz, each corresponding to the transmission frequencies for the different crystals. Fig. 2.11(c)-(d) show the spectrogram plots for an FDMA based transmission corresponding to two cases: (a) when only one of the crystals is transmitting in sequence (Tx1, Tx2, and Tx3); and (b) when all the crystals are simultaneously transmitting. In both Figures 2.11(c)-(d), the presence of the carrier signal can be discerned by the dark line at the center of the spectrogram. For each transmitter, the bit '1' is encoded by an increase in energy in the frequency band allocated to the transmitter, as shown in Fig. 2.11(c)-(d). For the multi-access transmission, where two of the crystals are simultaneously transmitting, the respective bits can be decoded by independently measuring the energy present in the frequency band allocated to the crystal. This experiment demonstrates the use of FDMA based multi-access communications using M-scan telemetry. Even though all the experiments presented here are based on a data-rate of 800 Kbps, we have verified communication rates up to 1.3 Mbps. In the case of multi-access communication, we have verified combined data-rates up to 2.4 Mbps. Note that FDMA encoding constitutes a particular case of spread-spectrum communication, and hence its BER performance will be similar to that of the results shown in Fig. 2.12.

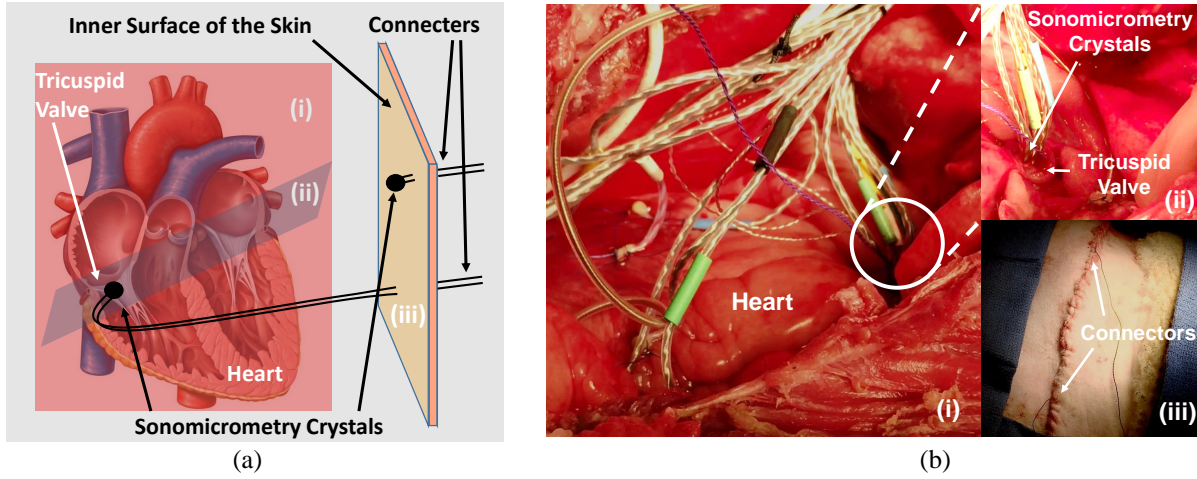


Figure 2.13: Experimental biotelemetry setup using an adult sheep model: (a) illustration showing piezoelectric crystals implanted in the tricuspid valve and sutured underneath the skin; (b) pictures taken during the surgery and crystal implantation (i)-(ii) and after surgery when the chest cavity has been closed (iii).

2.4 In-vivo Studies

In the final set of experiments, the proposed M-scan telemetry was verified in a live ovine model. The objective was to verify that a reliable communication link can be established when the piezoelectric crystal is implanted in the tricuspid valve, as illustrated in Fig. 2.13(a), and is continuously subjected to motion artifacts (movement of the valve in this specific case). The surgical procedure for implanting the crystal was performed on an adult male sheep in a fully equipped and accredited animal facility at West Michigan Regional Laboratory, which is a part of the Spectrum Health Delivery System.

2.4.1 Ovine Model Preparation

The animal was studied in an acute, open-chest fashion to facilitate validation of the proposed telemetry technique. Briefly, the animal was sedated, intubated, and put under general

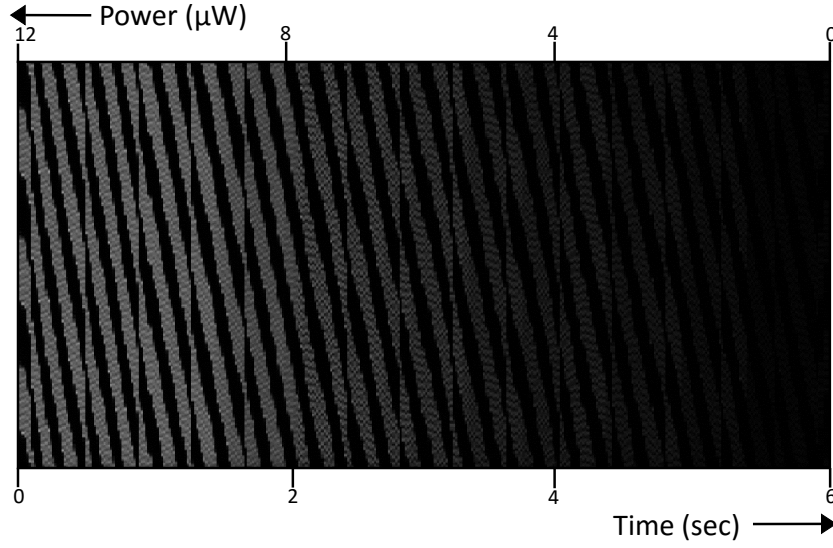


Figure 2.14: M-scan image corresponding to the ovine experiment where the crystal communicates (using a frequency modulation scheme) with the crystal located under-the-skin crystal and when the transmitted power is varied from 2 μW to 12 μW .

anesthesia; a right thoracotomy was performed as surgical access to the heart. After full heparinization, cardiopulmonary bypass was established via the right carotid artery and the right internal jugular vein. While on cardiopulmonary bypass and with the heart beating, both cava was snared, and the right atrium was opened to expose the tricuspid valve. A piezoelectric crystal used for telemetry was sewn on the tricuspid annulus, and another reader crystal was sutured underneath the skin as illustrated in Fig. 2.13 (a). Subsequently, the right atrium was closed, and the animal was weaned from cardiopulmonary bypass and stable hemodynamics achieved. Fig. 2.13 (b) (i) shows the opened chest cavity with the exposed heart and the cables associated with the piezoelectric crystal sewn on the tricuspid annulus. Fig. 2.13 (b) (iii) shows the closed chest cavity post-surgery with crystal connectors (data acquisition ports) located on the surface of the skin. The reader crystal was sutured underneath the skin's surface and the approximate distance to the implanted crystal is about 10 cm.

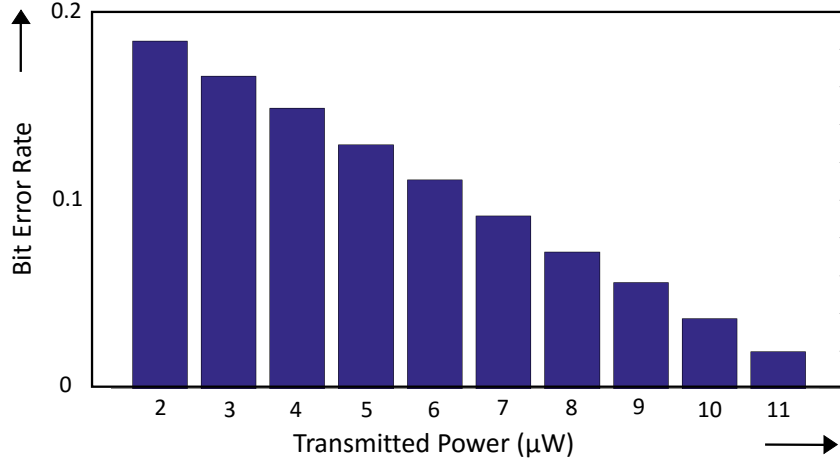


Figure 2.15: Measured bit error rate, for the data shown in Fig. 2.14, as the transmitted power is varied from 2 to 12 μW .

2.4.2 Experimental Results

Fig. 2.14 shows the M-scan retrieved by the reader when transmit power is varied from 0 to 12 μW for data rates of 1 Mbps and for a data sequence shown in Fig. 2.7 (c). The recorded M-scan images were used to reconstruct the data-stream and generate BER plots as shown in Fig. 2.15. As expected, the measured results show a monotonic decrease in the error rates with the increase in the transmission power. More importantly, BER rates of 10^{-2} can be achieved at power dissipation levels of only 11 μW which is well within the compliance limits.

2.5 Discussion

Given that the maximum energy dissipated at data-rates of more than 1 Mbps was demonstrated to be well below the compliance limits, there is still room to push telemetry limits using M-scan imaging. The high-frequency piezoelectric crystal could support higher data-rates; however, the attenuation in the tissue will also increase. In this regard, an ultrasound

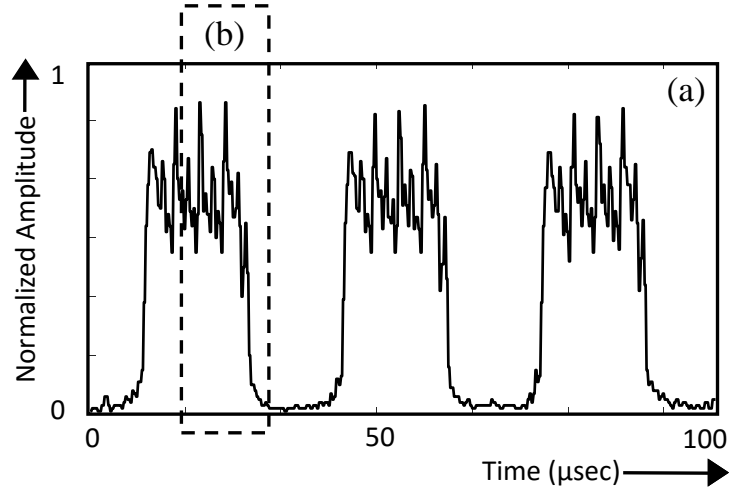


Figure 2.16: (a) An A-scan measured by the reader illustrating the possible improvements that can be achieved using channel equalization as highlighted by the transition region shown in (b) where consecutive transmissions alias with each other.

reader with a sufficient receive gain and low noise-factor could alleviate the effects due to attenuation. Another direction to increase the telemetry rate is by using channel equalization techniques [25] to compensate for overlap between neighboring transmission bits and also to compensate for effects due to multipath. The effect due to attenuation channel can be seen in Fig. 2.16, where the bits '1' are aliased when transmitted in sequence as compared to the case when a sequence of '0's are interspersed in between. Like conventional channel equalization methods, a known preamble sequence would estimate the instantaneous channel impulse response. This would then be used to demodulate the data bits. Note that in M-scan telemetry, the data (multi-access or single) is received as frames of images which can be post-processed using image equalization techniques (similar to channel equalization). Another possible solution to improve the data-rates is to reduce the echoes generated due to interrogation pulses which can be achieved by lowering the transmit power at the Ultrasound reader and increasing the receiver gain to capture a higher resolution ultrasound image of the transmit signal. In terms of BER performance, like any multi-access communication technique, the

error-rates will increase compared to a point-to-point communication link [26]. However, as long as the modulation and coding basis functions are chosen to be orthogonal, the error-rates for different multi-access schemes are approximately the same. The high-channel capacity of the M-scan or B-scan telemetry link could be exploited in alternate ways. For instance, using forward error-correcting (FEC) techniques [27] one can establish reliable telemetry links with implants that are either located further away from the ultrasound imager or with devices implanted inside material with low ultrasonic penetration - for example, implants in tissue surrounded by bone [28]. In such cases, the coding-gain is used to compensate for the signal attenuation, and the entire M-scan image could be treated as a single block-code.

2.6 Summary

This chapter demonstrates that a standard ultrasound reader can perform multi-access telemetry with devices implanted inside the body. Compared to an RF-based telemetry system, ultrasound-based telemetry can penetrate deeper into biological tissue. A millimeter-scale piezoelectric crystal was shown to be capable of high-speed ultrasonic communication links. Even at data rates close to 1 Mbps and implantation depths greater than 10 cm, the BER is estimated to be 10^{-2} which makes this method suitable for most in-vivo sensing applications [29]. Measured power dissipation on sonomicrometry devices was shown to be well below the tissue heating limits, which implies that they could be powered using implanted energy sources or could be powered remotely. In [30] we showed that up to a few microwatts of energy can be harvested from the interrogation pulses generated by a standard ultrasonic reader. In the future, our goal will be to use the piezoelectric crystal to harvest energy from the interrogation pulses to energize the sensing and telemetry functions.

To summarize, this telemetry technique generates an M-scan containing the transmitted information and saves it as a bitmap image, and later can be demodulated using appropriate image processing algorithms. The use of COTS and medically compliant ultrasound readers for in-vivo telemetry will obviate the need to design dedicated ultrasound decoders. They would simplify the adoption of technology by practicing clinicians. Examples of such low-data-rate devices where the FEC technique could be applied include health-monitoring sensors for hip or knee-implants [28].

Chapter 3

Energy Harvesting Cardiac Valvular Perturbations

This chapter investigates the feasibility of harvesting energy from cardiac valvular perturbations to self-power a wireless sonomicrometry sensor. Compared to the previous studies involving piezoelectric patches or encasings attached to the cardiac or aortic surface, the proposed study explores the use of piezoelectric sutures implanted in proximity to the valvular regions, where non-linear valvular perturbations could be exploited for self-powering. Using in-vivo studies on ovine animal model, the magnitude of valvular perturbations are first measured using an array of piezoelectric crystals implanted around the tricuspid valve. These measurements were then used to estimate the levels of electrical energy that could be harvested using a simplified piezoelectric suture model. These results were re-validated across seven different animals, before and after valvular regurgitation was induced. In this chapter we show that power harvested from different annular planes of the tricuspid valve (before and after regurgitation) could range from nano-watts to milli-watts, with the maximum power harvested from the leaflet plane. We believe that these results could be useful for determining

optimal surgical placement of wireless and self-powered sonomicrometry sensor, which in turn could be used for investigating the pathophysiology of ischemic regurgitation (IR).

3.1 Introduction

A cardiac (tricuspid or mitral) valve is a complex structure with a dynamic physiology that relies on an intricate inter-play between its individual components, which include the ventricles, papillary muscles, the annulus and the atrium. Failure in any one or all of these components, regardless of cause, can lead to significant mitral regurgitation (MR) and an inability to sustain normal cardiac performance. Specifically, ischemic mitral regurgitation (IMR) presents a vexing clinical problem where even modest geometric perturbations of the valvular and sub-valvular apparatus could result in significant insufficiency [31]. Unfortunately, the pathophysiology of IMR is not well understood, and studies have suggested that the underlying cause lies in the annulus and the sub-valvular apparatus, which need to be precisely tracked. However, tracking these 3D geometric perturbations presents a challenge for existing clinical imaging modalities like echocardiography or magnetic resonance imaging [32], hence requiring sensors (for example, piezoelectric crystals) to be implanted in proximity to the valvular apparatus, as shown in Fig. 3.1 (a). Current state-of-the-art sonomicrometry techniques [33] requires hard-wiring sensors to an external data acquisition and a power source which requires the animal to be intubated under general anesthesia. This prevents monitoring of the precise three-dimensional changes in the mitral valvular complex during the evolution of IMR. For chronic and long-term monitoring, these sensors are desired to be wireless (untethered) and preferably self-powered by the cardiac activity, as shown in Fig. 3.1 (b).

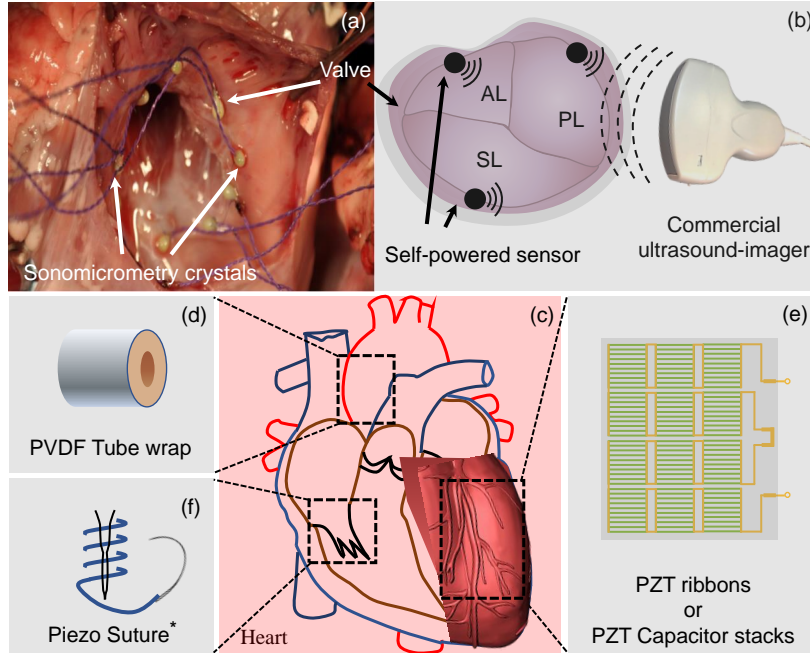


Figure 3.1: Vision of the proposed research for chronic monitoring of valvular dynamics and (a) overcoming the limitations of existing hard-wired sensing technology. (b) An array of wireless millimeter-scale self-powered implants sutured on the valve can be interrogated using a commercial diagnostic ultrasound scanner. (c) Anatomy of Heart and existing techniques for harvesting heart dynamics, (d) PVDF tube wraps for extracting energy from the outer annulus of the aorta, (e) PZT ribbons for harvesting from the surface of the heart which can power pacemakers (f) Proposed harvesting method to extract energy directly on the valve.

Previous approaches of self-powering using cardiac activity have resulted in flexible piezoelectric transducers for harvesting energy from the cardiac surfaces [34–37], two special cases were shown in Fig. 3.1(d)-(e). In particular, [34, 35] proposed a flexible PZT transducer placed on the surface of the swine heart and was shown to harvest enough energy to power implantable devices like pacemakers. In [36], a cylindrical PVDF transducer is placed around the ascending aorta as was demonstrated for biomechanical energy harvesting. Unfortunately, these centimeter-scale surface transducers would require explicit wiring to the sensors implanted in proximity to the cardiac valve, which could lead to surgical complications and mechanically impede the valve’s dynamics. In this chapter, we investigate the feasibility of using piezoelectric sutures, which are used in tethering piezoelectric crystals to the valve’s surface for harvesting energy. The key concept here is to exploit strong valvular perturbations to excite non-linear modes in the piezoelectric suture. These non-linear or broadband modes could then be used to boost a piezoelectric transducer’s energy harvesting capability, as have been previously reported in literature [38–40].

Our main objective is to estimate the amount of electrical power that can be locally harvested (using a model of piezoelectric suture) from non-linear geometric perturbations of different annular regions of a cardiac valve. The study is based on the following three results that have been reported in our previous works: (a) Using implanted piezoelectric crystals (as shown in Fig. 3.1(a)) it is possible to reliably measure subtle geometric perturbations of the mitral-valve in real-time [33, 41]; (b) The implantation of the crystals in the proximity of the valve does not affect the valvular dynamics [42–44]; and (c) An FDA compliant ultrasound scanner can be used to image the ultrasonic pings simultaneously generated by the implanted piezoelectric crystals and electrical power consumed by the crystals is less than a few microwatts [45]. The results of the feasibility study reported in this chapter would therefore facilitate the development, optimization, and surgical placement of an array of

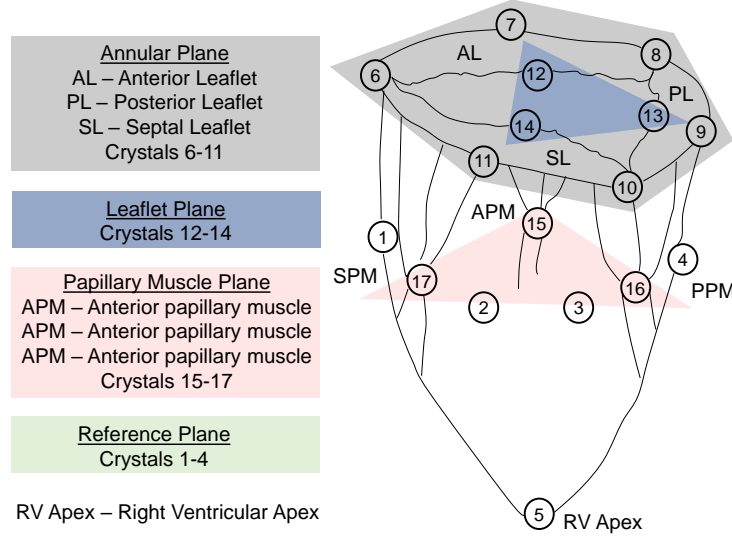


Figure 3.2: Geometric placement of sonomicrometry crystals and anatomy of tricuspid valve where crystals labeled (1-5), (6-11), (12-14), (15-17) were located around the epicardium, tricuspid annulus, tricuspid leaflet edges and papilliary muscle tips of the right ventricle respectively.

self-powered sonomicrometry sensors that can be used for real-time, wireless, and long-term tracking of valvular structures.

3.2 Experimental Methods

Sonomicrometry based measurement involves tracking the distances between the different spatial locations marked using ultrasound crystals, which are millimeter-scale implants and weigh less than 20 milligrams. For instance, Fig. 3.1 (a) shows a typical placement of the crystals around the tricuspid valve region [46]. Each of these crystals sequentially transmits an ultrasonic pulse, which is then received by the other crystals. The time-of-delay between the transmitted and received pulses is then used to estimate the respective distances between the crystals and the perturbation, and the valve dynamics. In this chapter, we have used the

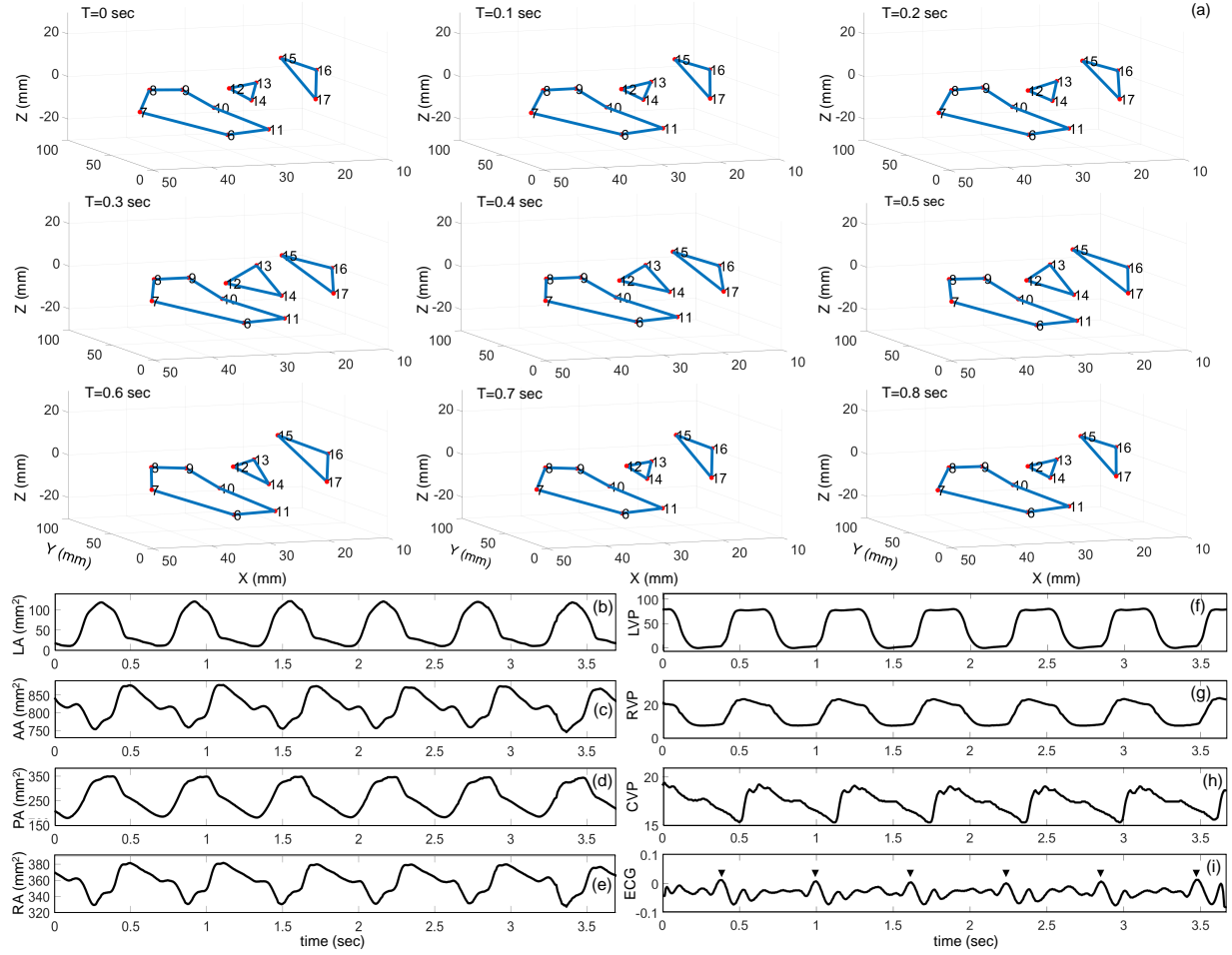


Figure 3.3: (a) 3D reconstruction of the valve using the raw data acquired using the sonomicrometry equipment at different instances showing the crystals' relative movement. (b)- (e) shows the variations of the area enclosed by the polygon formed by the crystals in each plane, respectively. (f) - (h) shows the pressure values LVP RVP and CVP, respectively, and (i) shows the processed ECG data, all collected simultaneously. The peaks are marked manually, indicating the duration of the cardiac cycle.

sonomicrometry preparation in live ovine models to estimate the magnitude of mechanical power that can be harvested using local valvular perturbations.

3.2.1 Ovine model preparation

The annular planes around the tricuspid valve are shown in Fig. 3.3, which also shows the placement of the sonomicrometry crystals (marked 1-17) [46]. The time-of-delay between the transmitted and received sonomicrometry pulses are then used to estimate the respective distances between the crystals and the relative mechanical strain at the marked locations. In-vivo experiments were performed on seven adult male sheep in a fully equipped and accredited animal facility at West Michigan Regional Laboratory, a part of the Spectrum Health Delivery System. The clinically pertinent surgical procedures followed the protocols described in the published literature supports the ovine model as the preferred animal model of human mitral valve pathophysiology.

Once the animals were sedated, intubated, and under general anesthesia, a left thoracotomy was carried out in a sterile fashion to expose the heart. After full heparinization, cardiopulmonary bypass was established, and the heart was subsequently arrested with standard crystalloid cardioplegic solution. Under cardiac standstill, the tricuspid valve was exposed through the right atrial appendage. Two sonomicrometry crystals were placed on the more dynamic posterior mitral annulus approximately 2 cm apart. Wire connections of the sonomicrometry crystals are connected to an outside data acquisition source (from SonoMetrics) through the open thoracotomy. The animals are subsequently weaned from cardiopulmonary bypass and stable hemodynamics achieved. Various physiologic conditions are introduced: 1) increased heart rate (30% above baseline) and contractility with epinephrine infusion 2)

blood pressure increase (50% above baseline) with norepinephrine infusion 3) bradycardia (heart rate below 60) with esmolol infusion. Simultaneous data acquisition from crystals was performed before and during each intervention with at least a 5 minute stabilization period between interventions.

3.2.2 Experimental Setup

3.2.3 Data Analysis

The sutured crystals on the tricuspid valve were clustered into four groups based on their location. As shown in Fig. 3.3, the crystals 6-11 were placed on the tricuspid annulus, 12-14 were placed on the edges of the leaflets, 15-17 were placed on the tips of the papillary muscles, while crystals 1-5 were sutured on the epicardium of the right ventricle. The raw data from the SonoMetrics equipment gave us the recorded traces for every single crystal working both as a receiver and a transmitter. The data was recorded using 17 crystals, which corresponds to 289 raw traces for every run (around 130 Hz). The data were initially processed using the software Sonosoft, provided by the manufacturer. The 3D coordinates of the crystals at each time instant were computed, assuming the location of crystal 5 as the origin. Post simulations were carried in MATLAB using a custom data analysis software.

Fig. 3.4(a) shows an experimentally determined three-dimensional map of the annular regions of an ovine tricuspid valve. X, Y, and Z refer to the three coordinates of the crystals measured in millimeters (mm). Each of the crystals labeled 12-14 in Fig.3.4(a) track the relative size of the leaflet plane during each opening and the closing of the valve. Other crystals in Fig. 3.4(a) are used for tracking auxiliary regions (annular edges and papillary muscle

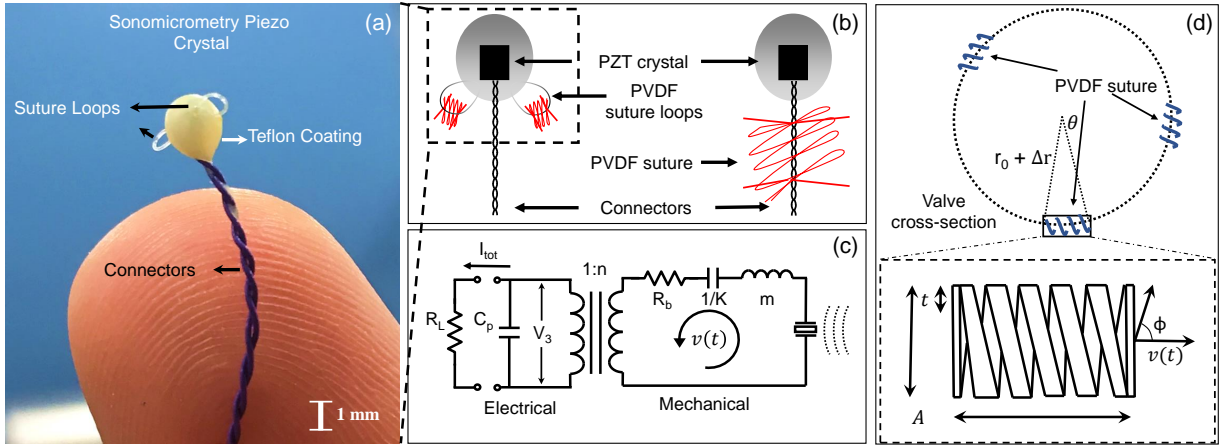


Figure 3.4: (a) Sonomicrometry crystal and (b) mechanism for harvesting energy either by replacing the suture loops or by using a piezoelectric suture to attach the crystal to the valve. (c) Suture model and parameters used in the analysis. (d) Cross-section of a valve assuming circular contour and sutured crystals tied to the boundary. At the bottom shows the model a multi-loop piezoelectric suture which reduces the effective local strain level $d\delta$ by a loop factor N .

tips) in the proximity of the valve. In our previous studies [46] we have shown that the sonomicrometry data could also be used for estimating changes in clinically relevant valvular parameters, for example, the changes in subvalvular distances and the annular area, which could be useful for clinical diagnostic purposes. To validate the data obtained using our experimental setup, we first compute a simple geometric area to verify the data with the well-accepted ECG and pressure recordings, which were also collected simultaneously. Fig. 3.4 (b)-(e) show the estimated change in the planar area corresponding to different tricuspid valvular regions based on the raw data collected from an ovine model (LA, AA, and PA refers to the area computed in leaflet plane, annular plane and papillary muscle plane respectively). Fig. 3.4 (f)-(h) show the plots for left-ventricular pressure (LVP), right-atrial pressure (RVP) and central venous pressure (CVP) for the same duration. Also Fig. 3.4 (i) shows the filtered ECG data. The raw data of ECG collected using an ADC is processed by a Savitzky-Golay least-square polynomial filter [47] to extract the epochs which indicate the cardiac cycle. The

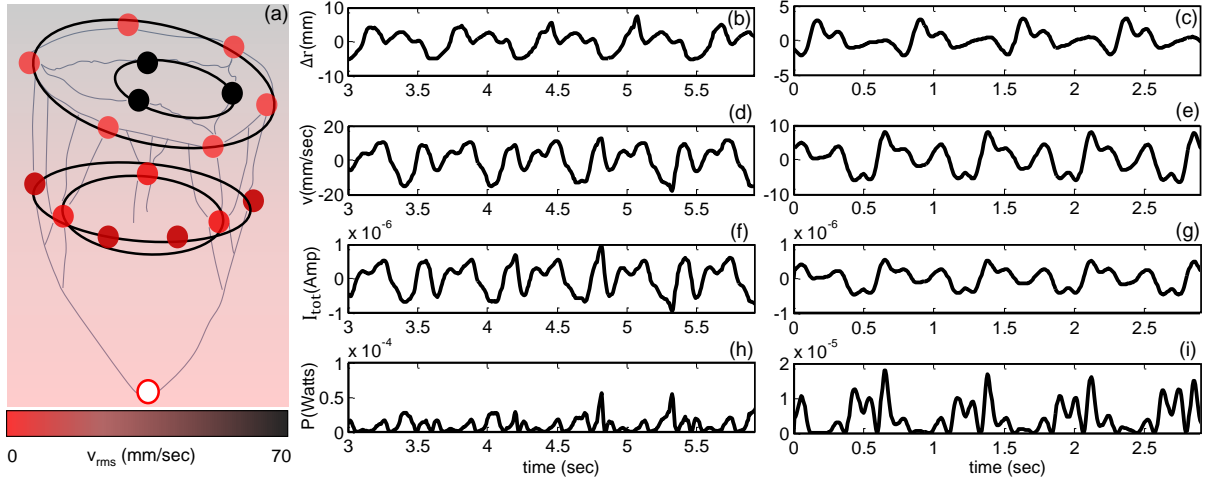


Figure 3.5: (a) Average velocity profile at each cross section which is obtained by analyzing the data recordings from seven ovine models (black indicating the maximum and red corresponding to zero velocity). (b)-(i) Estimated change in radius, velocity, current and power on the leaflet edges based on the data collected before and after inducing tricuspid-regurgitation (TR).

results validate the accuracy and the potential of SM measurements in studying the valve dynamics.

The measured geometric data was consistent with published reports from other groups, [48, 49] solidifying the reliability and validity of wired sonomicrometry technology. Another observation that can be inferred from the wired sonomicrometry experiments is that the rate of change in mechanical strain (change in dimension normalized by the original dimension) due to valvular dynamics is in the order of $0.5 \text{ } \epsilon/\text{s}$. This is also consistent with strain and strain-rate measurements obtained using cardiac ultrasound [50]. This magnitude of strain-variations could potentially be exploited to harvest microwatts of energy using a millimeter-scale piezoelectric transducer.

3.2.4 Energy Harvesting Model

Our modeling study is based on two techniques for integrating piezoelectric transducers into the sonomicrometry crystal, as shown in Fig. 3.5(a). Either the crystals could be tethered directly to the valve annulus through a piezoelectric suture, or the crystal could be first integrated by a piezoelectric suture loop, which could then be tethered to the valve using a standard surgical suture, as shown in Fig. 3.5 (b). Connecting piezoelectric loops to the crystal could be the easiest way for designing an integrated implant, but it might be less efficient in energy harvesting because of its low mechanical coupling (contact) to the tissue. Whereas using a piezoelectric suture could provide good mechanical coupling with the tissue, however, fabricating a flexible suture might present a challenge. In our estimation study, we abstract these two possible configurations while noting that future research would be needed to choose between the two options.

For our energy estimation model, we approximated the shape of the valve to be circular, with each crystal located along the perimeter of the circle, as illustrated in Fig. 3.5(d). Ideally, suture can be assumed as a helical loop with a limited number of turns N . However, in our analysis, we approximated the shape to a rectangular strip with a thickness t and cross-section area A . Note that the use of a helical loop with N turns (as shown in Fig. 3.5(d), effectively reduces the local strain level by N and ensures that the piezoelectric suture can operate within the material fracture compliance limits. We model the radius of the circular contour as a function of time and thus, it can be considered $r = r_0 + \Delta r(t)$ where r_0 is the mean radius during a cardiac cycle. First, a normal vector to the plane passing through the clustered set is estimated based on the minimum mean squared error (MMSE). These coordinates were then rotated and translated so that the crystals were located on the XY plane with the center at the origin. The radius r of the circle passing through the points is then estimated based

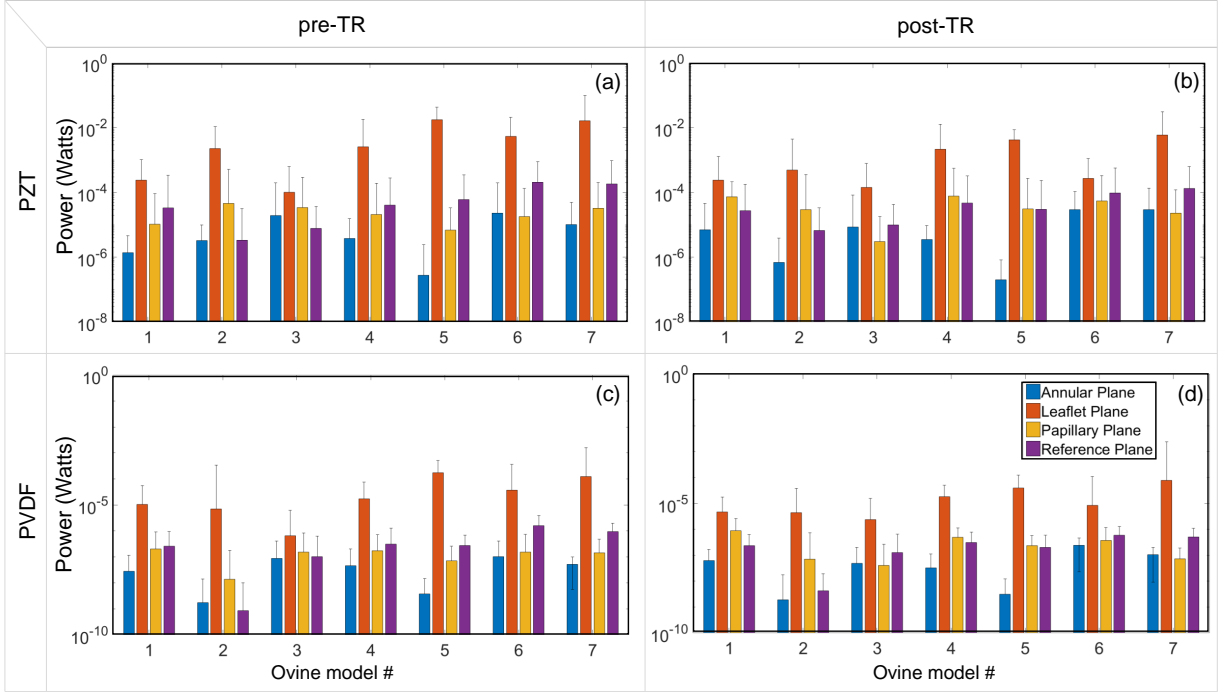


Figure 3.6: (a)-(b) shows the variations in power values estimated on each contour across the seven datasets (ovine sheep models) before and after inducing TR respectively (assuming PZT as the material of suture). Similarly (c)-(d) shows the variations for the case of PVDF suture.

on the MMSE. The rate of change in radius $v(t)$ at time instant t at each cross-sectional plane is estimated using a first order approximation as

$$\begin{aligned} v(t) &= \frac{d}{dt}(r(t)) \\ v(n) &= \frac{r(n) - r(n-1)}{\Delta t} \end{aligned} \quad (3.1)$$

where the radius $r(n)$ is estimated for every cycle and the sampling time-interval Δt is chosen to be around 75 ms. The velocity profile for each cross-sectional plane is shown in Fig. 3.6 (a), which is the average value across the data recorded from seven ovine models. Although the direction of the strain in the suture would be along ϕ , as shown in Fig. 3.5 (d), in our current analysis, we consider $v(t)$ to be the estimate of the strain-rate of the suture since our objective is to estimate the maximum power levels.

Assuming the two electrodes of the piezo are electrically neutral, the total charge (Q_{tot}) generated on each side of the electrode due to deformation is given by,

$$Q_{tot} = \int D_3 dA \quad (3.2)$$

where, D_3 is the electrical displacement along the polarization direction.

D_3 is determined by the amount of stress (T_1) and the electric field generated across the electrodes and is given by,

$$\begin{aligned} D_3 &= -d_{31}T_1 + \epsilon_{33}E_3 \\ &= -d_{31}Y_{11}\eta_1 + \epsilon_{33}\frac{V_3}{t_3} \end{aligned} \quad (3.3)$$

Table 3.1: Piezoelectric properties and parameters used in the suture model.

Parameter	Symbol	Value (PVDF)	Value (PZT)
Strain coefficient	d_{31} (m/V)	23×10^{-12}	110×10^{-12}
Dielectric constant	ϵ_{33} (F/m)	11×10^{-11}	198×10^{-11}
Young's modulus	Y_{11} (N/m ²)	3×10^9	6×10^{10}
Transducer thickness	t_3	$10 \mu m$	$10 \mu m$
Electrodes area	A	$10 mm^2$	$10 mm^2$
Load resistance	R_L	$60 M\Omega$	$60 M\Omega$

Equation. 3.3 is the general constitutive equation for the piezoelectric materials, where the parameters of the material are summarized in Table 3.1.

Defining the strain to be the ratio between relative change in radius ($\Delta r = r - r_0$) and initial radius (r_0), the rate of change in charge is given by,

$$\begin{aligned}
 Q_{tot} &= -\frac{d_{31}Y_{11}A}{r}\Delta r + \epsilon_{33}\frac{A}{t_3}V_3 \\
 \frac{dQ_{tot}}{dt} &= -\frac{d_{31}Y_{11}A}{r}\frac{dr}{dt} + \epsilon_{33}\frac{A}{t_3}\frac{dV_3}{dt} = I_{tot}.
 \end{aligned} \tag{3.4}$$

and A is the area of suture strip. Based on the equivalent circuit model of the piezoelectric transducer as shown in Fig. 3.4 (c) the voltage (V_3) and current I_{tot} flowing through the load resistor is given by,

$$\begin{aligned}
 \frac{dV_3}{dt} + \frac{V_3}{RC_p} - \frac{d_{31}Y_{11}A}{C_p r} \frac{dr}{dt} &= 0 \\
 \frac{dV_3(t)}{dt} + \frac{V_3(t)}{RC_p} - \frac{d_{31}Y_{11}A}{C_p} \frac{v(t)}{r(t)} &= 0
 \end{aligned} \tag{3.5}$$

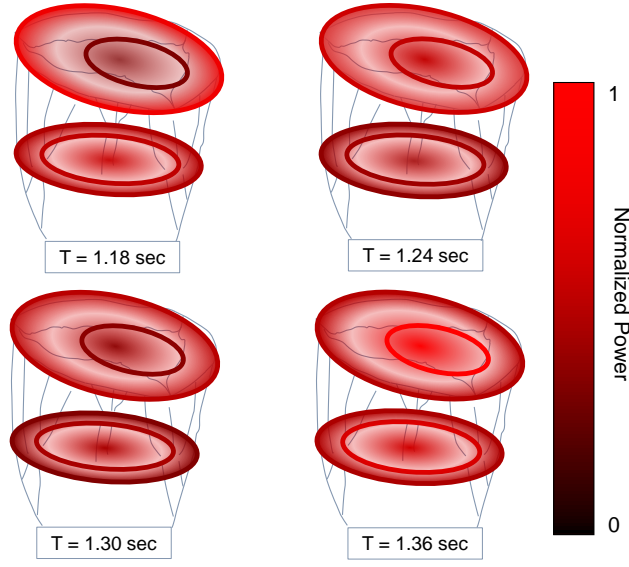


Figure 3.7: Power profile across the tricuspid valve showing the variations, in the normalized power, with respect to time. The power levels change rapidly with crystals located at different locations harvesting maximum power at different time-instants.

where $C_p = \frac{e_{33}A}{t_3}$ is the intrinsic capacitance as shown in Fig. 3.4 (c). Note that this equation is consistent with the earlier reported works [34]. The differential equation can be discretized for simulation as

$$V_3(n+1) = V_3(n) - \Delta t \times \left(\frac{V_3(n)}{RC_p} - \frac{d_{31}Y_{11}A}{C_p} \frac{v(n)}{r(n)} \right) \quad (3.6)$$

and the instantaneous power (P) across a resistor load of R can be estimated as

$$P(n) = \frac{V_3(n)^2}{R} \quad (3.7)$$

It can be seen that the voltage generated across the transducer is a function of the history of the rate of change in strain, as shown in equation. 3.6, which is directly proportional to instantaneous rate ($v(t)$) and inversely proportional to radius ($r(t)$). Table. 3.1 shows

Table 3.2: Maximum and average estimated power that can be harvested at different annular planes, under different conditions using PZT

Condition; piezo material	pre-TR; PZT		post-TR; PZT	
	Max. Power	Avg. Power	Max. Power	Avg. Power
Annular plane (6-11)	$46 \mu W$	$6.5 \mu W$	$30.3 \mu W$	$3.8 \mu W$
Leaflet plane (12-14)	21 mW	2 mW	5 mW	0.6 mW
Papillary Muscle plane (15-17)	0.14 mW	$22.1 \mu W$	0.1 mW	$15.4 \mu W$
Reference plane (1-4)	0.23 mW	$27.8 \mu W$	0.1 mW	$17.2 \mu W$

typical values of a piezo material which were reported in literature [51] and used here in our simulations and analysis.

3.3 Results

Based on the radius estimation procedure, different approximations of the cross-sectional area were made, and the rate of change in the radius was estimated using the equation 3.1. Fig. 3.6 (b),(c) shows the variations in the change in radius at the leaflet plane with respect to time for a particular experiment case before and after inducing tricuspid-regurgitation (TR), respectively. Fig. 3.6 (d),(e) shows the instantaneous velocity values for either cases based on the method mentioned in section 3.2.4. The power that can be harvested from the suture is

Table 3.3: Maximum and average estimated power that can be harvested at different annular planes, under different conditions using PVDF

Condition; piezo material	pre-TR; PVDF		post-TR; PVDF	
	Max. Power	Avg. Power	Max. Power	Avg. Power
Annular plane (6-11)	0.21 μ W	39.3 nW	0.1 μ W	17.8 nW
Leaflet plane (12-14)	0.24 mW	11 μW	0.19 mW	8.9 μW
Papillary Muscle plane (15-17)	0.84 μ W	0.17 μ W	0.6 μ W	0.1 μ W
Reference plane (1-4)	0.78 μ W	0.13 μ W	0.38 μ W	61.5 nW

estimated using the equation 3.7, for two specific cases: (a) before TR is induced (labeled as pre-TR), and (b) after TR is induced (labeled as post-TR). The results for both these cases are shown in Fig. 3.6(f)-(g). The results show that even though the radii change is periodic; there is a massive difference in power estimated at each cycle, as shown in Fig. 3.6(f). This can be attributed to the natural deviations in the ovine cardiac function and intrinsic non-linear dynamics of valvular perturbations. These non-linear effects result in energy bursts that can be readily harvested for self-powering. Note that for surface piezoelectric transducers, like the ones reported in [34], the non-linear dynamics (like buckling) gets filtered out, resulting in smooth and periodic strain-variations. Therefore, transducers with a large surface area have to be used to harvest sufficient energy.

Fig. 3.7 shows the bar plots corresponding to the estimated power that can be harvested from each annular plane for different animals and for pre and post TR conditions. We estimated the power levels assuming two types of suture models incorporating two different piezoelectric materials. The material properties and parameters used in our simulations were summarized in Table. 3.1. Note that while PZT sutures could provide more power, they need to be adequately encapsulated to ensure biocompatibility. Fig. 3.7 shows that the estimated power values are consistent across different animals showing the scalability of the proposed approach. The instantaneous voltage and current values range between 0-20 V and 0-1 μA respectively. In all cases, the maximum amount of power can be harvested from the leaflet plane. Although there is a slight decrease in power for the case of pre-TR and post-TR, as shown in Fig. 3.7(a)-(d), it can be seen that the power levels across different cross-sections in all the cases are almost similar which implies that self-powering is still feasible even after TR is induced. Fig. 3.8 shows the power profile for a particular case of an ovine model (pre-TR, using PVDF suture model) where the variations of the normalized estimated power at different instances in time. It can be seen that variations of power level are rapid (the time-scale of the change is in order of 60 msec) compared to that of the change in radius or velocity. Also, the distribution of power level shows bursts where different sections of the valvular planes deliver maximum power at different time instances. Thus, placement of the sutures and the sonomicrometry sensors is essential to ensure efficient and consistent harvested power levels.

Although the analysis presented in this chapter are based on the simulations of the suture models, earlier studies have shown a good match between the simulation studies and experimental results [34]. Thus, the average power that can be harvested, as summarized in Table. 3.2-3.3 should scale. Also, note that the model assumed the piezoelectric suture to be operating in the transverse mode; however, we need to consider the longitudinal and shear

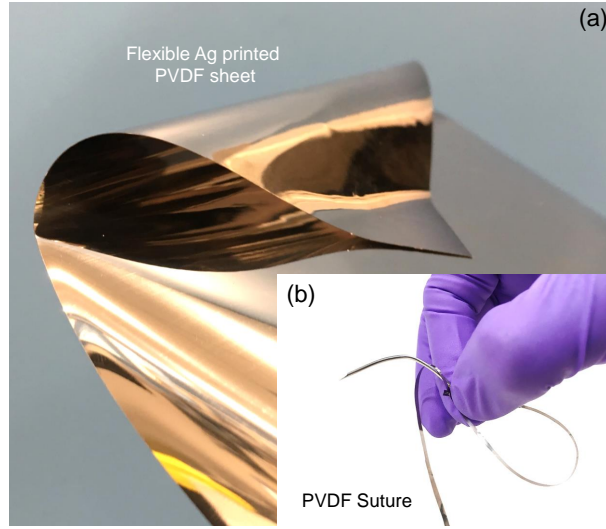


Figure 3.8: Flexible silver-coated PVDF sheet as a potential candidate for constructing piezoelectric sutures.

effects in practical implementation. Therefore, the numbers summarized in Table. 3.2-3.3 represent the upper limit and needs to be moderated based on practical suturing conditions. Also the power density is around $10mW/cm^2$ in the case of PZT and $100\mu W/cm^2$ in the case of PVDF for a piezoelectric suture.

3.4 Discussion

The feasibility analysis presented in this chapter is based on ideal assumptions on the suture orientation and its material properties, and therefore should be considered the upper limit. While the results presented in this chapter have been estimated using suture parameters summarized in Table 3.1, the results should scale with any variations in these parameters. It can be seen from equation. 3.6 that the voltage scale linearly with the change in the area where the power levels vary quadratically; however, corner effects need to be considered when

translating these results. Also, a suture with dimensions 0.5 mm x 2 cm might be reasonable for simulations, but such a configuration's practical feasibility needs to be further explored.

In practice, however, the results may differ, and the non-linear valvular dynamics might boost or damp the level of harvested energy. In particular, mechanical properties like buckling and torsional strain in the case of helical suture, which is not captured by the linear model given in equation. 3.5, could enhance the results. In contrast, the properties like damping and mechanical coupling can deteriorate the transducer's performance needs to be validated with experimental results. Future work will also include verifying an integrated sonomicrometry suture in-vivo. Fig. 3.8 shows one possible configuration to construct the suture cut out of a PVDF sheet. The mechanical stability, bio-compatibility, and packaging of the suture is a topic of future research. Also, future work will involve integrating piezoelectric energy harvesting circuits [4] and sonomicrometry telemetry circuits [18] with the piezoelectric suture.

3.5 Summary

This chapter summarizes the estimated power levels that can be harvested from non-linear mechanical perturbations of a cardiac valvular apparatus. Our analysis demonstrates the feasibility of harvesting $0.1-10mW/cm^2$, which is orders of magnitude higher than the previous configurations that harvested energy from the surface of the heart or the aorta. For instance, the time-average power density was reported to be $1.2\mu W/cm^2$ when harvesting energy from the surface of the heart [34]. In contrast, the power density was $170nW/cm^3$ when the energy was harvested from the aorta [36]. Experimental verification of this improvement would be the subject of future work. However, higher harvested power levels open the possibility of

designing self-powered sonomicrometry based sensors that can be used for chronic monitoring of mitral-valve dynamics and post-surgical IMR.

Chapter 4

B-scan Imaging based Telemetry

In chapter 2 we demonstrated that a commercial-of-the-shelf (COTS) M-scan ultrasound imaging system could be used for designing multi-access in-vivo ultrasound communications links. We demonstrated the feasibility of data rates up to 800 Kbps for implantation depths greater than 12 cm while dissipating only microwatts during transmission. However, if the transmission energy-budget could be reduced down to nano-watts, not only the battery form factor at the implant could be reduced but the telemetry could be potentially be self-powered using energy harvested in-vivo [52]. Reducing the transmission power will also reduce imaging artifacts when the ultrasound system is used simultaneously for imaging other physiological processes like blood flow or tissue palpitations [53]. In this chapter, we investigate if the transmission energy requirements can be reduced by exploiting the beam-forming feature available on most commercial ultrasound imaging systems.

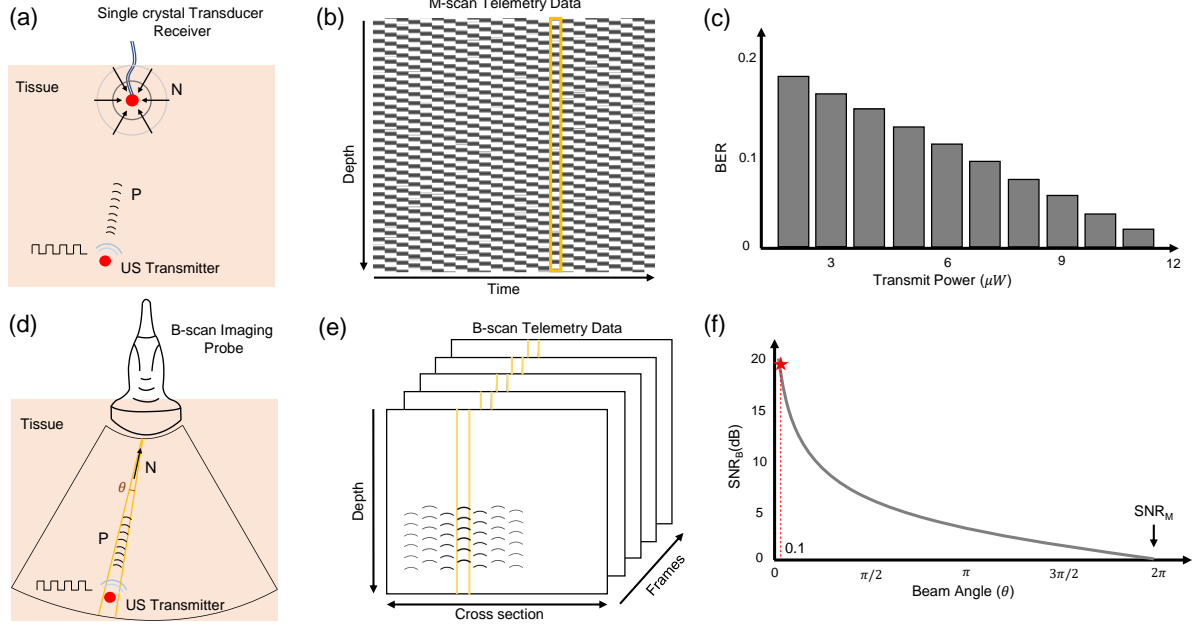


Figure 4.1: (a) Principle of M-scan telemetry as reported in 2; (b) Illustration of a typical M-scan image when the data is being transmitted using ON-OFF signaling. (c) BER corresponding to the M-scan telemetry link as reported in 2 when the transmit power is varied from $1\mu W$ to $12\mu W$. (d) Principle of the proposed B-scan telemetry. (e) Illustration of a typical B-scan image showing the presence of transmitted data in a 2D cross-section as well as across several B-scan frames. (f) Anticipated improvement in SNR (highlighted by star) for B-scan telemetry compared to M-scan telemetry scheme when operated around beam-angle of 0.1 radians ($\approx 5^\circ$).

4.1 Operation Principle

Fig. 4.1 shows the principle underlying the proposed approach and compares it against our previously reported M-scan based ultrasound telemetry. In M-scan telemetry shown in Fig. 4.1(a), a communication link is established between two single-element ultrasound crystals. One of the elements acts as a transmitter and is implanted inside the tissue. The other element, acting as an interrogator is located on the surface of the skin and is driven by an M-scan ultrasound imaging system, as shown in Fig.4.1(a). Fig.4.1(b) shows a sample

M-scan image data when the transmitter crystal is driven by a periodic ON-OFF signal. The transmitted pulses create an imprint on the M-scan image, which upon further processing reveals the transmitted data. In [45], we have characterized the M-scan telemetry link in terms of its BER and the transmission power. Fig. 4.1(c) shows a sample result which shows that only microwatts of transmission power are required to achieve reasonable BER. However due to lack of directionality, the received noise power (N) is isotropic as shown in Fig. 4.1(a). In practice, the information about the location of the implant is known apriori and hence, could be leveraged to boost the received signal to noise power ratio (SNR) using beam-forming. In the proposed B-scan telemetry, a linear array imaging probe (interrogator) is used for beam-forming and for capturing the transmitted data from the directions of interest and a specific depth, as shown in Fig.4.1(d). Sample B-scan data is shown in Fig. 4.1(e) where the effective SNR (SNR_B) is determined by the ratio of received signal power and the noise incident from a specific beam-angle (θ). Similar to SNR calculations used in radio-frequency MIMO systems [54], it is anticipated that the effective SNR (SNR_B) for B-scan telemetry should be inversely proportional to the interrogation beam angle. Thus, the B-scan based telemetry should provide higher SNR compared to the M-scan telemetry.

4.2 Experimental Setup

Fig. 4.2 shows the experimental setup that has been designed to verify and characterize the proposed B-scan telemetry. An ultrasound transmitter was prototyped using a Texas Instruments microcontroller board (TI CC1310) and the system was packaged in a water-proof container and then suspended in a water bath as shown in Fig. 4.2(a). A millimeter-sized piezoelectric crystal was used as an ultrasound transducer(Sonometrics Corp.) and was

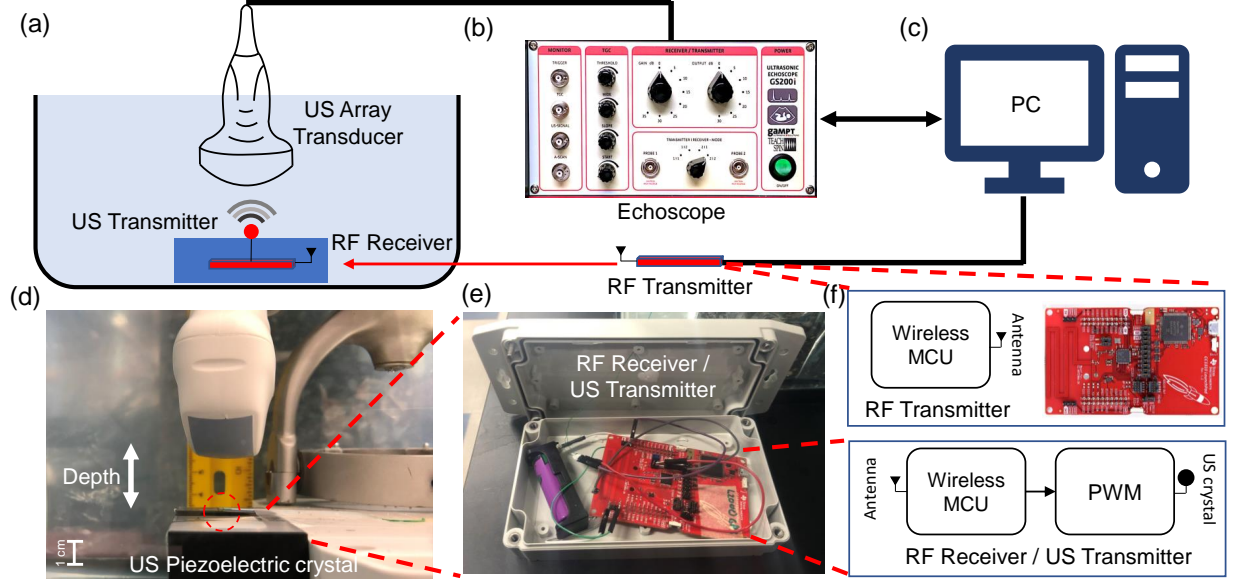


Figure 4.2: (a) Illustration of the experimental setup used to verify and quantify the performance of B-scan telemetry in a water transmission medium. A linear transducer array is driven by (b) an echoscope which is used to acquire B-scan images which are then post-processed on a (c) computer; (d) Picture of the water-bath highlighting the interrogation depth and the relative orientation of the imager and the implant; (e) The prototype of the ultrasound transmitter implemented using a TI CC1310 board and enclosed in a sealed waterproof container. (f) RF module is used for remote programming of the submerged ultrasound.

fixated outside the container such that it was aligned with the ultrasound imaging probe, as shown in Fig. 4.2(a). The B-scan data acquired by a commercial echoscope was stored on a computer (Fig. 4.2(c)) and the data is post-processed using methods described in section 4.2.5. An external RF micro-controller platform (TI CC1310) was used to wirelessly control the power and transmission rate of the ultrasound transmitter submerged in the water-bath, as shown in Fig. 4.2(f). Note that the RF link was only turned on for reprogramming the ultrasound transmitter to transmit at different power levels or for adjusting the transmission rate. At all other times, the RF link was disabled to minimize electromagnetic coupling.

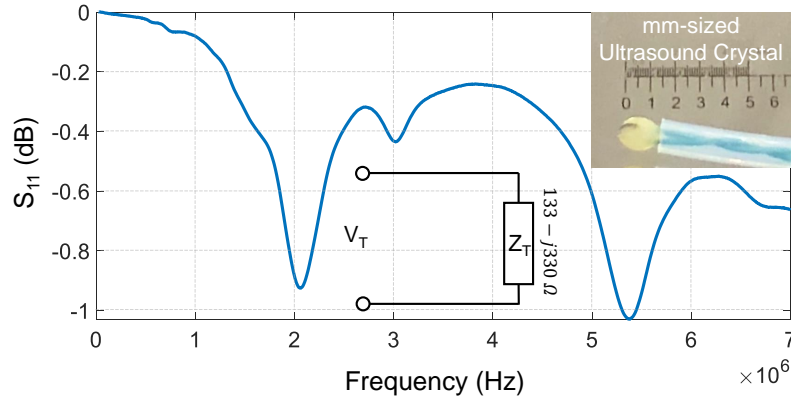


Figure 4.3: Measured S_{11} characteristics of the ultrasound transmitter crystal shown in the inset.

4.2.1 Characterization of the Ultrasound Transmitter Crystal

Fig. 4.3 shows the measured S_{11} characteristic of the piezoelectric crystal used as an ultrasound transmitter. The result shows that the crystal can be driven at different resonances but at the operating frequency of 2MHz, the crystal impedance was measured to be $133 - j330 \Omega$. The estimated impedance has been used in the later sections to calculate the transmitted power using an approach similar to the method described in [45]. The crystal is driven by an oscillator module integrated on the microcontroller board and the amplitude of the driving signal can be adjusted from $V_T = 0 - 5 V$, in steps of $1.2 mV$. The voltage sweep translates to sweeping the transmit power from $0 - 0.7 \mu W$ at sub- nW resolution. Note that the attenuation coefficient of ultrasound in water is given by 0.0022 dB/MHz/cm which leads to a $90 - 97\%$ efficiency in receiving the signal-power at the imager/receiver when the distance to the transmitter is varied from 10 cm to 2 cm .

4.2.2 Echoscope and Linear Transducer Array

The B-scan ultrasound imaging system was implemented by interfacing a convex array ultrasound probe (C5-2R60S-3) to a commercial echoscope (gaMPT GS200i with an integrated Telemed MicrUs ultrasound system). The 256-element ultrasound probe used in our experiments has a field view of 60 degrees with a 65 mm radius of curvature and its operating frequency can be adjusted from 2 MHz to 5 MHz. This focus of the system is customizable with a variable frame-rate of 13-24 fps while being able to image at depths of 90-230 mm respectively. Data from the echoscope was acquired via a USB 2.0 interface and the post-processing of the data was performed in *MATLAB*®. For the experiments, the echoscope was set to a low-transmit power setting and high-receive gain setting to reduce diagnostic imaging artifacts.

4.2.3 RF triggering, Control and Programming

The submerged ultrasound transmitter uses an integrated 915 MHz RF module to communicate with another RF transmitter located outside the water-bath. The RF link was used to wirelessly adjust different transmit parameters (transmission rate and transmission power) without physically disturbing the submerged transmitter. To overcome RF attenuation losses in the water-medium, we set the RF to transmit power to the maximum allowed level while operating within the 915 MHz ISM frequency band. Both the RF transmitter and the submerged RF receiver were designed using the TI CC1310 wireless microcontroller platform. In addition to the TI radio-module, the submerged RF receiver also had a pulse width modulator (PWM) that was used for driving the ultrasound transmitter crystal. The RF transmitter located outside the water-bath was controlled using a serial link to a computer

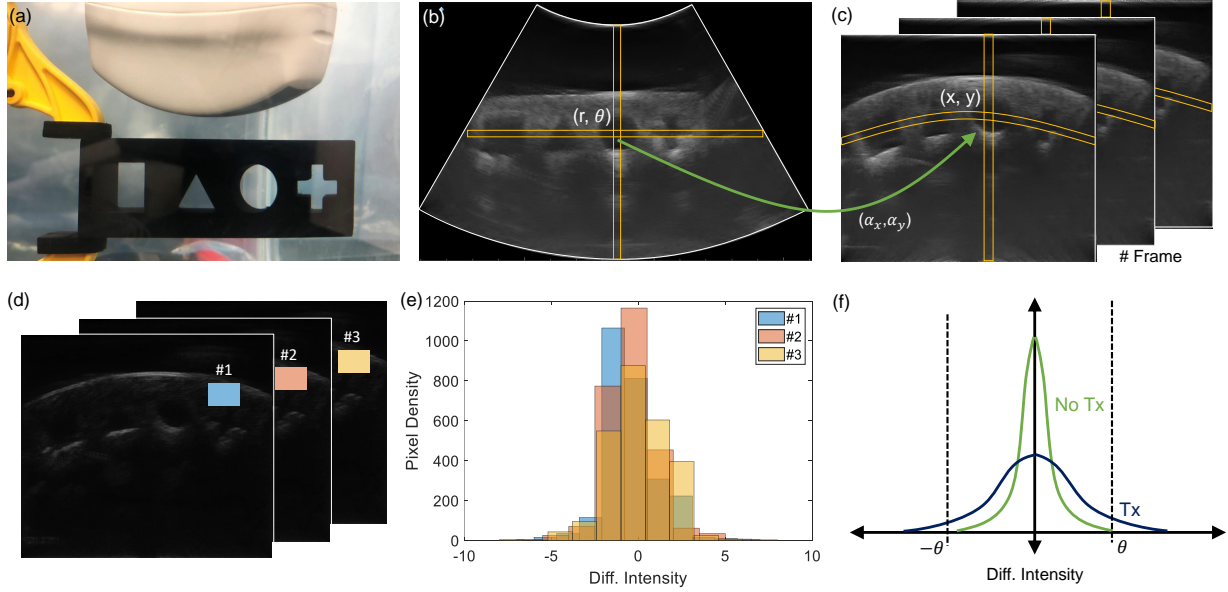


Figure 4.4: Illustration of the B-scan image transformation steps using a (a) template imaging stub where the original B-scan image (b) is transformed pixel-wise into Cartesian coordinates (c); (d) Difference image recovered by high-pass filtering the B-scan image frames; (e) Pixel intensity distributions estimated for a given frame at different instances of time. (f) Anticipated change in pixel intensity distributions in the presence and absence of transmission signal.

which was also used to send information about the pulse width, pulse rate, and transmit power. A transmitter was packaged inside a sealed container which was also used to stabilize the piezoelectric crystal at the bottom of the water tank, as shown in Fig. 4.2(d).

4.2.4 Data Collection and Processing

In this sub-section, we illustrate the data collection and processing steps using B-scan images of a stub comprising of engravings of different geometric shapes, as shown in Fig. 4.4(a). As shown in Fig. 4.4(b), the axial direction to the ultrasound imager provides information about the variations in acoustic impedance along with the depth and the lateral direction shows

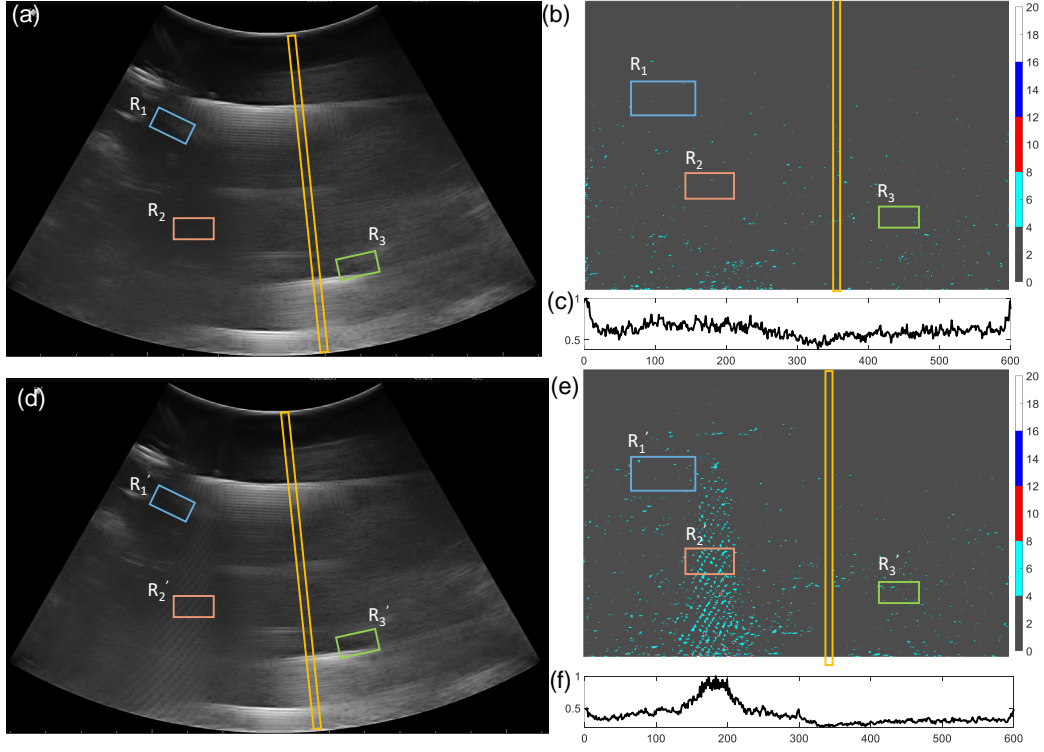


Figure 4.5: (a) Sample B-scan image frame when the transmitter is OFF and the corresponding transformed image (b) after filtering and the (c) column-wise mean intensity vector \bar{I} ; (d) Sample B-scan image frame when the transmitter is ON and the corresponding transformed image (e) after filtering and the (f) column-wise mean intensity vector \bar{I} .

the variations in the acoustic impedance of the medium parallel to the imaging plane. Every frame consists of multiple vertical lines which correspond to a pulse-echo interrogation cycle acquired by the linear array transducer. Echowave II software and user interface provided with the echoscope were used to adjust the transmit and the receive gain of the echoscope and the acquired B-scan images were saved in a PNG format. Note that the acquired images are represented in polar coordinates and the area under interrogation is highlighted using white borders in Fig. 4.4(b). To translate the image pixels into a Cartesian coordinate system, each PNG image was converted to grayscale after which a linear mapping is applied, as illustrated in Fig. 4.4(b)-(c). If a pixel location in the polar coordinates is represented by (r, θ) , then its

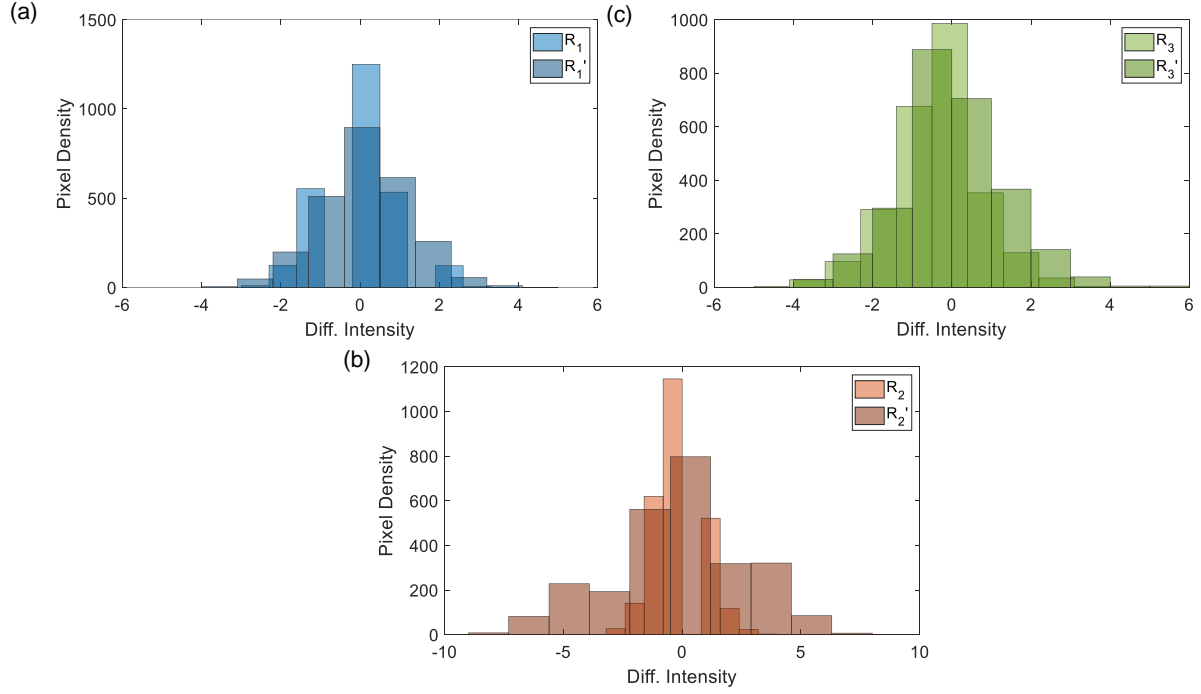


Figure 4.6: (a)-(c) Pixel intensity distributions corresponding to different image patches (R_1 , R_2 , R_3) when the transmitter is OFF and (R_1' , R_2' , R_3') when the transmitter is ON.

corresponding location in the Cartesian coordinate is given by the mapping

$$x = \lfloor r \sin \theta + \alpha_x \rfloor \quad (4.1)$$

$$y = \lfloor r \cos \theta + \alpha_y \rfloor. \quad (4.2)$$

Note that $\lfloor \cdot \rfloor$ are floor operators, and (α_x, α_y) is an offset as shown in Fig. 4.4 (b). This transformation also reduces the image size to $(x_{max}, y_{max}) = 530 \times 600$ pixels as shown in Fig. 4.4(c). In the transformed image, if $U_{(x,y)}^i$ denotes the pixel intensity at location x, y on the i^{th} frame, a difference operation is applied according to

$$W_{(x,y)}^i = U_{(x,y)}^i - U_{(x,y)}^{i-1}. \quad (4.3)$$

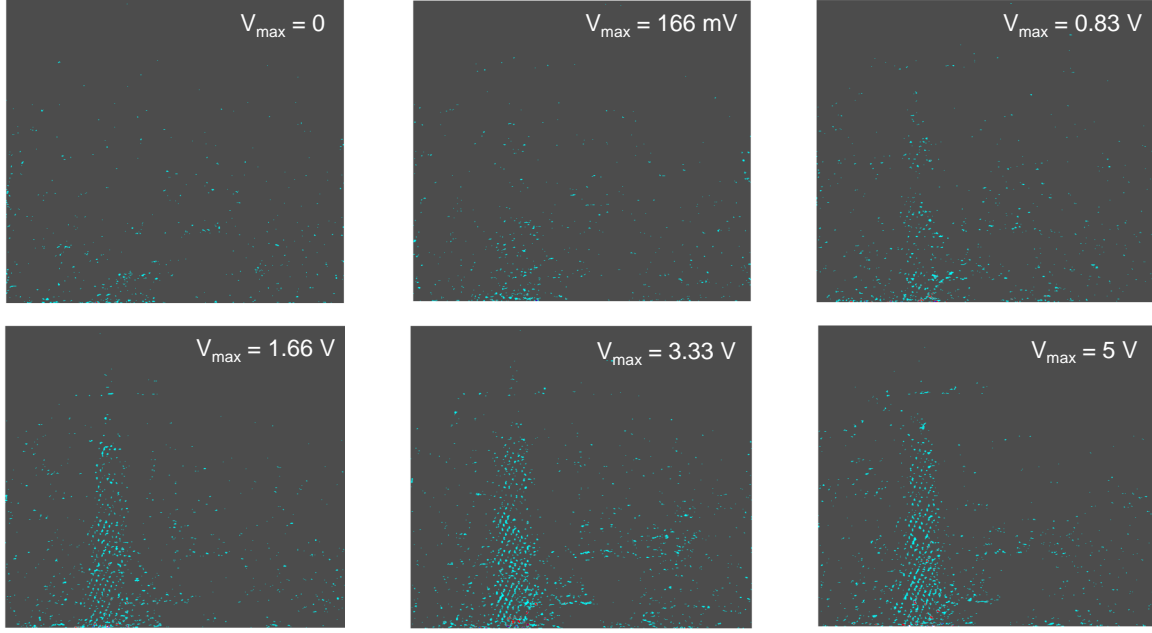


Figure 4.7: High-pass filtered B-scan image frames measured at different magnitudes of transmitted power.

This operation eliminates the static background and retains only information that fluctuates at frequencies greater the frame-rate. Fig. 4.4(d) shows the filtered data W which has been appropriately scaled to improve visualization. Distribution of pixel intensities within an image patch is then estimated across different frames, as shown in Fig. 4.4(e). The result for each frame follows an approximate bell-shaped curve, as shown in Fig. 4.4(f), indicating the distribution can be assumed to be quasi-stationary to the image frames. When the transmitter is ON, we expect the distribution of W to change such that the statistical variance of W should increase, as shown in Fig. 4.4(f). The challenge in this case would be to design a simple and yet robust decoding algorithm that can detect this change or increase in variance.

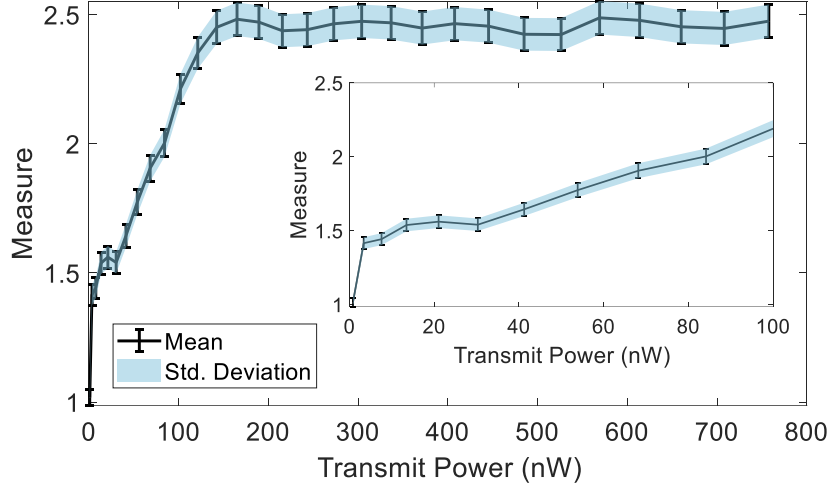


Figure 4.8: Estimated mean and std. deviation for an image patch for different levels of transmitted power.

4.2.5 Telemetry Decoding Algorithm

When the ultrasound transmitter is ON, the imager captures the changes in the received signal power as changes in the pixel intensities on the B-scan images. This is illustrated for high transmit power levels by measuring the column-wise pixel intensities according to

$$I_y^i = \frac{1}{x_{max}} \sum_x |W_{(x,y)}^i| \quad (4.4)$$

where \vec{I} is a vector containing the mean intensity value estimated along the column in the i^{th} frame.

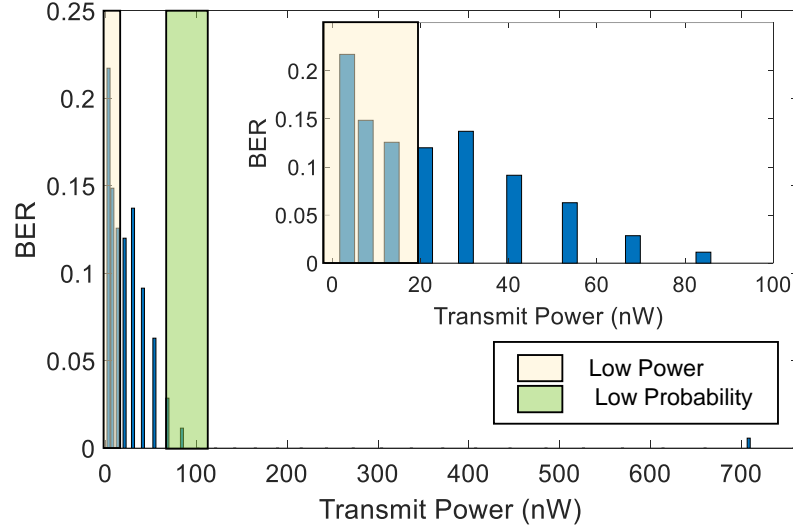


Figure 4.9: Estimated BER when the transmitted power is varied from 10 - 700 nW. Inset highlights two operating regions (1-20 nW and 100nW) where sensitivity analysis has been performed.

The statistical properties of $|W_{(x,y)}^i|$ constrained to pixels defined by the patch $(x, y) \in (P, Q)$ can be quantified by its mean and standard deviation measures which are given by

$$\mu_{(P,Q)}^i = \frac{1}{pq} \sum_{x \in P} \sum_{y \in Q} |W_{(x,y)}^i| \quad (4.5)$$

$$\sigma_{(P,Q)}^i = \sqrt{\left[\frac{1}{pq} \sum_{x \in P} \sum_{y \in Q} (|W_{(x,y)}^i| - \mu_{(P,Q)}^i)^2 \right]} \quad (4.6)$$

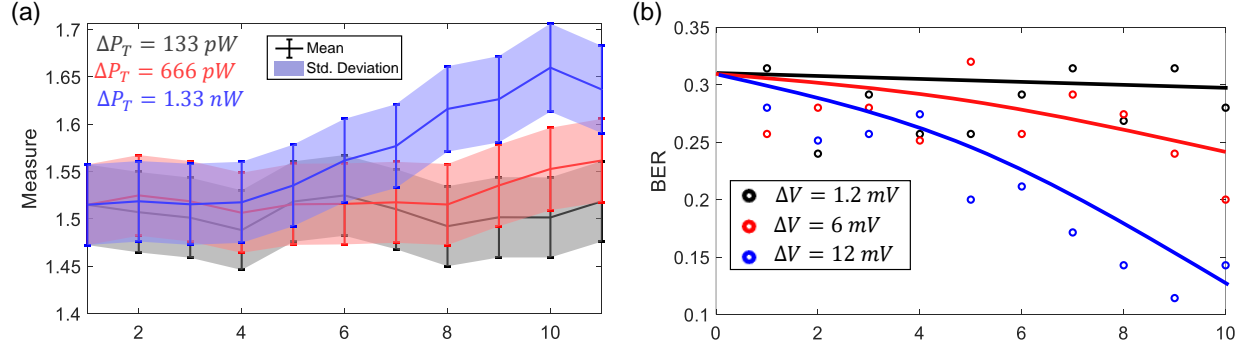


Figure 4.10: Sensitivity analysis in the low BER region where the transmitted power $P_T = 101.5 \text{ nW}$: (a) Mean and std. deviation values of the image patches; (b) the estimated BER when the magnitude of the transmitted pulsed is varied in increments of 1.2 mV-12 mV.

In this work, the algorithm used for decoding the ON (logic level 1) and OFF (logic level 0) states D^i of the transmitter in the i^{th} frame is given by

$$D^i = \begin{cases} 1 & \text{when, } \max [W_{(x,y)ON}^i] > \max [W_{(x,y)OFF}^i] \\ 0 & \text{when, } \max [W_{(x,y)ON}^i] \leq \max [W_{(x,y)OFF}^i] \end{cases} \quad (4.7)$$

Based on the decoded bits, the BER corresponding to the B-scan telemetry can be estimated by taking the ratio between the total number of errors and the total number of frames.

4.3 Results

The experimental setup shown in Fig. 4.2 was used to collect B-scan data for two specific cases: (a) when the submerged ultrasound transmitter is OFF (sample scan shown in Fig. 4.5(a)); and (b) when the transmitter is OFF (sample scan shown in Fig. 4.5(d)). The respective post-processed scans are mapped into Cartesian coordinates as shown in

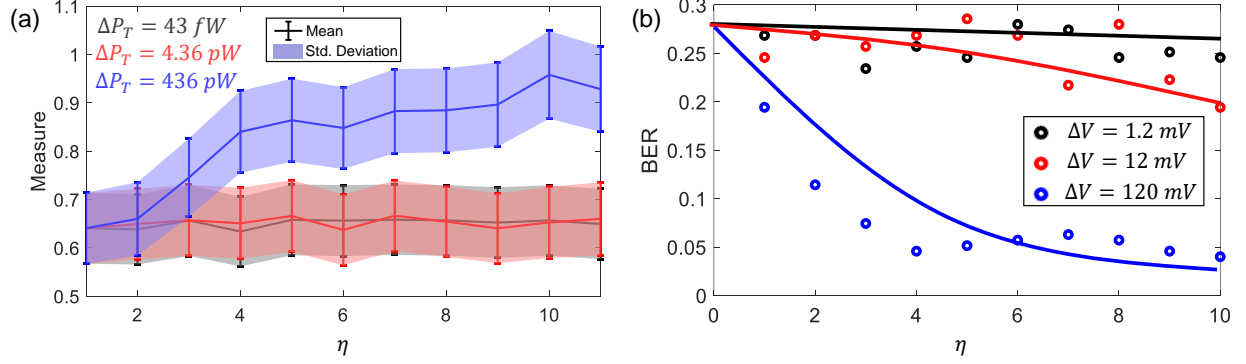


Figure 4.11: Sensitivity analysis in the low BER region where the transmitted power $P_T = 0 \text{ nW}$: (a) Mean and std. deviation values of the image patches; (b) the estimated BER when the magnitude of the transmitted pulsed is varied in increments of 1.2 mV-120 mV.

Fig. 4.5(b)-(e). Fig. 4.5(c),(f) shows the corresponding column-wise average intensity (\vec{I} - defined in equation 4.4), for each of the scans. Fig. 4.6(a)-(c) compares the distribution of the pixel intensities measured in different patches of the scan (R_1, R_2 and R_3 highlighted in Fig. 4.5(a) and R'_1, R'_2 and R'_3 in Fig. 4.5(e)) for the ON and OFF cases respectively. Note that the distributions for the ON and OFF states measured for the patch R_2 are sufficiently different from each other compared to distributions estimated using the other patches.

4.3.1 Quality Metrics

Several experiments were conducted for different levels of transmit power. Some examples of filtered B-scan data are shown in Fig. 4.5(a). Once we identified a target patch in the scan we can quantify the quality of the telemetry signal within the patch using the mean absolute intensity and the standard deviation metrics estimated across the pixel intensities. The BER corresponding to the telemetry signal is estimated according to the decoding algorithm in equation 4.7. The BER metric was then measured for different values of V_{max} which is the

maximum amplitude of the voltage pulse (V_T) used to drive the ultrasound crystal at the transmitter. Using the crystal equivalent circuit shown in Fig. 4.3, the transmitted power can be estimated from V_{max} as the power dissipated at the equivalent resistor R_T . Fig. 4.8 shows the mean and the standard deviation measured estimated for the image patch for different levels of transmitter power P_T . The results show that both the mean and standard deviation of $|W|$ increases with the increase in transmitted power. However, note that both the measures saturate at higher transmit power levels which could be due to the saturation of the B-scan amplifier or due to the limited driving capability of the ultrasound crystal.

4.3.2 BER Analysis

Using the decoder defined in equation 4.7, the transmitted state was estimated which was then used to estimate the BER corresponding to different transmit power levels. The corresponding results are shown in Fig. 4.9. Note that even though the size and the shape of the patch could be varied, we chose a rectangular patch of a specific size that gives the best BER. The BER results in Fig. 4.9 shows that the system performance is optimal when the transmit power level is more than 100 nW and at transmitting power level of 1 nW the measured BER was as high as 0.25.

4.3.3 Sensitivity Analysis

In the next set experiment, we quantified the robustness of the B-scan telemetry system using sensitivity analysis. We characterized the sensitivity for two different regions: (a) when the transmit power P_T was low; and (b) when the system metrics start saturating, as highlighted by the *Low Probability* region in Fig. 4.9. The measured mean and std. deviation are shown

in Fig. 4.10(a) for the case where the magnitude of the driving pulse changed in increments of $\Delta V = [1.2 \text{ mV}, 6 \text{ mV}, 12 \text{ mV}]$ according to $V_{max} = 1.83 + \eta\Delta V$. The corresponding transmit power variations for the voltage increments of 1.2 mV, 6 mV and 12 mV are $\Delta P_T = 133 \text{ pW}$, $\Delta P_T = 666 \text{ pW}$ and $\Delta P_T = 1.33 \text{ nW}$ respectively. The results show no significant improvement in signal quality measure with increments ranging in $\Delta P_T = 133 \text{ pW}$ but the performance deviation is evident when the transmit power is varied in steps of $\Delta P_T = 1.4 \text{ nW}$. This effect can also be seen in the BER plot in Fig. 4.10(b), where the BER change for the case of $\Delta V = 1.2 \text{ V}$ is not significant compared to the case $\Delta V = 6 \text{ mV}$ and $\Delta V = 12 \text{ mV}$ respectively. Similar results corresponding to $V_{max} = 0$ are shown in Fig. 4.11(a). Here the increments in transmitted power $\Delta P_T = [43 \text{ fW}, 4.36 \text{ pW}, 436 \text{ pW}]$ correspond to the voltage increments $\Delta V = [1.2 \text{ mV}, 12 \text{ mV}, 120 \text{ mV}]$. In this case as well, the mean and std. deviation for this data show no significant improvement in signal quality when the transmit power is increased in steps of $\Delta P_T = [43 \text{ fW}, 4.36 \text{ pW}]$ but for the later case of $\Delta P_T = 436 \text{ pW}$ significant improvement in signal quality is observed. This effect can also be seen in the corresponding BER plots shown in Fig. 4.11(b).

4.3.4 Telemetry driven by Unregulated Power Source

The next set of experiments were designed to verify that B-scan telemetry and the decoding algorithm is useful for applications where an unregulated power source drives the ultrasound transmitter. This scenario arises in self-powered systems [55] where the energy harvested from a transducer is used directly to power the telemetry functions without any voltage regulation. For example in our previous work [52] we showed that cardiac valvular perturbations could be exploited to harvest nano-watts to micro-watts of power using a piezoelectric suture. When

and the standard deviation metrics for the noise-modulated ultrasound transmission along with the BER of the decoder estimated at each transmit power level. Note that the decoder BER for this case is similar to the case reported in Fig. 4.12(c) but at much lower levels of transmit power.

4.4 Discussion

Table 4.1 compares this work with the prior work in the area of in-vivo ultrasonic telemetry [45], [56]- [57]. Note that the previous works were geared towards improving the data rates and quality of communication link by exploring different modulation schemes. Our reported data rates are limited by the frame rate of the echoscope which is approximately 27 fps. However, these values should scale if a more advanced ultrasound imaging system with higher frame rates is used. Also, note that the field of view and the number of piezoelectric elements available at the linear transducer array will affect the receive beam-angle which in turn will determine the BER of the proposed B-scan telemetry.

4.4.1 Comparison

In this work, we explored the case where lowering the transmit power is more important than the data rates. This is the case for applications with fixed data-rates or when the implant is located at large depths such as in bone healing applications [63] or spinal-fusion monitoring applications [64]. In these applications, the implant needs to operate at limited energy budgets but the latency in interrogation is not very critical. Also, the use of FDA approved

Table 4.1: Comparison of this work with previous related approaches in terms of transmit power and BER.

Reference	Transducer Size	Pulse Rate	Transmit Power / Voltage	BER
[45]	2 mm	800 Kbps	18 μW	10^{-2}
[56]	2 mm	200 Kbps	4 V	10^{-4}
[58]	1.67 mm ³	125 KHz	600 μW	10^{-4}
[59]	0.045 mm ³	100 Kbps	177 μW	10^{-4}
[60]	9.5 mm	28.12 Mbps	25 V	0.13
[61]	19 mm	70-700 Kbps	8-40 μW	10^{-4}
[62]	741 mm ²	20 Mbps	-	10^{-4}
[57]	3.5 mm	0.6 Kbps	0.38 mW	10^{-5}
This Work	1 mm	27bps	0.83 nW/0.166 V	0.22
This Work	1 mm	27bps	4.1 nW/1.3 V	10^{-2}

ultrasound imaging systems for telemetry would make the translation of this approach more clinically acceptable.

4.4.2 Performance Gain

Comparing the M-scan and B-scan telemetry systems we observed two orders of improvement in signal transmit power when results corresponding to low BER (Fig. 4.1(c) and Fig. 4.9) is achieved at 12 μW and 100 nW receptively. These results correspond to a 21 dB improvement in the SNR value as predicted in section. 4.1.

4.4.3 Unregulated Voltage Source

The results for the case of unregulated voltage source can be considered as an emulation of a telemetry system that is powered by an in-vivo energy harvester. As the energy available at the implant varies the output waveform can be modeled as an amplitude varying voltage source with a set frequency. Note that for the case of higher transmit powers the BER tends to 0 which is very similar to the case of results shown in 4.9. At a particular power level ($P_T = 4.1 \text{ nW}$) the performance is almost comparable to that of $P_T = 50.1 \text{ nW}$ using the stable voltage source and the performance gets worse as P_T is reduced to 1 nW .

4.5 Summary

In this chapter, we showed the feasibility of sub-nano-watt in-vivo telemetry links in a water-medium for implantation depths greater than 10cm. The experimental system comprised of a millimeter-scale piezoelectric crystal, a standard digital pulse-width-modulator, a commercially available echoscope, and a linear array ultrasound transducer. We also presented a simple and yet robust decoding algorithm and we characterized the B-scan telemetry performance using reader sensitivity and bit-error rates. Although the data rates achieved using the proposed scheme are limited by the frame rate of the imager, given modern ultrasound systems [65] that enable imaging at 10000 fps the data rates using B-scan telemetry scale accordingly without affecting the quality (BER) of the communication link. Future work includes validating the B-scan telemetry in-vivo and for different biomedical applications.

Chapter 5

Variance-based Computing

In this chapter, I will investigate an alternate signal representation called variance-based logic (VBL) that can revisit this fundamental limit and provide new insights for designing highly energy-efficient communication and computing schemes. Also, VBL representation enables embedding of rectification and multiplication modules within the primary logic cells, and unlike other energy-recovery logic circuits, the proposed approach obviates the need for any phase synchronization. As a result, VBL representation can be used for designing low-latency digital circuits that are directly powered by the unregulated power source that is energy incident from a remote reader. From an energy point of view logic ‘LOW’ would correspond to an energy sink like a ground plane, which is readily available in most systems whereas logic ‘HIGH’ would represent a random signal with a finite energy fluctuation (or statistical variance) which also readily available for an energy harvesting system. This architecture will eliminate the need for power harvesting and power regulation modules in a conventional energy harvesting or self-powered sensing system which is applicable beyond biomedical implants.

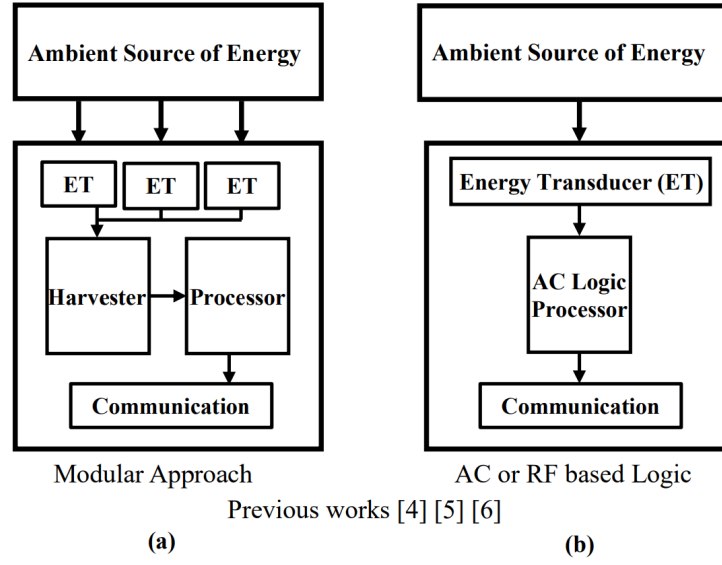


Figure 5.1: (a) Conventional approach where energy is accumulated before the processor and communication modules are activated; (b) AC/RF based logic where the processor is directly driven by the transducer's AC signal.

5.1 Energy Harvesting Sensors

Current energy harvesting systems use a charge multiplying approach to accumulate and store energy on a battery or super-capacitor. This is illustrated in Fig. 5.1(a) where the accumulated energy is used to power the computation and communication module. However, this approach incurs significant latency (or start-up time) [66] as sufficient energy needs to be accumulated to meet the needs of different modules. One of ways to overcome this latency is to eliminate the need for AC-DC conversion, similar to the techniques proposed in [67]- [68]. This approach is illustrated in Fig. 5.1(b) where the logic gates and communication modules are directly powered by the incoming interrogation signal. The principle is very similar to the well known charge recovery logic [69] and adiabatic dynamic logic [70] where complementary logic computation is performed in each of the respective phases of the AC signal. However, this requires some form of phase and frequency synchronization which is difficult to achieve

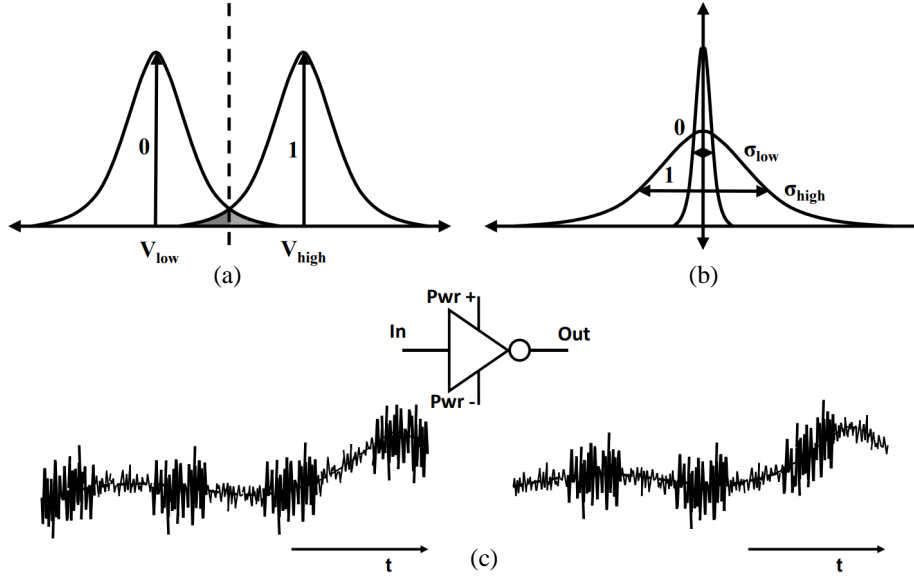


Figure 5.2: (a) Logic representation for both conventional and AC coupled logic; (b) proposed variance based logic representation; (c) Waveforms of the signal observed at the input and output of an VBL based NOT gate.

in practical conditions. Also, this approach does not scale when multiple sources of energy (with different frequency and impedance characteristics) are available.

5.1.1 Variance-based Processors

To overcome the limitations of the conventional and the AC coupled approaches, we present an alternative approach to digital logic design that is more amenable to energy harvesting systems. The approach uses the statistical variance of the signal instead of the signal's statistical mean to represent different logic levels. The variance-based logic (VBL) representation enables embedding of rectification and multiplication modules within basic digital logic units and unlike AC-coupled or energy-recovery logic circuits the proposed approach obviates the need for any phase synchronization.

5.2 VBL based Digital Circuits

Conventional energy-harvesting devices use power harvesting circuits to rectify and regulate the available ambient energy in a manner that results in two binary signal levels (V_{high} and V_{low}). These signal levels typically represent the Boolean logic states (denoted by 0 and 1) and is used in the evaluation and representation of different types of digital functions. Because real-world signals are noisy these binary levels are statistically represented by their probability distributions that are centered about their respective means V_{low} and V_{high} , as shown in Fig 5.2 (a). The variance of each of the distribution captures the effect of noise and signal fluctuations which is a function of the operating environment and applications respectively. In the proposed VBL, as illustrated in Fig 5.2 (b), logic 0 is represented by a probability density function (PDF) with a small variance (σ_{low}) whereas logic 1 is represented by a PDF with a large variance (σ_{high}). Note that the respective means for both the distributions are the same (shown as 0 in Fig. 5.2(b)), unlike the conventional representation which is shown in Fig 5.2 (a). From an energy harvesting point of view, logic 0 (signal with low variance) could correspond to an energy-sink like a ground plane (or a large capacitor), that is readily available in most systems. Whereas, logic 1 (signal with high variance) could be represented by a random signal with a finite energy, which could be the ambient energy source. Fig 5.2 (c) shows an example signal representation for a VBL based NOT gate where a bit sequence 1,0,1,0,1 applied to the input. Note that the signal variance (within a finite measurement window) switches according to the bit-sequence, whereas the signal mean (which is unimportant in the proposed representation) could potentially drift. The output of the VBL based NOT gate produces a complementary sequence as represented by the switching of the variance of the signal.

5.2.1 Variance-based Logic Gates

To understand how a variance-based logic can be implemented at a circuit level, consider a generic architecture of any combination logic, as shown in Fig. 5.3(a). This architecture can be viewed to comprise of a measurement module and a transformation module. The measurement module determines the state of the input signal, which for a conventional logic, would be by measuring the signal mean. For instance, a CMOS implementation of a conventional logic achieves this by averaging the input signal on a capacitor (typically the gate-capacitance of a MOSFET transistor), as shown in Fig. 5.3(c) for the case of an inverter (Fig. 5.3 (b)). The transformation module (Fig. 5.3 (d)) then generates the output signal state by selectively switching the load C_{Load} , to gnd or to V_{dd} through Z_L depending on the measured input state. This is illustrated for a conventional NOT gate, where the switch can be implemented using an NMOS transistor and the load Z_L can be a PMOS transistor. Similarly, for a variance-based logic the measurement module would need to determine the state of the input variance (high or low) using one of several approaches: (a) measure the energy of the input signal; or (b) use a peak detector to track the maximum deviation of the input signal. Fig. 5.3 (f) shows a simple peak detector stage (formed by the diode D, an NMOS N and a capacitor C_m) that could be used for measuring the variance of the input signal. Once the state of input signal variance has been determined, similar to the conventional logic, the transformation module for a variance-based logic can simply couple or decouple the ambient energy source (labeled as Pwr+ in Fig. 5.3 (g)) to the output through a coupling capacitance C_L . A gate controlled NMOS transistor ($=V_{control}$), as shown in Fig. 5.3 (f), implements a leakage resistance which ensures that the variance measured during the previous cycle is erased before the measurement is repeated. Note that there can be several ways to implement the erase functionality that could yield better performance in

terms of speed and energy-efficiency. Fig. 5.3 (e) shows a general implementation of NOT gate using Variance based logic where the source of power could be any combination of Pwr1, Pwr2 or Pwr3 indicating the operation of gate using multiple coupled sources. In particular, Pwr2 could be a primary power source (for e.g. vibration), Pwr1 could correspond to a supplementary AC source (strain variations) and Pwr3 could be a DC coupled source (for e.g. a solar-cell). Using the basic measurement and transformation circuits shown in Fig. 5.3 (f)-(g), the proposed variance-based logic could be extended to implement other logic functions like a NOR gate or a D-FlipFlop. Note that the example circuit shown in Fig. 5.3 (d) implements only a single-ended variant of the variance-based logic where only one of the outputs from an energy transducer is used. Most energy transducers (piezoelectric transducer or an RF antenna) are fully-differential in nature, so a fully-differential implementation would be required to exploit the entire range of signal variance.

5.3 Measurement Results

We have implemented basic VBL based circuits like inverters, ring-oscillators, and NOR logic gates in a $0.5\ \mu\text{m}$ CMOS process and Fig. 5.4 shows the micrograph of the fabricated prototype. For the measurement results presented in this section, the value of the leakage resistance (determined by $V_{control}$) and the coupling capacitance C_L were chosen such that the logic circuits could be driven at a desired frequency. The energy source (high-variance source) in all these experiments were emulated using a 100KHz $2V(=V_{pp})$ source and the logic transitions were generated using square-wave modulation with a frequency of 500 Hz. The measured result corresponding to a NOT gate is shown in Fig. 5.5 for different values of the leakage resistance (or control-gate voltage $V_{control}$). The results confirm the functionality

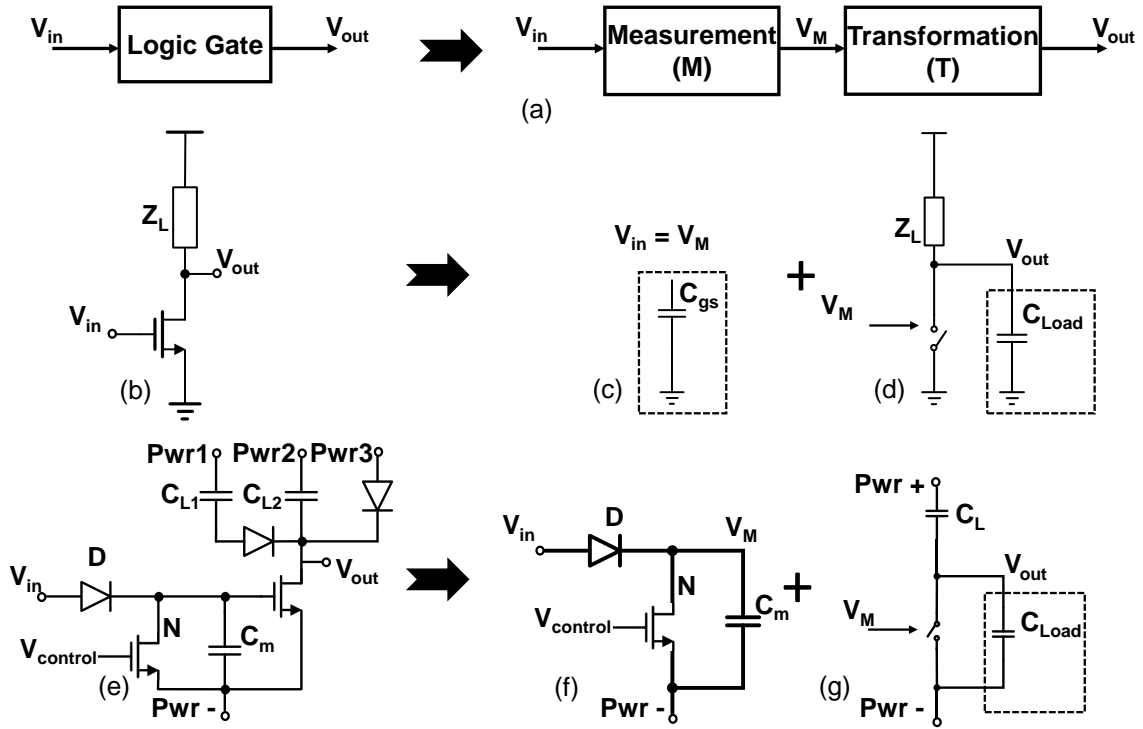


Figure 5.3: (a) Implementation of a generic logic gate as a combination of measurement and transformation modules. (b) Schematic of a NOT logic gate using a conventional approach – formed using circuit for (c) measuring the signal mean and (d) transforming the output signal based on the mean. (e) Equivalent implementation of a variance-based NOT gate where (f) and (g) show the corresponding variance measurement and transformation modules.

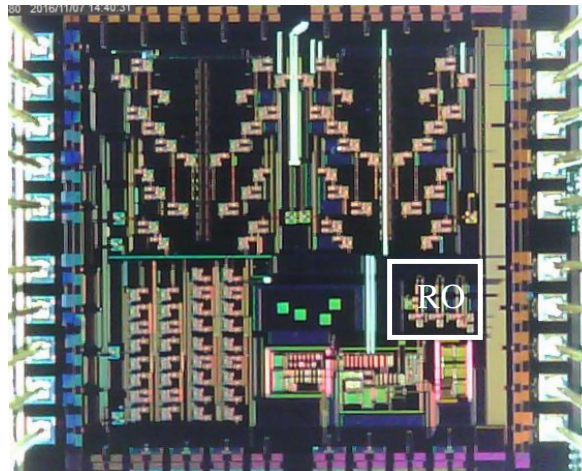


Figure 5.4: Micrograph of the fabricated chip in a $0.5 \mu\text{m}$ CMOS process.

of VBL based NOT gate where the output variance switches from low to high when the input variance switches from high to low. Also, as shown in Fig. 5.5, smaller values of the leakage resistance (larger value of $V_{control}$) produces different rise-times (delays). The next set of measurements verified the functionality of a 3-stage ring-oscillator (RO) and Fig. 5.6 shows the measured oscillation frequency when both $V_{control}$ and the magnitude of the input signal frequency (or input energy) is varied. The measured results show that the output frequency of the VBL based RO is strong function of the input energy (which is expected) and a function of the leakage resistance. Therefore, the RO frequency seems to adjust itself to the available input energy which is really important in energy harvesting systems.

The measured responses from the VBL based logic cells could be used to generate a behavioral model and to synthesize more complex processing units, similar to the conventional logic synthesis approach. In the next set of experiments we used the VBL logic cells to implement a 4-bit Johnson counter that is directly driven by a random energy source. For comparison we implemented an equivalent counter using conventional logic cells and is driven by a power conditioning unit formed by a rectifier and a multiplier. Fig. 5.7 (a) shows the output waveform (Q0-Q4) of a conventional 4 bit ring counter that is clocked at a frequency of 10KHz and powered by a regulated 3-stage voltage multiplier. The shaded region in the plot of around 2.8 ms duration illustrates the startup latency of the rectifier/multiplier, which is the time taken to reach the steady-state voltage of 3V. For the VBL-based counter, a Gaussian noise-source is used as an input. The corresponding waveforms for each stage of the counter (Q0-Q4) are shown in Fig. 5.7 (b). The waveforms indicate that VBL based counter demonstrates a latency of 50 μ s and completes two cycles of operation by the end of 0.8 ms. This result clearly shows the advantage of the proposed VBL-based digital circuits to design low-latency digital circuits. This attribute would be important for designing real-time wireless interrogation circuits for IoTs.

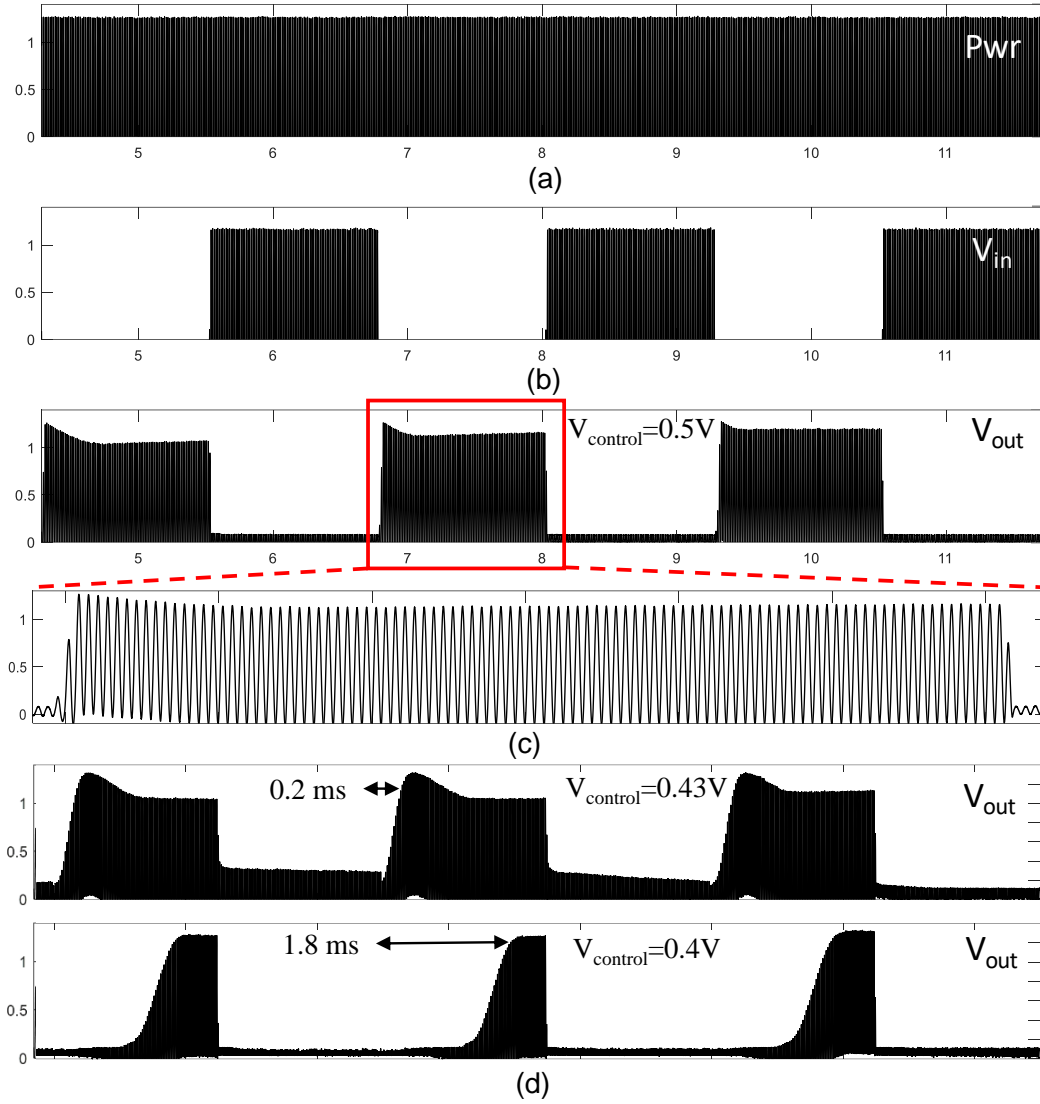


Figure 5.5: (a) Power source (Pwr), (b) Input signal (V_{in}) and (c)-(d) Measured output response of a VBL-based NOT gate for different values of $V_{control}$.

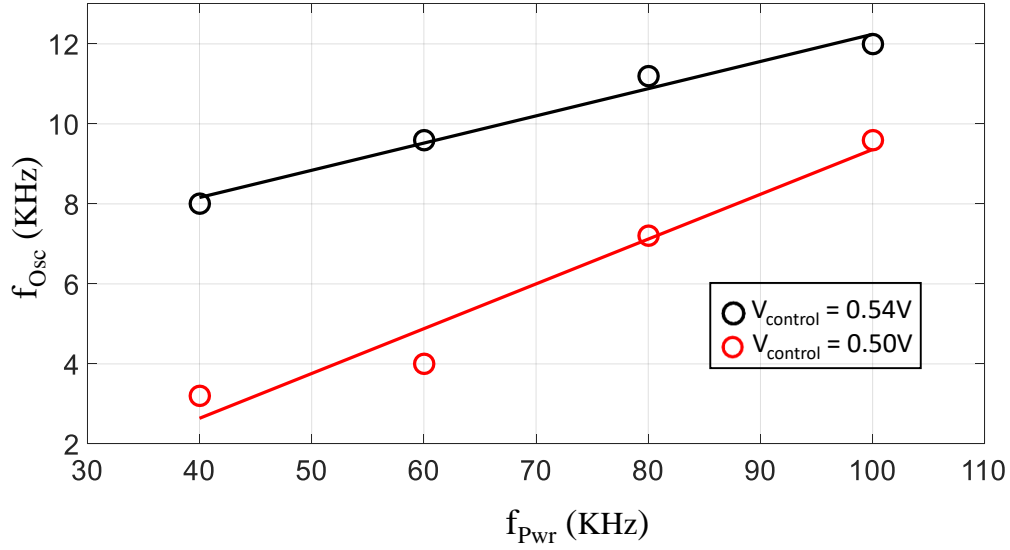


Figure 5.6: Measured oscillation frequency of a 3-stage VBL ring oscillator when the frequency of power source is varied from 40 KHz to 100 KHz.

5.4 Summary

Analysis presented in this chapter provides an alternate and novel approach for building logic gates that operate on the statistical variance of the input signal, which we call variance-based logic. The approach could potentially combine the functionalities of energy harvesting and digital computation and the approach could be applied to a wide variety of energy transducers. With help of prototype, we have demonstrated the performance of basic digital cells and proposed the feasibility of a simple state machine. The advantage of this new logic design in terms of power and delay, when compared to the conventional logic gates, is unknown and is the subject of future research in this area. Another benefit of using variance-based logic is that the reciprocity of the energy transducer (like an RF antenna) which can be used to wirelessly transmit logic-state information. In fact, variance-based logic shares similarity with load-modulation techniques that are commonly used in back-telemetry for passive RFIDs.

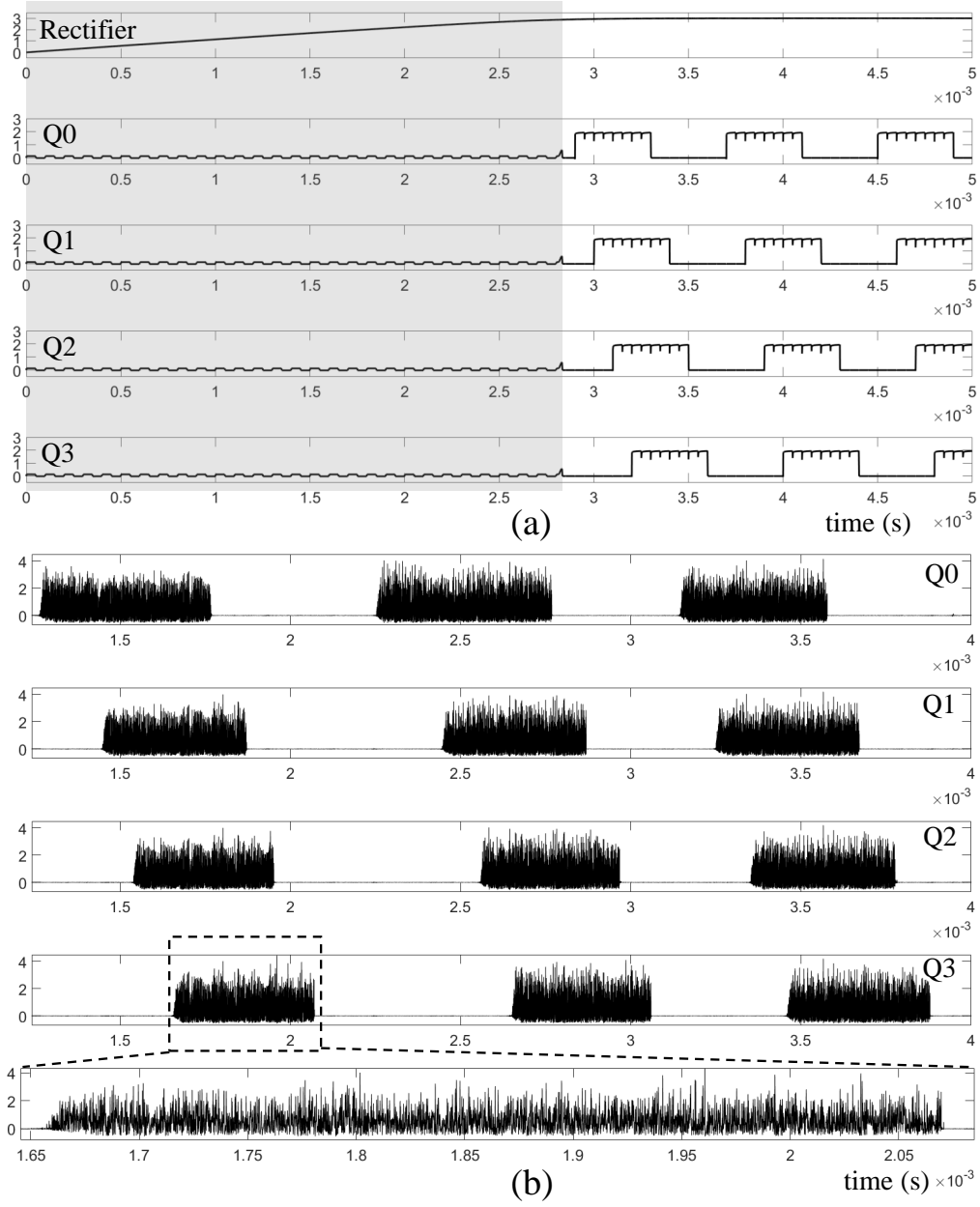


Figure 5.7: Simulation results of a 4 bit johnson counter using: (a) conventional logic gates; and (b) using VBL based gates.

Chapter 6

Variance based Logic

Variance-based logic (VBL) uses the fluctuations or the variance in the state of a particle or a physical quantity to represent different logic levels. In this chapter I show that compared to the traditional bi-stable logic representation the variance-based representation can theoretically achieve a superior performance trade-off (in terms of energy dissipation and information capacity) when operating at fundamental limits imposed by thermal-noise. In addition to the universal $KT \ln(1/\epsilon)$ energy dissipation required for a single bit flip, a bi-stable logic device needs to dissipate at least $4.35KT/\text{bit}$ of energy, whereas under similar operating conditions, a VBL device reduces the additional energy dissipation requirements down to sub- KT/bit . These theoretical results are general enough to be applicable to different instantiations and variants of VBL ranging from digital processors based on energy-scavenging or to processors based on the emerging valleytronic devices.

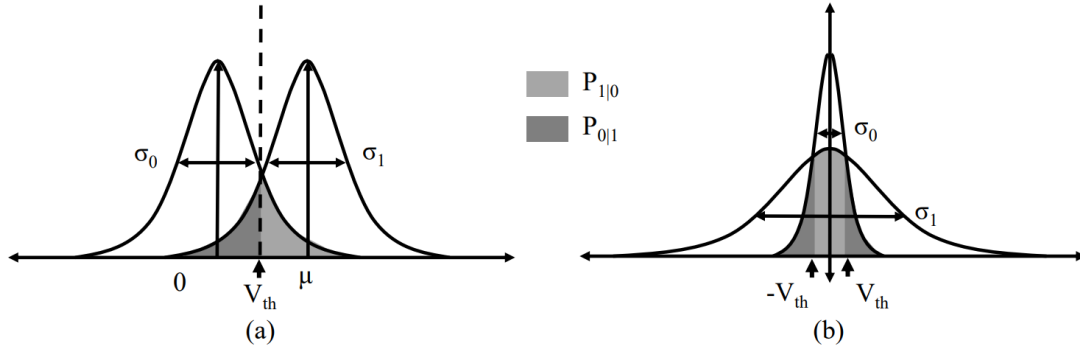


Figure 6.1: Statistical representation of binary logic states '0' and '1' using (a) Mean-based Logic (MBL) and (b) Variance-based Logic (VBL).

6.1 Digital Systems

At a fundamental level any form of digital operation involves repeated and controlled transition between the two logic states. Traditionally a digital system can be represented using a potential well diagram where the two states (0 and 1) are separated from each other by an energy barrier. The potential wells are assumed to be stable configurations and any fluctuation or variance in these configurations is treated as noise. For example, in a standard CMOS logic the states are represented by the signal mean (average voltage or current) and the signal variance captures the effect of thermal fluctuations or environmental interference. For a spintronic device [71] the logic states are represented by the state of magnetic spin of the electrons; in a phase-change device like memristor [72] or FeRAM [73] the logic states are represented by the static alignment of domains or individual molecules in the dielectric material.

6.1.1 Mean-based Logic

From a statistical point of view, the two logic states (denoted by '1' and '0') are represented by the means (0 and μ) of the two probability distributions that are separated from each other by an energy-barrier, as shown in Figure 6.1(a). Note that since the physics of the two configurations are assumed to be similar, the variances of the distributions can be assumed to be equal and the probability of error can be estimated by the overlap of the distributions (shown in Fig. 6.1(a)). We refer this mode of representation as Mean-based Logic(MBL).

6.1.2 Variance-based Logic

Alternatively, we investigate a new logic representation where instead of the mean, the variance in the state configurations are used for representing logic levels 0 and 1. The statistical representation of the variance-based logic (VBL) [55] is shown in Fig. 6.1(b) where logic '0' is represented by a configuration with small fluctuations (or variance), and logic '1' is represented by a configuration with large fluctuations (or variance). Note that in Fig. 6.1(b), the two distributions have the same mean value which therefore does not carry any logic information. Also note that VBL representation is different from a noise based logic (NBL) [74] where the orthogonal patterns of noise carried the digital information, unlike the change in signal variance in the case of VBL.

VBL is applicable to devices and systems where the shape of the energy levels (or equivalently the momentum of the particles) can be changed. One such example is a system that is powered by scavenging energy from ambient sources. In this case, the asymmetry in the electrical impedance seen by the system ground and as seen by the energy transducer leads to different variances in voltage levels at the supply and at the ground potential. In [55] we

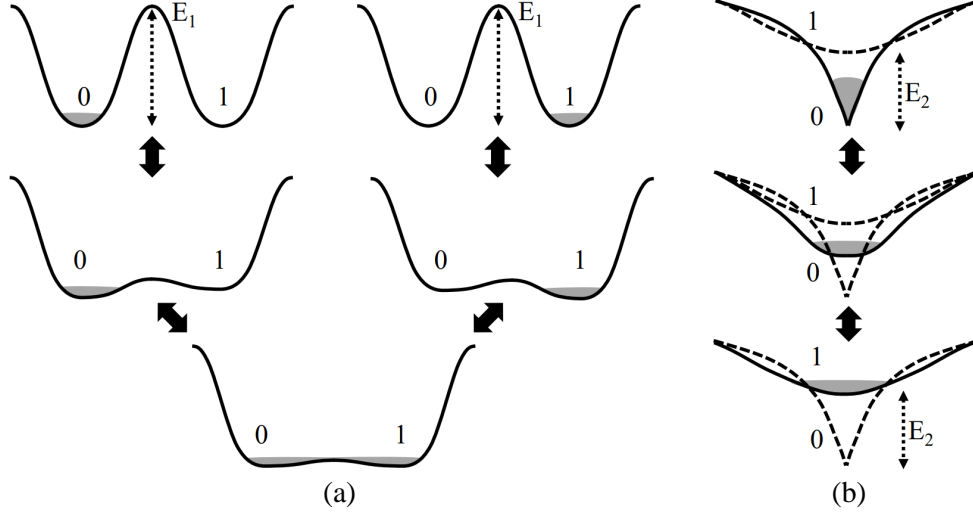


Figure 6.2: The process of logic transition corresponding to (a) MBL and (b) VBL.

have exploited the voltage variances to implement different forms of VBL logic gates and circuits. Another example where VBL could be applicable are processors based on valleytronic devices [75] where the curvature of the energy-levels (or equivalently the momentum of the particle trapped in the energy-level) could be changed to represent different logic levels. Our goal is to abstract out the physical level implementation of VBL and investigate the energy-efficiency limits of VBL as determined by thermal-noise.

6.1.3 Mean vs Variance

Based on the potential well model, the energy-efficiency of VBL can be compared to the traditional mean-based logic (MBL) by visualizing the process of logic transition, as shown in Fig. 6.2(a) and (b). For a specific implementation of MBL the logic transition can be realized by transferring electrons from one potential well to another [76], [77], as shown in fig. 6.1(a). During the logic transition (0 to 1 for example), the energy barrier is lowered and the potential wells are reshaped in a way that the electrons move to the potential well corresponding to

logic 1. The energy barrier E_1 is then restored and held until the next transition. Assuming irreversible computation and adiabatic transport of the electrons between the potential wells, the energy dissipated per logic transition or a bit for MBL, can be estimated to be twice the height of energy barrier ($E_{MBL} \approx 2 \times E_1$). The thermodynamic limits on E_1 is determined by the minimum energy required to enforce logic state transition and is atleast $KT \ln(2)$ Joules when the information content carried is close to zero. [78]. Note that this energy limit is independent of logic implementation or realization of the logic circuit. However, when the energy dissipated due the process of measurement is taken into account, a different lower-bound on the energy-dissipation per bit is obtained [79]. On the other hand, in a VBL device (as depicted in Fig. 6.2(b)) the electrons are either constrained in a narrow potential well (a low variance state '0') or the electrons are relatively free to move around in a broader potential well (a high variance state '1'). Transition between the logic states in VBL involves changing the shape of the potential well and hence involves adding or subtracting a fixed amount of energy E_2 ($= E_{VBL}$) from the system, as shown in Fig. 6.2(b). In our analysis, we derive the lower bounds on energy dissipation (E_{VBL}) for VBL and compare it with E_{MBL} .

6.2 Energy-per-bit for MBL and VBL

6.2.1 Estimation of Probability of Bit Error

Following an approach that was presented in ref. [79], we first calculate the information capacity for MBL and VBL by estimating the average probability of error p_{avg} that is incurred

in measuring the two logic levels. This is given by,

$$p_{avg} = p_0 p_{1|0} + p_1 p_{0|1} \quad (6.1)$$

where p_0, p_1 are prior probabilities for logic state to be '0' or '1', and $p_{1|0}, p_{0|1}$ are conditional probabilities that captures incorrect measurement in the logic state. In an MBL representation as shown in Fig. 6.1(a), a threshold V_{th} could be used to distinguish between the logic levels in which case $p_{1|0}, p_{0|1}$ is given by the overlap between the distributions. Assuming equal apriori probability $p_0, p_1 = 0.5$ and the conditional distributions to be Gaussian with respective means 0 and μ and variances σ_0^2 and σ_1^2 , the average probability of error [80] can be estimated as

$$p_{avg,MBL} = \frac{1}{4} [erfc(\frac{\mu - V_{th}}{\sqrt{2}\sigma_1}) + erfc(\frac{V_{th}}{\sqrt{2}\sigma_0})] \quad (6.2)$$

where,

$$erfc(x) = \frac{2}{\sqrt{\pi}} \int_x^\infty e^{-t^2} dt. \quad (6.3)$$

In case of VBL, the variances σ_0^2 and σ_1^2 corresponding to the two logic states could be measured by comparing the magnitude of the signal with respect to a threshold $\pm V_{th}$. The probability of error ($p_{avg,VBL}$) is determined by the shaded region as shown in Fig. 6.1 (b). Following equation 6.1 and assuming equal apriori probabilities, the average probability of error $p_{avg,VBL}$ can be estimated as

$$p_{avg,VBL} = \frac{1}{2} [1 - erfc(\frac{V_{th}}{\sqrt{2}\sigma_1}) + erfc(\frac{V_{th}}{\sqrt{2}\sigma_0})]. \quad (6.4)$$

6.2.2 Estimation of Channel Capacity

Maximum information rate can be estimated by applying Shannon's capacity equation to an binary asymmetric channel with error probabilities $p_{0|1}$ and $p_{1|0}$ and is given by

$$C(p_{0|1}, p_{1|0}) = f_c [1 + p_1 \{p_{0|1} \ln(p_{0|1}) + p_{1|1} \ln(p_{1|1})\} + p_0 \{p_{1|0} \ln(p_{1|0}) + p_{0|0} \ln(p_{0|0})\}] \quad (6.5)$$

where f_c is the rate (or equivalently the speed) at which the logic state is measured.

6.2.3 Estimation of Power Dissipation

The next step towards determining the energy efficiency of MBL and VBL is to estimate the energy dissipated during the process of logic transition. Similar to the approach presented in [79] we realize both the logic by measuring an equivalent signal (mean or the variance) on an equivalent capacitance C_{meas} . For an MBL, the energy is dissipated during charging and discharging the sampling capacitor ' C_{meas} ' to voltage μ at a rate of f_c and the average power dissipation is given by

$$P_{MBL} = f_c \times \frac{1}{2} C_{meas} \mu^2. \quad (6.6)$$

For a VBL, the energy dissipation would be given by the difference in the signal variance corresponding to the two logic states and the average power dissipation is given by

$$P_{VBL} = f_c \times C_{meas} (\sigma_1^2 - \sigma_0^2) \quad (6.7)$$

6.2.4 Figure-of-Merit

The Energy dissipated per bit (or the figure-of-merit for comparison) is then given by

$$FOM_{MBL,VBL} = \frac{P_{MBL,VBL}}{C(p_{0|1}, p_{1|0})}. \quad (6.8)$$

Note that the FOM is a function of probabilities $p_{1|0}$ and $p_{0|1}$ which in turn depend on the variances σ_0^2 , σ_1^2 corresponding to the logic states 0 and 1 respectively. Since our objective is to determine the fundamental limits for MBL and VBL as constrained by thermal noise, we will assume $\sigma_0^2 = KT/C_{meas}$. Figure 6.3 (a) compares the FOM numerically estimated for MBL and VBL using equations 6.2- 6.8 and for different values of V_{th} , σ_1^2 . The figure shows that for the FOM for MBL is bounded from below and approaches a fundamental limit of 4.35 KT/bit. This limit is different from what was previously reported in [79] and therefore in this section we provide a brief derivation of this limit.

6.3 Comparison Analysis

Revisiting the approximation provided in ref. [79] it can be seen that the capacity of MBL (C_{MBL}), when operating near the average probability of error $p_{avg} = p \approx 0.5$. Assuming a binary symmetric channel with $\sigma_1 = \sigma_0$, the Shannon capacity equation given by equation 6.5 can be rewritten as

$$C_{MBL}(p) = f_c[1 + p \log_2 p + (1 - p) \log_2(1 - p)]. \quad (6.9)$$

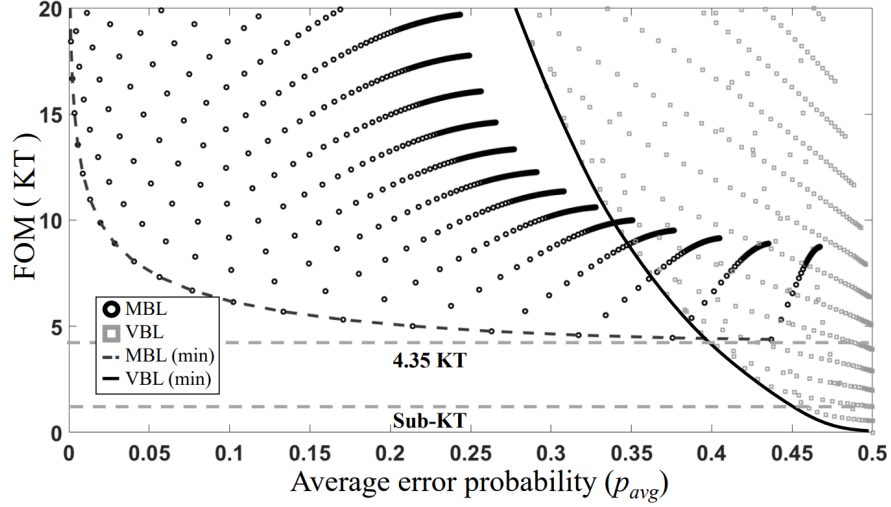


Figure 6.3: Numerical estimated FOM (energy dissipated per bit) corresponding to MBL and VBL for different values of V_{th} and σ_1 .

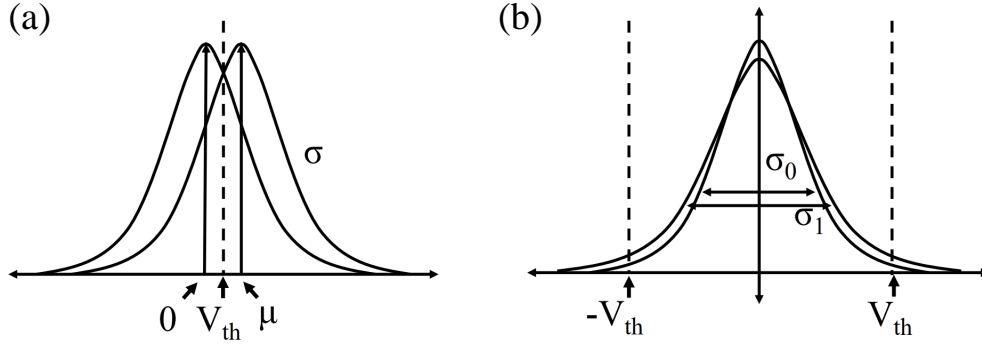


Figure 6.4: (a) Statistical distributions and thresholds corresponding to the MBL operating at the 4.35KT per bit fundamental limit; and (b) VBL operating at sub-KT per bit fundamental limit.

Defining Δp as $\Delta p = p_{avg} - 0.5$ and using a Taylor series expansion of C_{MBL} around $p_{avg} = p = 0.5$, equation 6.9 leads to,

$$\begin{aligned} C_{MBL}(\Delta p)|_{p \approx 0.5} &= C(p) + \frac{C'(p)}{1!} \Delta p + \frac{C''(p)}{2!} \Delta p^2 + \dots \\ &= \frac{2}{\ln 2} f_c(\Delta p)^2 \end{aligned} \quad (6.10)$$

Assuming that the variance of measurement $\sigma_0^2 = \sigma_1^2 = \frac{KT}{C_{meas}}$ as determined by thermal-noise and $V_{th} = \frac{\mu}{2}$, Δp is given by

$$\Delta p \approx \frac{g(0)\mu}{2} = \frac{\mu}{2\sqrt{2\pi}\sigma} = \frac{\mu}{2\sqrt{2\pi KT/C_{meas}}} \quad (6.11)$$

where $g(\cdot)$ is the Gaussian distribution function. Using Eq. (6.10), the capacity is given by

$$C_{MBL}|_{p \approx 0.5} = \frac{\mu^2}{(4\pi \ln 2) \frac{KT}{C_{meas}}} f_c \quad (6.12)$$

which leads to the fundamental FOM limit as

$$FOM_{MBL|min} = \frac{P_{MBL}}{C_{MBL}|_{p \approx 0.5}} \approx 4.35KT/bit. \quad (6.13)$$

This limit has been verified using numerical simulation and the results are summarized in Fig. 6.3. It can be also seen in Fig. 6.4(a) that the FOM limit for VBL could be lower than the MBL limit and in some cases the FOM approaches sub-KT per bit. For VBL sub-KT per bit limit is achieved when the respective variances σ_0 and σ_1 are approximately equal (implying $p_{avg} \approx 0.5$) and the threshold V_{th} samples only the tails of the distribution, as shown in Fig. 6.4(b). To understand why VBL can achieve sub-KT per bit limit, in Fig. 6.5 we compare the channel capacity $C(p_{0|1}, p_{1|0})$ for MBL and VBL, numerically estimated for

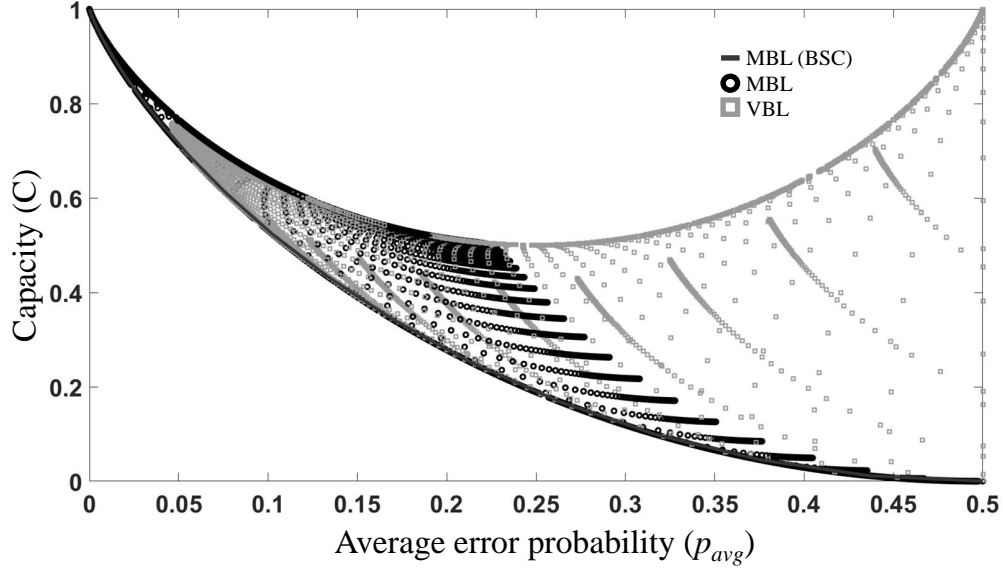


Figure 6.5: Comparison of numerically estimated information capacity C as a function of the average probability of error p_{avg} , corresponding to MBL and VBL and for different values of V_{th} and σ_1 .

different values of V_{th} and σ_1 . Fig. 6.5 shows that while for MBL the information capacity approaches zero when the $p_{avg} \approx 0.5$, this is not the case for some instances of VBL when V_{th} is located around the tails of the distribution. In the above derivation, we have ignored the energy incurred by the switching circuit to convey the VBL levels, albeit the logic ‘0’ and ‘1’. For VBL, the switch will effectively control the width of the potential well, shown in Fig. 6.2 (b), which in turn will change the noise-variance. Therefore, the energy dissipation to convey one bit of information is also determined by the minimum energy dissipated to trigger a switch, which is $KT \ln(1/\epsilon)$, ϵ being the probability of error in case of VBL. [78, 81]. In the limit of $\epsilon = 0.5$, this will result in the Brillouin limit of $KT \ln(2)$ which needs to be added to the lower bound of VBL.

6.4 Discussion and Summary

In [82] it was proposed that one of methods to approach the fundamental limit of energy-dissipation for MBL was to use error-correcting codes to compensate for high p_{avg} . A more practical approach would be to first boost the signal-to-noise ratio (SNR) of the measurement through repeated sampling and statistical averaging. Given N independent and identically distributed (iid) random samples x_1, x_2, \dots, x_N from a distribution with mean μ and variance σ^2 , the sample mean (\hat{x}) is defined as $\hat{x} = \frac{\sum_{i=1}^N x_i}{N}$ and sample variance is given by $\hat{\sigma}^2 = \frac{\sum_{i=1}^N (x_i - \hat{x})^2}{N-1}$. The signal-to-noise ratio (SNR) for the measurement is given by

$$SNR = \frac{E[\hat{x}]^2}{E[\hat{\sigma}^2]} \quad (6.14)$$

In case of MBL, it is given by

$$SNR_{MBL} = \frac{N\mu^2}{\sigma^2} \quad (6.15)$$

Even if the samples are drawn from any given probability distribution the definition of SNR_{mean} holds. Where as the variance of the sample variance becomes a function of fourth order moment and is estimated to be [83]

$$E[(\hat{\sigma}^2 - \sigma^2)^2] = \sigma^4 \left[\frac{2}{(N-1)} + \frac{\kappa}{N} \right] \quad (6.16)$$

where κ is the kurtosis of the probability distribution. A generalized expression for SNR_{var} is given as

$$SNR_{VBL} = \frac{1}{\frac{2}{(N-1)} + \frac{\kappa}{N}} \quad (6.17)$$

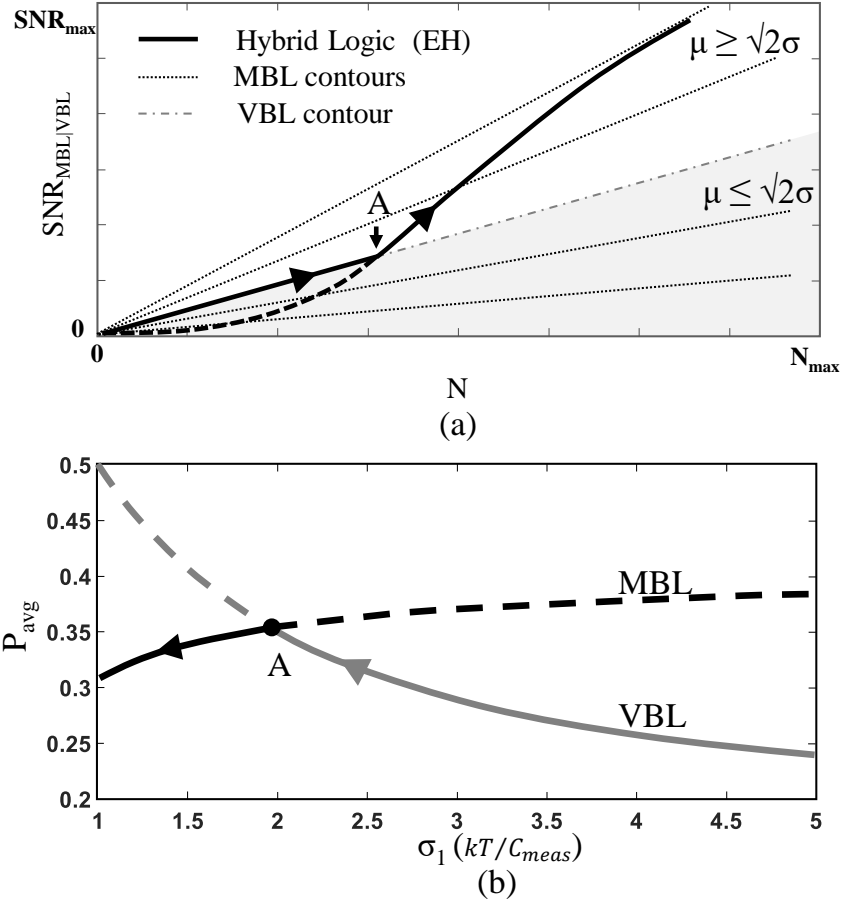


Figure 6.6: Rationale for a hybrid logic that combines MBL and VBL - (a) plot showing regions where VBL (or MBL) yields a higher SNR compared to MBL (or VBL) with 'A' being the transition point between the two logic topologies; (b) plot showing the variation in the average probability of error p_{avg} for different values of σ_1 with 'A' being the transition point to switch between MBL and VBL.

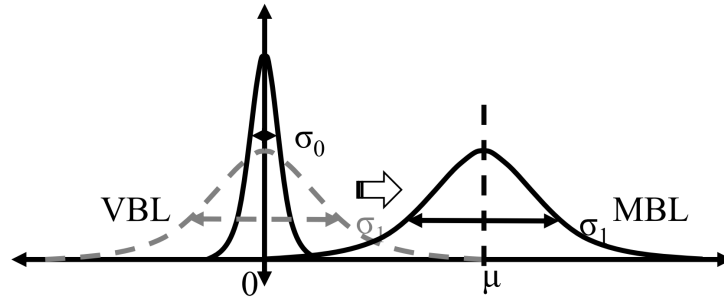


Figure 6.7: Transition between VBL to MBL in an energy-scavenging system.

It can be seen that SNR_{MBL} , shown in equation. 6.15, increases with increase in μ and N and with the decrease in variance (σ^2). On the other hand SNR_{VBL} , shown in equation. 6.17, is independent of parameter σ and only increases with N . In Fig. 6.6(a) we show the regions where $SNR_{VBL} \geq SNR_{MBL}$ and $SNR_{VBL} \leq SNR_{MBL}$.

6.4.1 Hybrid Logic

The result shown in Fig. 6.6(a) indicates that VBL and MBL techniques could be combined to form a hybrid logic topology where VBL is used when $\mu \leq \sqrt{2}\sigma$, and MBL is used when $\mu \geq \sqrt{2}\sigma$. The scenario occurs in energy scavenging processors [84] where the ambient energy (for example radio-frequency signals or vibrations) could serve as source of high-variance. In a traditional approach, the source of energy is harvested and rectified to create a stable voltage level μ which could then be used to implement MBL based processing. This process is illustrated in Fig. 6.7 where during the startup phase $\mu \leq \sqrt{2}\sigma$ is satisfied and therefore VBL would be more attractive. As more energy is harvested and rectified, $\mu \geq \sqrt{2}\sigma$ it is more attractive to use MBL for computing. The proposed hybrid logic should also provide improvements in reliability as the variance of the logic level σ_1 reduces in addition to the increase in μ . Fig. 6.6(b) shows the estimated p_{avg} corresponding to MBL and VBL when σ_1 is varied. The comparison shows an optimal transition point labeled as 'A' where switching the logic style from VBL to MBL yields a better reliability in terms of p_{avg} . Future work would entail practical implementation of the hybrid logic using topologies similar to that of [55] and comparing its performance with other energy harvesting logic topologies [84, 85].

Chapter 7

High Dimensional VBL

Is there a fundamental advantage in encoding information by modulating the variance of a signal rather than modulating its mean? This chapter, provides mathematical and geometric insights into this question by comparing the fundamental limits on the minimum energy-per-bit that can be achieved by a variance-based logic (VBL) and a mean-based logic (MBL) representation. We argue that while for MBL, the trade-off between the energy-per-bit and the bit-error-rate is fundamentally constrained, using VBL it is possible to achieve a better trade-off compared to MBL. This result has been experimentally verified for an Additive-white-Gaussian-Noise (AWGN) channel using numerical and monte carlo simulations.

7.1 Limits of VBL

There exists a trade-off between the energy required for transmitting information across a noisy communication channel and the reliability of correctly decoding the transmitted information. This trade-off manifests itself as the celebrated Shannon-limit [86], which determines the minimum energy-per-bit (E_b/N_0) that is required to achieve arbitrary small

bit-error-rate (BER) for a given communication channel. We argue that the Shannon-limit for an alternate signal representation can provide a better trade-off such that a communication system can potentially achieve arbitrarily small BER while dissipating near-zero energy-per-bit. The proposed representation is based on previously reported variance-based logic (VBL), where the information bits are encoded as changes in signal variance [55]. This logic representation is contrary to the conventional mean-based logic (MBL) where the information is encoded as the change in the mean of a signal property, for instance, the signal amplitude or its phase or its frequency [87, 88]. Both MBL and VBL representations are illustrated using a standard communication model in Fig. 7.1(a). For a one-dimensional (1D) MBL, the probability density function (PDF) of the channel input (\mathbf{X}) is modeled using two Dirac-delta functions located at logic levels '0' and '1', as shown in Fig. 7.1(b). Note that this abstraction is independent of the physical implementation of MBL using amplitude-shift keying (ASK), frequency-shift keying (FSK) or phase-shift keying (PSK). If the noise in the communication channel (\mathbf{W}) is assumed to be additive, as illustrated in Fig. 7.1(a), then the output of the channel is $\mathbf{Y} = \mathbf{X} + \mathbf{W}$, and its corresponding PDF is given by two overlapping probability distributions, as shown in Fig. 7.1(b). For 1D VBL (shown in Fig. 7.1(c)), the input logic levels are encoded by PDFs with a low and high variance which translates to an output PDF with low and high variances. The key difference between the MBL and VBL representations is the decoder used to differentiate between the logic levels at the receiver. The optimal decoding boundary for 1D MBL is shown in Fig. 7.1(b) and lies at the intersection of the two distributions, whereas for 1D VBL, the optimal decoding boundary lies at the tails of the distributions.

In this chapter, we investigate the lower-bounds on energy-per-bit when using high-dimensional VBL (HD-VBL) representations. Examples of 2D and 3D MBL and VBL representations are shown in Fig. 7.2. In the case of high-dimensional MBL (HD-MBL), the lower bound on

E_b/N_0 can be derived using a channel coding theorem. For instance, for an additive white gaussian noise (AWGN) channel, the lower-bound on E_b/N_0 is -1.59dB [89]. Thus, all existing communication schemes that employ MBL representations are limited by this bound even when the signal-dimensions used for encoding approaches infinity. In the case of HD-VBL, the fundamental limit on E_b/N_0 is determined by the overlapping volume of multivariate probability distributions, as illustrated in Fig. 7.2 for 2D, 3D representations, which determines the trade-off between the information capacity and the BER. Using geometric arguments, we show that for HD-VBL, the information capacity and BER become uncorrelated with respect to each other. Hence, both BER and E_b/N_0 could concurrently be pushed towards zero. Note that zero E_b/N_0 communication schemes have been previously proposed in the literature in the context of thermodynamic computing [90] and adiabatic computing [91]; however, the limit is achievable only for asymptotically zero information (data) rates.

7.2 Geometric Interpretation of HD-VBL

For our analysis, we will use the standard communication model, as shown in Fig. 7.1(a) and follow the arguments on high-dimensional geometry as depicted in [92]. In the case of HD-VBL, each codeword is encoded by modulating the variance of a zero-mean high-dimensional signal along the direction $\mathbf{X} \in \mathbb{R}^D$ in a D -dimensional space as indicated in Fig. 7.3. For an additive-white-Gaussian-noise (AWGN) channel, the received codeword (Y) takes a shape of multi-dimensional Gaussian PDF and its contour is geometrically represented using a D -dimensional hyper-ellipsoid as shown in Fig. 7.3. When the channel is not being used, the PDF of Y at the receiver is symmetrical around the origin and can be illustrated using a D -dimensional hyper-sphere \mathbf{S}_0 and is determined by the noise spectral density (N_0).

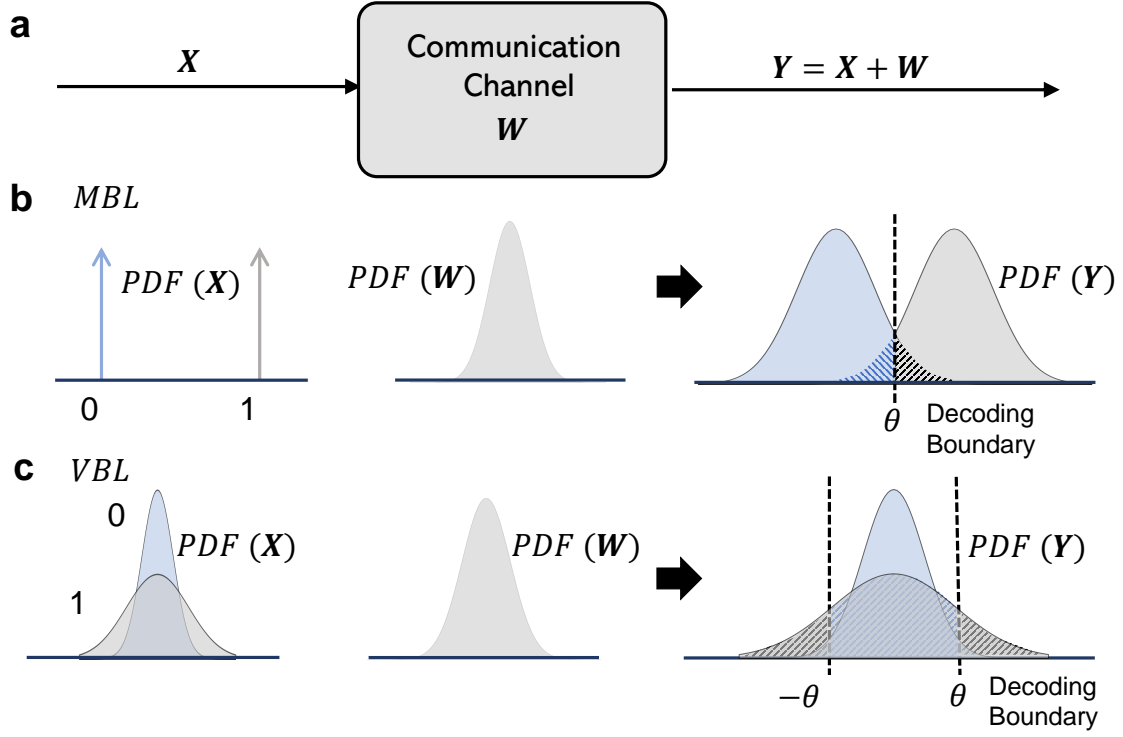


Figure 7.1: Comparison of mean-based logic (MBL) and variance-based logic (VBL) representations using (a) a standard communication system model and an AWGN channel. (b) For one-dimensional MBL, the source PDF is encoded using two Dirac-delta functions located at two logic states (\mathbf{X}) 0 and 1. The receiver differentiates the two MBL levels using a decoding boundary θ that separates the PDF corresponding to the output of the AWGN channel (\mathbf{Y}). (c) For one-dimensional VBL the input logic levels are mapped into PDFs with low(0) and high(1) variances. The receiver then differentiates between the VBL levels using a decoding boundary ($\pm\theta$) that are located at the tails of the output PDFs.

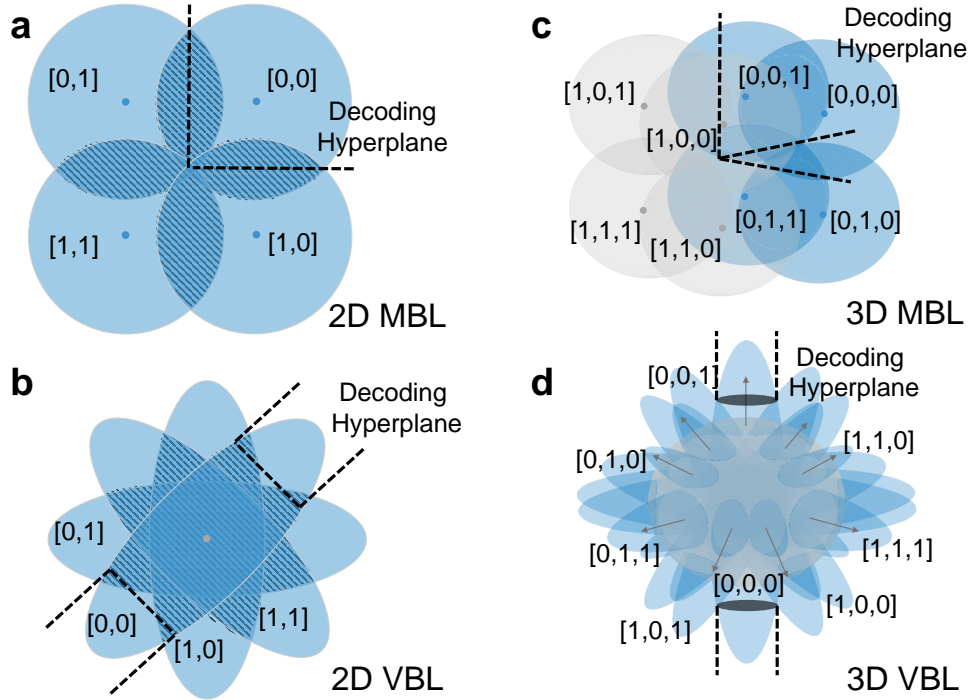


Figure 7.2: (a) Generalization of MBL and VBL to two and three dimensions. For high-dimensional MBL (HD-MBL) the decoding hyperplane cuts through the volume of the overlapping probability density functions (PDFs), whereas for HD-VBL, the decoding boundaries lie on the surface of the overlapping high-dimensional PDFs. Note that the overlap between the PDFs determines the bit-error-rate (BER) for each representation.

When the target D -tuple VBL codeword is transmitted, the received PDF at the receiver is a hyper-ellipsoid \mathbf{S}_1 (as illustrated in Fig. 7.3), whose major axis is oriented along the vector \mathbf{X} .

To detect whether the target code-word was transmitted, the receiver uses a decoder with decision boundaries that coincide with two hyper-cylinders \mathbf{T}_1 and \mathbf{T}_2 , as illustrated in Fig. 7.3. Both \mathbf{T}_1 and \mathbf{T}_2 are aligned along the direction of \mathbf{X} (known a-priori) and terminated by spherical caps \mathbf{C}_1 and \mathbf{C}_2 , formed by the overlap between hyper-ellipsoid \mathbf{S}_1 and the hyper-sphere \mathbf{S}_0 . The received codedword is decoded correctly only if the received signal vector lies within the boundary of the hyper-cylinders, shown in Fig. 7.3. Based on this decoder we can analytically estimate the probability-of-detection p_d for each of transmitted codewords. Mathematically, we show in section 7.3, estimating p_d reduces to solving a two-fold hypothesis testing formulation involving χ^2 distributions. Then, for a given probability-of-detection p_d , we estimate the number of non-overlapping spherical caps \mathbf{C}_1 and \mathbf{C}_2 that could be packed on the surface of the hyper-sphere \mathbf{S}_0 , which gives us an estimate on the capacity of this specific HD-VBL representation.

7.3 Numerical Results

7.3.1 HD-VBL with one degree-of-freedom

For an HD-VBL with one degree-of-freedom the signal power is added to any one of the available D -dimensions, so that the direction vector \mathbf{X} falls along one of the axes as illustrated in Fig. 7.3. Without loss of generality, multi-dimensional variance of the received vector \mathbf{Y}

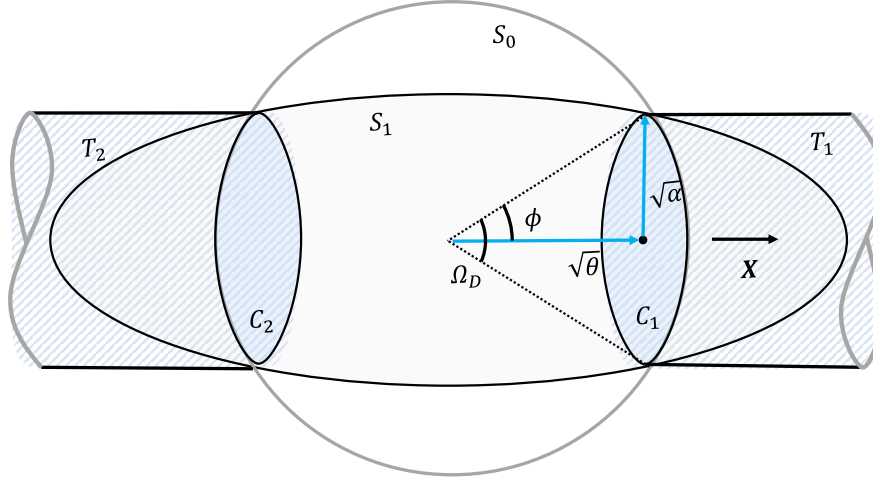


Figure 7.3: Estimation of capacity and BER for VBL representation with a threshold-based decoder. Decision rule for estimating the probability of correct detection (p_d) is provided by the bounding cylinders (\mathbf{T}_1 , \mathbf{T}_2).

could be represented using a diagonal co-variance matrix (Σ_D) given by,

$$\Sigma_D = \text{diag} [P + N_0, N_0, N_0, \dots, N_0] \quad (7.1)$$

where P is the total signal power and N_0 is the channel noise power per dimension. Thus, PDF for the received vector $\mathbf{Y} = [y_1, y_2, \dots, y_D]$ is given by a multi-variate zero-mean normal distribution which is,

$$f_Y(y_1, y_2, \dots, y_D) = A \exp \left(-\frac{1}{2} \left[\frac{y_1^2}{P + N_0} + \sum_{i=2}^D \frac{y_i^2}{N_0} \right] \right), \quad (7.2)$$

where A is the normalization factor [93]. Note that this distribution can be parameterized using $[a, b] = \left[y_1, \sqrt{\left(\sum_{i=2}^D \frac{y_i^2}{D-1} \right)} \right]$, where each of the parameters a^2 and b^2 assumes a χ^2 distribution with degrees-of-freedom 1 and $D - 1$ respectively and PDFs are illustrated in Fig. 7.4(a). The decision rule (or decoder) is then determined by the solid angle Ω_D and

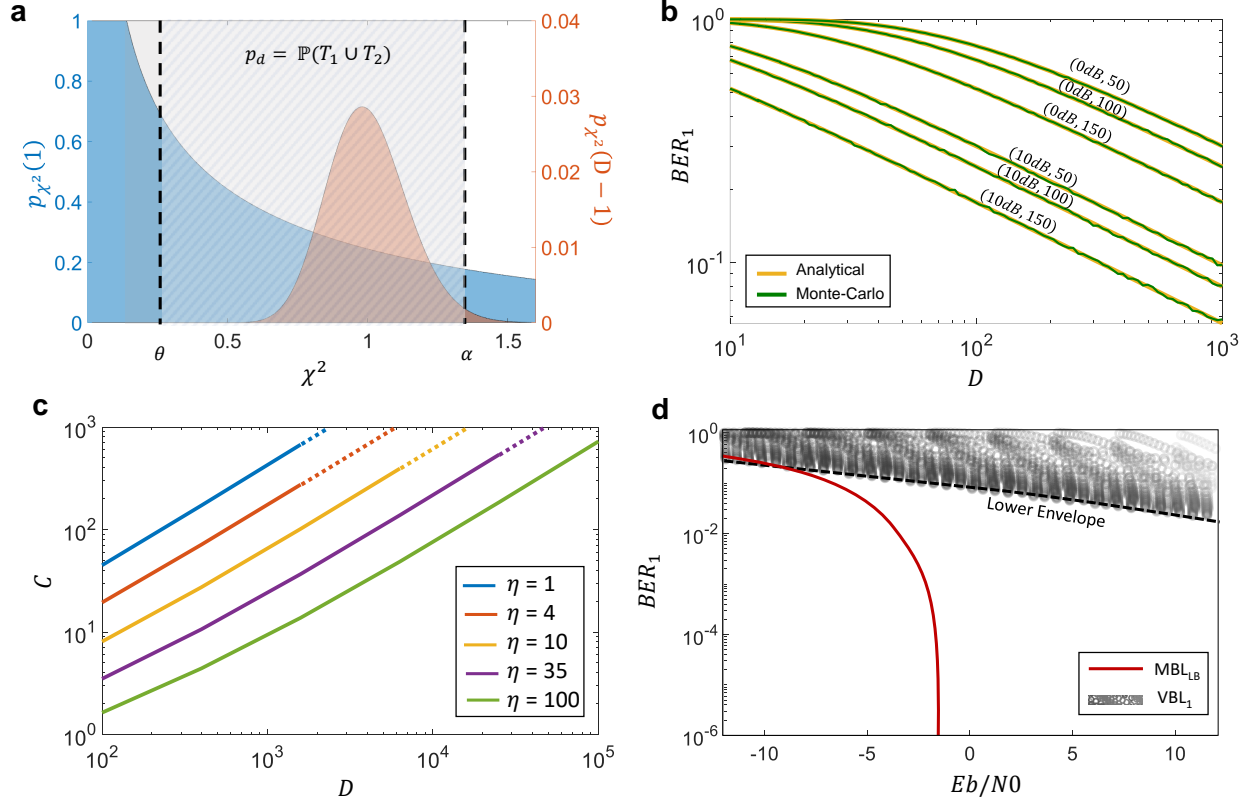


Figure 7.4: (a) BER estimation in terms of a two-fold hypothesis testing based on a Chi-square distribution with degree of freedom 1. (b) Verification of analytical expression derived in equation. 7.3 for $BER_1 (= 1 - p_d)$ with Monte-Carlo simulations for a different number of dimensions (D) and parameters (SNR, θ). (c) Estimated channel capacity as a function of D in log scale. (d) Classic BER_1 - E_b/N_0 plot for the case of VBL with one degree-of-freedom, and comparison is made with respect to MBL_{LB} .

projected angle ϕ shown in the $a - b$ Cartesian plane contained by the thresholds α and θ , as shown in Fig. 7.3. The probability of detecting the correct codeword (p_d) is given by the total probability mass concentrated between the two thresholds, also highlighted in Fig. 7.3 and is given by

$$\begin{aligned}
p_d &= 1 - BER_1 = \mathbb{P}(\mathbf{Y} \in (\mathbf{T}_1 \cup \mathbf{T}_2)) \\
&= \mathbb{P}[(a^2 \geq \theta) \wedge (b^2 \leq \alpha)] \\
&= \frac{\gamma(\frac{D-1}{2}, \frac{(D-1)\eta\theta'}{2})}{\Gamma(\frac{D-1}{2})} \left(1 - \frac{\gamma(\frac{1}{2}, \frac{\theta'}{2(D \text{ SNR} + 1)})}{\Gamma(\frac{1}{2})} \right)
\end{aligned} \tag{7.3}$$

Here, $\theta' = \frac{\theta}{N_0}$ is the normalized threshold, $\eta = \frac{\alpha}{\theta} = (\tan \phi)^2$ and $SNR = \frac{P}{DN_0}$ is the signal to noise power ratio. Also, $\gamma(., .)$ is the lower incomplete gamma function and $\Gamma(.)$ is the ordinary gamma function [94]. Fig. 7.4(b) shows the corresponding bit-error-rate BER_1 , where the subscript 1 indicates the number of degrees-of-freedom. BER_1 asymptotically decreases with the increase in the number of dimensions D , for different levels of signal-to-noise ratio (SNR) and decoder parameters. Also, the analytical model for p_d has been validated using Monte-Carlo simulations for multiple parameter realizations and is shown in Fig. 7.4(b).

To calculate the capacity of HD-VBL, we estimate the number of non-overlapping spherical caps that can be packed on the surface of a D -dimensional hyper-sphere determined by the thresholds, as illustrated in Fig. 7.3. Estimation of optimal packing density for spherical-caps has been well studied in literature wrapped spherical codes and laminated spherical codes [95, 96]. The number of code words (M_1) that can be accommodated in the space is given by the ratio between the total surface area (A_D), and the area spanned by one single

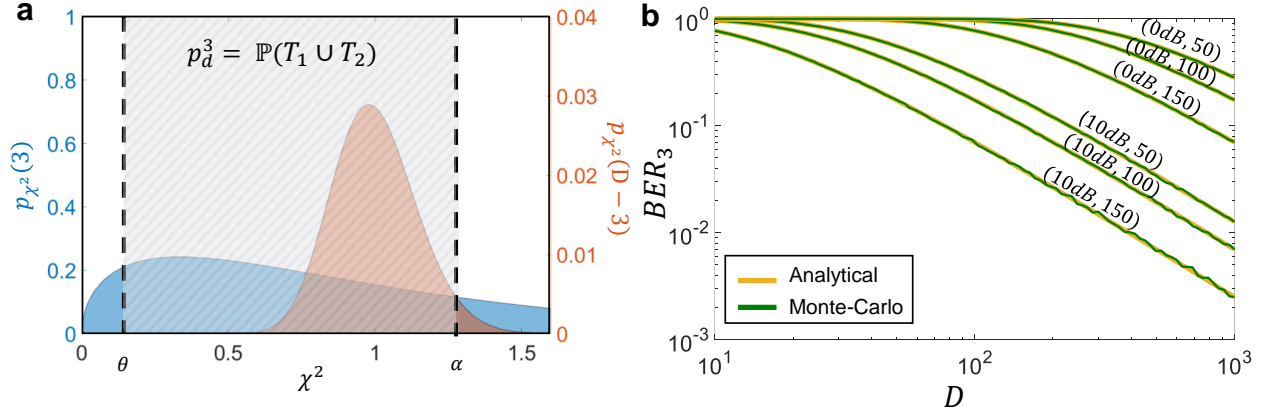


Figure 7.5: Extension to the case of general HD-VBL with variable degrees-of-freedom (a) Estimation of the p_d^k using two-fold hypothesis testing for a 100-dimensional VBL representation with degrees-of-freedom $k=3$. (b) Verification of analytical BER expressions derived in equation. 7.3, 7.9 with Monte-Carlo simulations for different parameter values (SNR , θ).

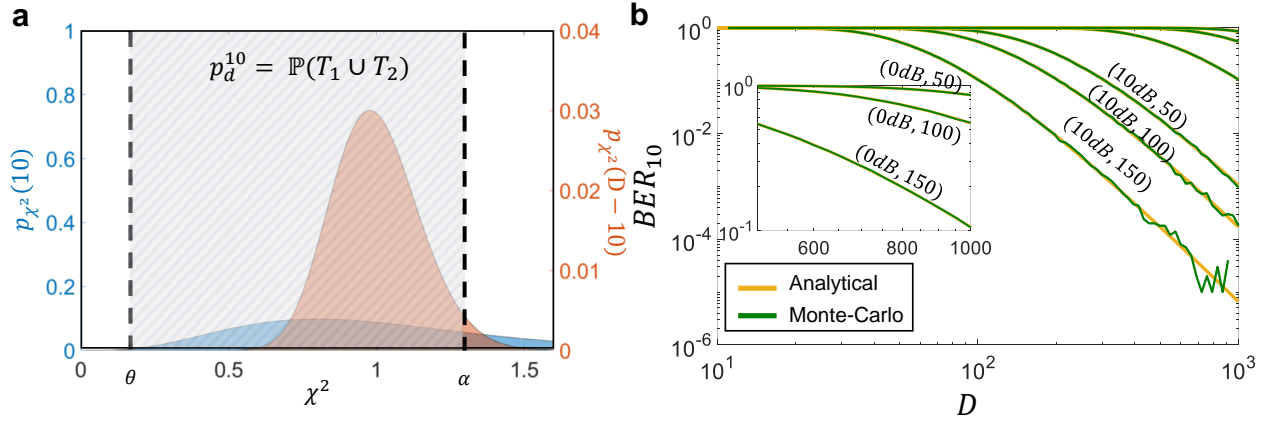


Figure 7.6: Extension to the case of general HD-VBL with variable degrees-of-freedom (a) Estimation of the p_d^k using two-fold hypothesis testing for a 100-dimensional VBL representation with degrees-of-freedom $k=10$. (b) Verification of analytical BER expressions derived in equation. 7.3, 7.9 with Monte-Carlo simulations for different parameter values (SNR , θ).

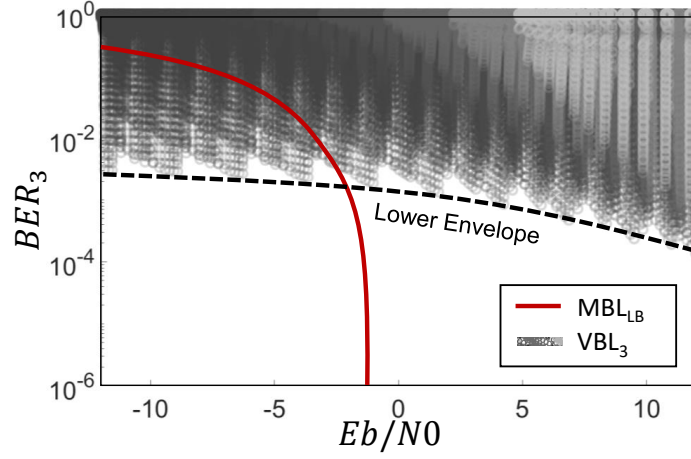


Figure 7.7: Energy-per-bit (E_b/N_0) estimated as defined in equation. 7.8 vs BER plots for the case of HD-VBL with degrees-of-freedom $k=3$ and interpolated lower bounds (VBL Bound).

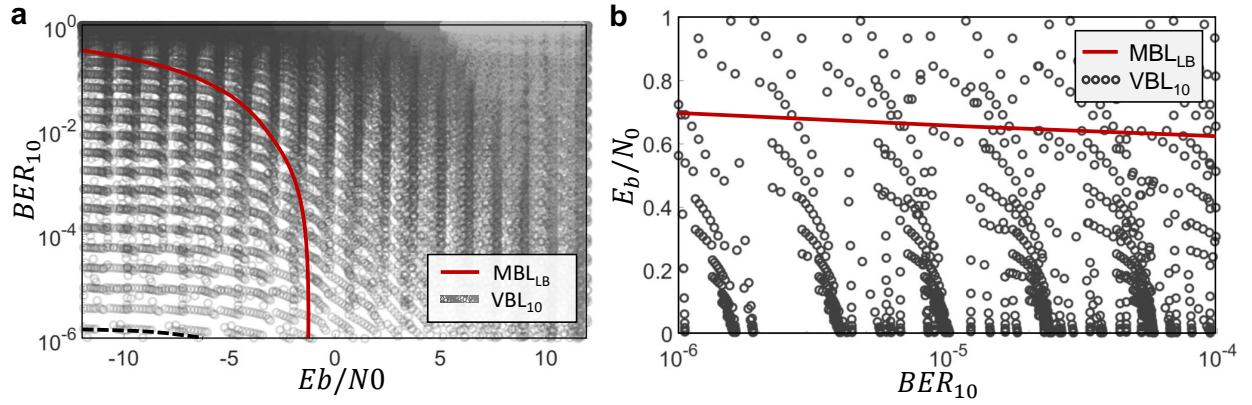


Figure 7.8: Energy-per-bit (E_b/N_0) estimated as defined in equation. 7.8 vs BER plots for the case of HD-VBL with degrees-of-freedom $k=10$ and interpolated lower bounds (VBL Bound).

codeword (A_D^{Cap}) which are given by,

$$A_D^{Cap} = \frac{1}{2} A_D I_{\sin^2 \phi} \left(\frac{D-1}{2}, \frac{1}{2} \right) \quad (7.4)$$

where ϕ is the angle intended by the thresholds (θ, α) and $I_*(.,.)$ is the regularized incomplete beta function. Also, $\sin^2 \phi$ could be expressed as $\sin^2(\tan^{-1} \sqrt{\eta})$ where $\eta = \frac{\alpha}{\theta}$ and thus,

$$A_D^{Cap} = \frac{1}{2} A_D I_{\sin^2(\tan^{-1} \sqrt{\eta})} \left(\frac{D-1}{2}, \frac{1}{2} \right) \quad (7.5)$$

So the number of code words is given by,

$$\begin{aligned} M_1 &= \frac{A_D}{A_D^{Cap}} \\ &= \frac{1}{I_{\sin^2(\tan^{-1} \sqrt{\eta})} \left(\frac{D-1}{2}, \frac{1}{2} \right)} \end{aligned} \quad (7.6)$$

Using the expression in equation 7.6, the capacity for this specific representation is given by,

$$C = \log_2 M_1 = \log_2 \left(\frac{1}{I_{\sin^2(\tan^{-1} \sqrt{\eta})} \left(\frac{D-1}{2}, \frac{1}{2} \right)} \right). \quad (7.7)$$

estimated using logarithmic measure [92]. Fig. 7.4(c) plots the capacity C with respect to the signal dimensions D , for different choices of the decoder hyper-parameters (θ, α, η) . The estimated capacity in equation 7.7 can be used to obtain the energy-per-bit $(\frac{E_b}{N_0})$ for different values of signal power P that is,

$$\frac{E_b}{N_0} = \frac{SNR}{C} = \frac{P}{DN_0 C} \quad (7.8)$$

The results in Fig. 7.4(b)-(c) were used to obtain the BER_1-E_b/N_0 plot as shown in Fig 7.4(d). Note that every marker in the HD-VBL simulation in Fig 7.4(d) corresponds to a specific choice of a decoder parameter set (θ, α) . The result shows that for this HD-VBL representation, the BER can be reduced, but at levels of energy-per-bit (E_b/N_0) that are significantly higher than the MBL_{LB} .

7.3.2 HD-VBL with k degrees-of-freedom

We generalize the VBL representation to a topology where the variance is now encoded along a specific sub-manifold of dimension $k(< D)$, instead of a one axis as discussed in the section above. The code-words are now represented by sub-manifolds that are spanned by a vectors $X = [x_1, x_2, \dots, x_D]$, such that $\sum_{i=1}^D x_i = k$ with $v_i \in \{0, 1\} \forall i = [1, D]$. Similar to the analysis presented in section 7.3.1, the estimation of the modified parameters $[a_k, b_k] = \left[\sqrt{\left(\sum_{i=1}^k \frac{y_i^2}{k} \right)}, \sqrt{\left(\sum_{i=k+1}^D \frac{y_i^2}{D-k} \right)} \right]$, which admits the PDFs $a_k^2 \sim \chi_k^2$ and $b_k^2 \sim \chi_{D-k}^2$. The respective distributions corresponding to $D = 100$ with degrees-of-freedom $k = 3$ and $k = 10$ are shown in Fig. 7.5-7.6, where the respective probability-of-detection p_d^3 and p_d^{10} are given by the total probability mass within the two thresholds θ and α with signal power spread equally (SNR/k) across only k axes in the direction of X .

Following similar arguments as in section 7.3.1, the probability of correctly decoding p_d^k can be estimated as,

$$\begin{aligned} p_d^k &= 1 - BER_k = \mathbb{P}(\mathbf{Y} \in (\mathbf{T}'_1 \cup \mathbf{T}'_2)) \\ &= \frac{\gamma\left(\frac{D-k}{2}, \frac{(D-k)\eta\theta'}{2}\right)}{\Gamma\left(\frac{D-k}{2}\right)} \left(1 - \frac{\gamma\left(\frac{k}{2}, \frac{k\theta'}{2(D\frac{SNR}{k}+1)}\right)}{\Gamma\left(\frac{k}{2}\right)} \right) \end{aligned} \quad (7.9)$$

It can be seen in Fig. 7.5(b), as k increases the region signifying p_d^k spans a large proportion of the probability mass as depicted in the BER_k plots shown in Fig. 7.5-7.6. Note that sub-script k denotes the number of degrees-of-freedom considered in the definition of HD-VBL representation. The analytical results are given by equation. 7.9 have also been verified using Monte-Carlo simulations, as shown in Fig. 7.5-7.6. Capacity of a HD-VBL representation with k -degrees of freedom is estimated using spherical-cap packing argument for a $(D - k)$ -dimensional sphere and the number of code words are estimated using similar arguments as in equation. 7.6,

$$M_k = \frac{1}{I_{\sin^2 \phi} \left(\frac{D-k}{2}, \frac{k}{2} \right)} \quad (7.10)$$

and hence the capacity is given by,

$$C = \log_2 M_k = \log_2 \left(\frac{1}{I_{\sin^2(\tan^{-1} \sqrt{\eta})} \left(\frac{D-k}{2}, \frac{k}{2} \right)} \right) \quad (7.11)$$

The average bit-error rate (BER_k) and capacity (C) were computed for different thresholds (θ, α) and the energy-per-bit (E_b/N_0) was estimated using equation. 7.8. Fig. 7.7-7.8. show the $BER_k - E_b/N_0$ plots corresponding to the case $k = 3$ and $k = 10$. Also, each point in the BER simulation corresponds to the results obtained for a specific choice of the decoder parameter θ, α . The results clearly show that there exist HD-VBL representations for dimensions no more significant than 100 that achieves near-zero BER with E_b/N_0 close to zero values. However, whether there exist VBL representations that can asymptotically achieve arbitrarily small BER at arbitrarily small E_b/N_0 still needs to be verified through Monte-Carlo studies. This would require an exhaustive search over different decoding parameters and decoder topologies which in turn requires significant computational resources.

7.4 Summary

The analysis and results presented in this chapter seem to indicate that by encoding information in the variance of the signal, we can significantly improve upon the $BER - E_b/N_0$ MBL limit. The intuitive understanding of this effect is that VBL encodes information on the surface of a hyper-sphere whose volume asymptotically goes to zeros as the number of dimensions approaches infinity. As a result, for VBL the tails of the distributions project orthogonally to the hyper-spherical surface whereas the packing of the centroids is achieved on the surface of the hypersphere. In a high-dimensional space and for low SNR, these two effects (packing and error rates) are not perfectly correlated and hence once could be reduced without reducing the other. This implies that the VBL limit could potentially achieve arbitrary small BER at near-zero E_b/N_0 . However, this conjecture needs to be mathematically proven and will be the topic of future publications. For a conventional MBL representation, the lower-limit arises because the overlap between the PDFs of the adjacent codewords (centroids) lies within the volume spanned by their PDFs. In higher dimensions and for a given signal-to-noise ratio, the packing density (or equivalently the channel capacity) scale linearly with the number of dimensions. As a result, the energy-per-bit E_b/N_0 , cannot be further reduced while achieving near-zero BER, thus leading to the MBL-limit [92].

One of the challenges in implementing a practical communication system is the complexity of implementing the decoder at the receiver. For an optimal decoder, the correct set of hyper-parameters needs to be chosen. However, for higher-dimensional VBL and when multiple directions are chosen for encoding, one has to resort to an exhaustive search over the decoder parameter space to achieve the optimal decoding performance. Practical consideration and the complexity of the optimization procedure would impose limits on the correct choice of these parameters; however, note that for stationary channels, the parameters need to be

estimated only once. Adaptive determination of the decoding hyper-parameters will be a topic of future research. Also, note that even though we have shown the asymptotic property of near-zero BER at near-zero E_b/N_0 for a specific type of VBL representation, there might exist other VBL representations that might demonstrate superior convergence. In this spirit, there might exist some connection between VBL representations and stochastic resonance based decoding, where “noise” or variance is introduced into the system to improve the detection of a buried but harmonic signal [97]. Additionally, the practical realization of the VBL based communication system would be a topic for future research. In VBL [98], it was shown that the energy-harvesting systems [55] and emerging valleytronic devices [75] could form a natural platform to implement some of the proposed communication techniques.

Chapter 8

Conclusion

This dissertation demonstrates that a commercial off the shelf (COTS) ultrasound reader can perform multi-access telemetry with devices implanted inside the body. Compared to an RF-based telemetry system, ultrasound-based telemetry can penetrate deeper into biological tissue. A millimeter-scale piezoelectric crystal can establish a high-speed data communication link. Specifically, this telemetry technique generates M-scan/B-scan images containing the transmitted information, and it is stored as a bit-map image and later can be demodulated using appropriate image processing algorithms. Experimental results demonstrate data rates close to 1 Mbps at implantation depths greater than 10 cm with reasonable BER, which suits most in-vivo sensing applications. The measured power dissipation on sonomicrometry devices was shown to be well below the tissue heating limits. This proposed technique's main advantage is that COTS and medically compliant ultrasound readers for performing in-vivo telemetry will obviate the need to design dedicated ultrasound decoders and help translate the technology into clinical practice without additional regulations. Flexibility in providing variable data rates makes this technique accessible for immediate adoption in several applications ranging from neural implants, cardiac implants, and health monitoring sensors for hip or knee-implants. Using a B-scan imaging probe, I also showed the feasibility of

sub-nano-watt in-vivo telemetry links in a water-medium for implantation depths greater than 10cm. We also presented a simple and yet robust decoding algorithm, and we characterized the B-scan telemetry performance using reader sensitivity and bit-error rates. Although the data rates achieved using the proposed scheme are limited by the frame rate of the imager, given modern ultrasound systems that enable imaging at 10000 fps the data rates using B-scan telemetry scale accordingly without affecting the quality (BER) of the communication link.

Models for estimating energy levels harvested from non-linear biomechanical perturbations of a cardiac valvular apparatus are presented in chapter. 3. My analysis demonstrates the feasibility of harvesting 0.1-10 mW/cm², which is orders of magnitude higher than the previous configurations that harvested energy from the surface of the heart or the aorta. For instance, the time-average power density was reported to be 1.2μW/cm² when harvesting energy from the surface of the heart. In contrast, the power density was 170nW/cm³ when the energy was harvested from the aorta.

I also present an alternate and novel approach for building logic gates that operate on the input signal's statistical variance, which we call variance-based logic. The approach could combine the functionalities of energy harvesting and digital computation, and the approach could be applied to a wide variety of energy transducers. With the help of a prototype, we have demonstrated fundamental digital cells' performance and proposed a simple state machine's feasibility. Benefits of using variance-based logic include its reciprocity of the energy transducer (like an RF antenna) which can be used to transmit logic-state information wirelessly. Variance-based logic shares similarity with load-modulation techniques commonly used in backscattering based communication systems.

”Is there any advantage in encoding the information in signal mean rather than in signal variance?”. This question has led my research to investigate variance-based informatics. Although preliminary results demonstrate the benefits of variance-based representation and threshold-based detection schemes, underlying theory, practical realization, and generalization to high dimensional spaces are still part of future research.

8.1 Thesis Contributions

The main contributions of this thesis are as follows:

- **Ultrasound Imaging-based Telemetry:** First to investigate the use of commercial off the shelf ultrasound readers for the performing multi-access and in-vivo biotelemetry.
- **Piezoelectric Suture:** First to investigate the concept of piezoelectric suture for efficient energy harvesting from cardiac valve dynamics and its validation using in-vivo sonomicrometry data.
- **Variance driven Computing:** First to investigate variance-based computing architecture to realize digital state machines that operate using multiple unregulated power sources.
- **Variance based Informatics:** First to explore variance-based representation in the context of energy-efficient physical system design.

8.2 Future Directions

Although this dissertation contains a brief selection of topics under the title "Theory, Design, and Implementation of Energy Efficient Bio-telemetry using Ultrasound Imaging," in this section, I summarize the immediate next steps that follow the research and also implications of discussed methods beyond biomedical applications.

- **Self-powered in-vivo Sonomicrometry:** One of the challenging application that can be addressed using imaging based telemetry is to practically demonstrate a fully self-powered in-vivo sonomicrometry platform. Future work in this direction includes assembling a sub cm^3 scale self-powered implantable device by integrating the sonomicrometry crystal (Chapter 2) along with the oscillator IC (Chapter 5) in bio-compatible packaging with piezoelectric leads (chapter 4). Interrogation of these implantable devices can be carried using a commercial off the shelf ultrasound imager (chapter 2). This platform technology can enable a tether-free sonomicrometry platform that can be used to monitor the cardiac valve monitoring in the ovine model and several other deep tissue interrogation studies.
- **Energy Harvesting Internet-of-Things:** Traditionally, self-powered internet of things are designed using modular approach and each module is designed and optimized independently. The design techniques introduced in Chapter 5 provide architecture for designing digital circuits that rely on signal variance and seamlessly integrates energy harvesting circuits with digital logic. In this way, these devices can overcome temporal latency in accumulating and trickle charging energy from energy sources. Although the results presented in this work only serve as an introduction to this concept, the future work will focus on improving circuit level implementation of the basic logic gates such

as latency and power dissipation. We envision that digital circuits designed using the proposed approach could be applied in designing novel IoT sensors that can monitor without any down-time, free-of-maintenance and can be interfaced with existing and future IoT networks [99–103].

- **Variance-based Informatics:** The work on high dimensional variance-based logic indicates that by encoding information in the variance of the signal, we can significantly improve upon the BER-EbN0 MBL limit. The intuitive understanding of this effect is that VBL encodes information on the surface of a hyper-sphere whose volume asymptotically goes to zero as the number of dimensions approaches infinity. As a result, for VBL, the tails of the distributions project orthogonal to the hyper-spherical surface, whereas the centroids' packing is achieved on the surface of the hypersphere. In a high-dimensional space and low SNR, these two effects (packing and error rates) are not perfectly correlated. Hence, one could be reduced without reducing the other, which implies that the VBL limit could achieve arbitrary small BER at near-zero EbN0. However, this conjecture needs to be mathematically proven and will be the topic of future research.

Bibliography

- [1] H. R. Sharif and Y. S. Kavian, *Technological Breakthroughs in Modern Wireless Sensor Applications*. IGI Global, 2015.
- [2] K. Sivasubramanian and M. Pramanik, “High frame rate photoacoustic imaging at 7000 frames per second using clinical ultrasound system,” *Biomedical optics express*, vol. 7, no. 2, pp. 312–323, 2016.
- [3] P. Gueth, R. Blanchard, H. Liebgott, and O. Basset, “Improved resolution for ultrasound fourier imaging,” in *2010 IEEE International Ultrasonics Symposium*. IEEE, 2010, pp. 1735–1738.
- [4] F. S. Foster, C. J. Pavlin, K. A. Harasiewicz, D. A. Christopher, and D. H. Turnbull, “Advances in ultrasound biomicroscopy,” *Ultrasound in medicine & biology*, vol. 26, no. 1, pp. 1–27, 2000.
- [5] G. Clement, J. Huttunen, and K. Hynynen, “Superresolution ultrasound imaging using back-projected reconstruction,” *The Journal of the Acoustical Society of America*, vol. 118, no. 6, pp. 3953–3960, 2005.
- [6] S. Tognarelli, C. Quaglia, P. Valdastrì, E. Susilo, A. Menciasci, and P. Dario, “Innovative stopping mechanism for esophageal wireless capsular endoscopy,” *Procedia Chemistry*, vol. 1, no. 1, pp. 485–488, 2009.
- [7] S. Thongpang, T. J. Richner, S. K. Brodnick, A. Schendel, J. Kim, J. A. Wilson, J. Hippensteel, L. Krugner-Higby, D. Moran, A. S. Ahmed *et al.*, “A micro-electrocorticography platform and deployment strategies for chronic bei applications,” *Clinical EEG and neuroscience*, vol. 42, no. 4, pp. 259–265, 2011.
- [8] A. Ahuja, J. Dorn, A. Caspi, M. McMahon, G. Dagnelie, P. Stanga, M. Humayun, R. Greenberg, A. I. S. Group *et al.*, “Blind subjects implanted with the argus ii retinal prosthesis are able to improve performance in a spatial-motor task,” *British Journal of Ophthalmology*, vol. 95, no. 4, pp. 539–543, 2011.
- [9] A. Wang, S. Banerjee, B. A. Barth, Y. M. Bhat, S. Chauhan, K. T. Gottlieb, V. Konda, J. T. Maple, F. Murad, P. R. Pfau *et al.*, “Wireless capsule endoscopy,” *Gastrointestinal endoscopy*, vol. 78, no. 6, pp. 805–815, 2013.

- [10] R. Muller, H.-P. Le, W. Li, P. Ledochowitsch, S. Gambini, T. Bjorninen, A. Koralek, J. M. Carmena, M. M. Maharbiz, E. Alon *et al.*, “A minimally invasive 64-channel wireless μ ecog implant,” *IEEE Journal of Solid-State Circuits*, vol. 50, no. 1, pp. 344–359, 2014.
- [11] G. Charvet, M. Foerster, S. Filipe, J. Porcherot, J. Bêche, R. Guillemaud, P. Audebert, G. Régis, B. Zongo, S. Robinet *et al.*, “Wimagine: A wireless, low power, 64-channel ecog recording platform for implantable bci applications,” in *Neural Engineering (NER), 2011 5th International IEEE/EMBS Conference on*. IEEE, 2011, pp. 356–359.
- [12] M. Anis, G. Grau, and N. Wehn, “Ultra low power rf transceiver architecture for in-body communication system,” in *2010 IEEE Radio and Wireless Symposium (RWS)*. IEEE, 2010, pp. 575–578.
- [13] M. A. Hanson, “Health effects of exposure to ultrasound and infrasound: report of the independent advisory group on non-ionising radiation,” *Health Protection Agency*, 2010.
- [14] G. E. Santagati and T. Melodia, “Sonar inside your body: Prototyping ultrasonic intra-body sensor networks,” in *IEEE INFOCOM 2014-IEEE Conference on Computer Communications*. IEEE, 2014, pp. 2679–2687.
- [15] E. Demirors, G. Alba, G. E. Santagati, and T. Melodia, “High data rate ultrasonic communications for wireless intra-body networks,” in *2016 IEEE International Symposium on Local and Metropolitan Area Networks (LANMAN)*. IEEE, 2016, pp. 1–6.
- [16] D. Seo, R. M. Neely, K. Shen, U. Singhal, E. Alon, J. M. Rabaey, J. M. Carmena, and M. M. Maharbiz, “Wireless recording in the peripheral nervous system with ultrasonic neural dust,” *Neuron*, vol. 91, no. 3, pp. 529–539, 2016.
- [17] K. S. Shanmugam, “Digital and analog communication systems,” *STIA*, vol. 80, p. 23225, 1979.
- [18] Y. Alazzawi and S. Chakrabartty, “Design of cmos telemetry circuits for in-vivo wireless sonomicrometry,” in *2016 IEEE International Symposium on Circuits and Systems (ISCAS)*. IEEE, 2016.
- [19] D. Miller, “Safety assurance in obstetrical ultrasound, sem,” *Ultrasound CT MRI 29 (2008) 156–164. Ultrasound in Obstetrics and Gynecology.*, 2008.
- [20] T. L. Szabo, *Diagnostic ultrasound imaging: inside out*. Academic Press, 2004.
- [21] L. Galluccio, T. Melodia, S. Palazzo, and G. E. Santagati, “Challenges and implications of using ultrasonic communications in intra-body area networks,” in *2012 9th Annual Conference on Wireless On-Demand Network Systems and Services (WONS)*. IEEE, 2012, pp. 182–189.

- [22] Kaye and Laby, “Table of physical and chemical constants.”
- [23] T. Yamada, T. Uezono, H. Sugawara, K. Okada, K. Masu, A. Oki, and Y. Horiike, “Battery-less wireless communication system through human body for in-vivo healthcare chip,” in *Silicon Monolithic Integrated Circuits in RF Systems, 2004. Digest of Papers. 2004 Topical Meeting on.* IEEE, 2004, pp. 322–325.
- [24] G. E. Santagati, T. Melodia, L. Galluccio, and S. Palazzo, “Medium access control and rate adaptation for ultrasonic intrabody sensor networks,” *IEEE/ACM Transactions on Networking*, vol. 23, no. 4, pp. 1121–1134, 2014.
- [25] L. W. Couch, M. Kulkarni, and U. S. Acharya, *Digital and analog communication systems.* Citeseer, 1997, vol. 6.
- [26] J. G. Proakis, M. Salehi, N. Zhou, and X. Li, *Communication systems engineering.* Prentice Hall New Jersey, 1994, vol. 2.
- [27] D. J. MacKay, “Good error-correcting codes based on very sparse matrices,” *IEEE transactions on Information Theory*, vol. 45, no. 2, pp. 399–431, 1999.
- [28] W. Borchani, K. Aono, N. Lajnef, and S. Chakrabartty, “Monitoring of postoperative bone healing using smart trauma-fixation device with integrated self-powered piezo-floating-gate sensors,” *IEEE Transactions on Biomedical Engineering*, vol. 63, no. 7, pp. 1463–1472, 2015.
- [29] C. H. W. Oey and S. Moh, “A survey on temperature-aware routing protocols in wireless body sensor networks,” *Sensors*, vol. 13, no. 8, pp. 9860–9877, 2013.
- [30] B. Fang, T. Feng, M. Zhang, and S. Chakrabartty, “Feasibility of b-mode diagnostic ultrasonic energy transfer and telemetry to a cm 2 sized deep-tissue implant,” in *Circuits and Systems (ISCAS), 2015 IEEE International Symposium on.* IEEE, 2015, pp. 782–785.
- [31] P. Dagum, T. A. Timek, G. R. Green, D. Lai, G. T. Daughters, D. H. Liang, M. Hayase, N. B. Ingels, and D. C. Miller, “Coordinate-free analysis of mitral valve dynamics in normal and ischemic hearts,” *Circulation*, vol. 102, no. suppl 3, pp. Iii–62, 2000.
- [32] J. J. Bax and V. Delgado, “Advanced imaging in valvular heart disease,” *Nature Reviews Cardiology*, vol. 14, no. 4, p. 209, 2017.
- [33] T. A. Timek, D. T. Lai, F. Tibayan, D. Liang, F. Rodriguez, G. T. Daughters, P. Dagum, N. B. Ingels, and C. Miller, “Annular versus subvalvular approaches to acute ischemic mitral regurgitation,” *Circulation*, vol. 106, no. 12 suppl 1, pp. I–27, 2002.

- [34] C. Dagdeviren, B. D. Yang, Y. Su, P. L. Tran, P. Joe, E. Anderson, J. Xia, V. Doraiswamy, B. Dehdashti, X. Feng *et al.*, “Conformal piezoelectric energy harvesting and storage from motions of the heart, lung, and diaphragm,” *Proceedings of the National Academy of Sciences*, vol. 111, no. 5, pp. 1927–1932, 2014.
- [35] B. Lu, Y. Chen, D. Ou, H. Chen, L. Diao, W. Zhang, J. Zheng, W. Ma, L. Sun, and X. Feng, “Ultra-flexible piezoelectric devices integrated with heart to harvest the biomechanical energy,” *Scientific reports*, vol. 5, 2015.
- [36] H. Zhang, X.-S. Zhang, X. Cheng, Y. Liu, M. Han, X. Xue, S. Wang, F. Yang, A. Smitha, H. Zhang *et al.*, “A flexible and implantable piezoelectric generator harvesting energy from the pulsation of ascending aorta: in vitro and in vivo studies,” *Nano Energy*, vol. 12, pp. 296–304, 2015.
- [37] A. Zurbuchen, A. Pfenniger, A. Stahel, C. T. Stoeck, S. Vandenberghe, V. M. Koch, and R. Vogel, “Energy harvesting from the beating heart by a mass imbalance oscillation generator,” *Annals of biomedical engineering*, vol. 41, no. 1, pp. 131–141, 2013.
- [38] Y. Qi, J. Kim, T. D. Nguyen, B. Lisko, P. K. Purohit, and M. C. McAlpine, “Enhanced piezoelectricity and stretchability in energy harvesting devices fabricated from buckled pzt ribbons,” *Nano letters*, vol. 11, no. 3, pp. 1331–1336, 2011.
- [39] L. Tang, Y. Yang, and C. K. Soh, “Broadband vibration energy harvesting techniques,” in *Advances in energy harvesting methods*. Springer, 2013, pp. 17–61.
- [40] N. Lajnef, W. Borchani, R. Burgueño, and S. Chakrabartty, “Self-powered piezo-floating-gate smart-gauges based on quasi-static mechanical energy concentrators and triggers,” vol. 15, no. 2. IEEE, 2015, pp. 676–683.
- [41] E. Lansac, K. H. Lim, Y. Shomura, W. A. Goetz, H. S. Lim, N. T. Rice, H. Saber, and C. M. Duran, “Dynamic balance of the aortomitral junction,” *The Journal of thoracic and cardiovascular surgery*, vol. 123, no. 5, pp. 911–918, 2002.
- [42] J. Hung, J. Solis, J. L. Guerrero, G. J. Braithwaite, O. K. Muratoglu, M. Chaput, L. Fernandez-Friera, M. D. Handschumacher, V. J. Wedeen, S. Houser *et al.*, “A novel approach for reducing ischemic mitral regurgitation by injection of a polymer to reverse remodel and reposition displaced papillary muscles,” *Circulation*, vol. 118, no. 14 suppl 1, pp. S263–S269, 2008.
- [43] N. B. Ingels, G. T. Daughters, E. B. Stinson, and E. L. Alderman, “Measurement of midwall myocardial dynamics in intact man by radiography of surgically implanted markers,” *Circulation*, vol. 52, no. 5, pp. 859–867, 1975.
- [44] N. B. Ingels, D. E. Hansen, G. T. Daughters, E. B. Stinson, E. L. Alderman, and D. C. Miller, “Relation between longitudinal, circumferential, and oblique shortening and

- torsional deformation in the left ventricle of the transplanted human heart.” *Circulation Research*, vol. 64, no. 5, pp. 915–927, 1989.
- [45] S. H. Kondapalli, Y. Alazzawi, M. Malinowski, T. Timek, and S. Chakrabartty, “Multiaccess in vivo biotelemetry using sonomicrometry and m-scan ultrasound imaging,” *IEEE Transactions on Biomedical Engineering*, vol. 65, no. 1, pp. 149–158, 2017.
 - [46] M. Malinowski, P. Wilton, A. Khaghani, D. Langholz, V. Hooker, L. Eberhart, R. L. Hooker, and T. A. Timek, “The effect of pulmonary hypertension on ovine tricuspid annular dynamics,” *European Journal of Cardio-Thoracic Surgery*, vol. 49, no. 1, pp. 40–45, 2015.
 - [47] S. Hargittai, “Savitzky-golay least-squares polynomial filters in ecg signal processing,” in *Computers in Cardiology, 2005*. IEEE, 2005, pp. 763–766.
 - [48] M. E. Hiro, J. Jouan, M. R. Pagel, E. Lansac, K. H. Lim, H.-S. Lim, and C. M. Duran, “Sonometric study of the normal tricuspid valve annulus in sheep,” *Journal of Heart Valve Disease*, vol. 13, no. 3, pp. 452–460, 2004.
 - [49] H. Fawzy, K. Fukamachi, C. D. Mazer, A. Harrington, D. Latter, D. Bonneau, and L. Errett, “Complete mapping of the tricuspid valve apparatus using three-dimensional sonomicrometry,” *The Journal of Thoracic and Cardiovascular Surgery*, vol. 141, no. 4, pp. 1037–1043, 2011.
 - [50] J. D’hooge, A. Heimdal, F. Jamal, T. Kukulski, B. Bijnens, F. Rademakers, L. Hatle, P. Suetens, and G. Sutherland, “Regional strain and strain rate measurements by cardiac ultrasound: principles, implementation and limitations,” *European Journal of Echocardiography*, vol. 1, no. 3, pp. 154–170, 2000.
 - [51] A. Jain, P. KJ, A. K. Sharma, A. Jain, and R. PN, “Dielectric and piezoelectric properties of pvdf/pzt composites: A review,” *Polymer Engineering & Science*, vol. 55, no. 7, pp. 1589–1616, 2015.
 - [52] S. H. Kondapalli, Y. Alazzawi, M. Malinowski, T. Timek, and S. Chakrabartty, “Feasibility of self-powering and energy harvesting using cardiac valvular perturbations,” *IEEE transactions on biomedical circuits and systems*, vol. 12, no. 6, pp. 1392–1400, 2018.
 - [53] K. K. Shung, *Diagnostic ultrasound: Imaging and blood flow measurements*. CRC press, 2015.
 - [54] J. Li and P. Stoica, *MIMO radar signal processing*. John Wiley & Sons, 2008.
 - [55] S. H. Kondapalli, X. Zhang, and S. Chakrabartty, “Variance-based digital logic for energy harvesting internet-of-things,” in *2017 IEEE International Symposium on Circuits and Systems (ISCAS)*. IEEE, 2017, pp. 1–4.

- [56] T. Bos, W. Jiang, J. D’hooge, M. Verhelst, and W. Dehaene, “Enabling ultrasound in-body communication: Fir channel models and qam experiments,” *IEEE transactions on biomedical circuits and systems*, vol. 13, no. 1, pp. 135–144, 2018.
- [57] B. Jaafar, J. Luo, D. Firfilionis, A. Soltan, J. Neasham, and P. Degenaar, “Ultrasound intra body multi node communication system for bioelectronic medicine,” *Sensors*, vol. 20, no. 1, p. 31, 2020.
- [58] M. L. Wang and A. Arbabian, “Exploiting spatial degrees of freedom for high data rate ultrasound communication with implantable devices,” *Applied Physics Letters*, vol. 111, no. 13, p. 133503, 2017.
- [59] T. C. Chang, M. L. Wang, J. Charthad, M. J. Weber, and A. Arbabian, “27.7 a 30.5 mm 3 fully packaged implantable device with duplex ultrasonic data and power links achieving 95kb/s with 10⁻⁴ ber at 8.5 cm depth,” in *2017 IEEE International Solid-State Circuits Conference (ISSCC)*. IEEE, 2017, pp. 460–461.
- [60] E. Demirors, G. Alba, G. E. Santagati, and T. Melodia, “High data rate ultrasonic communications for wireless intra-body networks,” in *2016 IEEE International Symposium on Local and Metropolitan Area Networks (LANMAN)*. IEEE, 2016, pp. 1–6.
- [61] G. E. Santagati and T. Melodia, “Sonar inside your body: Prototyping ultrasonic intra-body sensor networks,” in *IEEE INFOCOM 2014-IEEE Conference on Computer Communications*. IEEE, 2014, pp. 2679–2687.
- [62] A. Singer, M. Oelze, and A. Podkowa, “Mbps experimental acoustic through-tissue communications: Meat-comms,” in *2016 IEEE 17th International Workshop on Signal Processing Advances in Wireless Communications (SPAWC)*. IEEE, 2016, pp. 1–4.
- [63] I. H. Kalfas, “Principles of bone healing,” *Neurosurgical focus*, vol. 10, no. 4, pp. 1–4, 2001.
- [64] R. A. Deyo, A. Nachemson, and S. K. Mirza, “Spinal-fusion surgery—the case for restraint,” *The Spine Journal*, vol. 4, no. 5, pp. S138–S142, 2004.
- [65] H. Hasegawa, “Very high frame rate ultrasound for medical diagnostic imaging,” in *AIP Conference Proceedings*, vol. 2173, no. 1. AIP Publishing LLC, 2019, p. 020015.
- [66] Y. Zhang, F. Zhang, Y. Shakhsheer, J. D. Silver, A. Klinefelter, M. Nagaraju, J. Boley, J. Pandey, A. Shrivastava, E. J. Carlson *et al.*, “A batteryless 19uw mics/ism-band energy harvesting body sensor node soc for exg applications,” *IEEE Journal of Solid-State Circuits*, vol. 48, no. 1, pp. 199–213, 2012.
- [67] W. Zhao, K. Bhanushali, and P. Franzon, “Design of a rectifier-free uhf gen-2 compatible rfid tag using rf-only logic,” in *2016 IEEE International Conference on RFID (RFID)*. IEEE, 2016, pp. 1–6.

- [68] S. Briole, C. Pacha, K. Goser, A. Kaiser, R. Thewes, W. Weber, and R. Brederlow, "Ac-only rf id tags for barcode replacement," in *2004 IEEE International Solid-State Circuits Conference (IEEE Cat. No. 04CH37519)*. IEEE, 2004, pp. 438–537.
- [69] Y. Moon and D.-K. Jeong, "An efficient charge recovery logic circuit," *IEICE transactions on electronics*, vol. 79, no. 7, pp. 925–933, 1996.
- [70] A. G. Dickinson and J. S. Denker, "Adiabatic dynamic logic," *IEEE Journal of Solid-State Circuits*, vol. 30, no. 3, pp. 311–315, 1995.
- [71] B. Behin-Aein, D. Datta, S. Salahuddin, and S. Datta, "Proposal for an all-spin logic device with built-in memory," *Nature nanotechnology*, vol. 5, no. 4, pp. 266–270, 2010.
- [72] D. B. Strukov, G. S. Snider, D. R. Stewart, and R. S. Williams, "The missing memristor found," *nature*, vol. 453, no. 7191, p. 80, 2008.
- [73] M. Zwerg, A. Baumann, R. Kuhn, M. Arnold, R. Nerlich, M. Herzog, R. Ledwa, C. Sichert, V. Rzehak, P. Thanigai *et al.*, "An 82 μ a/mhz microcontroller with embedded feram for energy-harvesting applications," in *Solid-State Circuits Conference Digest of Technical Papers (ISSCC), 2011 IEEE International*. IEEE, 2011, pp. 334–336.
- [74] H. Wen and L. B. Kish, "Noise-based logic: Why noise? a comparative study of the necessity of randomness out of orthogonality," *Fluctuation and Noise Letters*, vol. 11, no. 04, p. 1250021, 2012.
- [75] C. E. Nebel, "Valleytronics: Electrons dance in diamond," *Nature materials*, vol. 12, no. 8, p. 690, 2013.
- [76] R. W. Keyes and R. Landauer, "Minimal energy dissipation in logic," *IBM Journal of Research and Development*, vol. 14, no. 2, pp. 152–157, 1970.
- [77] C. H. Bennett, "The thermodynamics of computation—a review," *International Journal of Theoretical Physics*, vol. 21, no. 12, pp. 905–940, 1982.
- [78] L. B. Kish and C. G. Granqvist, "Energy requirement of control: Comments on szilard's engine and maxwell's demon," *EPL (Europhysics Letters)*, vol. 98, no. 6, p. 68001, 2012.
- [79] L. B. Kish, "Thermal noise driven computing," *Applied Physics Letters*, vol. 89, no. 14, p. 144104, 2006.
- [80] B. E. Akgul, L. N. Chakrapani, P. Korkmaz, and K. V. Palem, "Probabilistic cmos technology: A survey and future directions," in *Very Large Scale Integration, 2006 IFIP International Conference on*. IEEE, 2006, pp. 1–6.

- [81] L. B. Kish and D. K. Ferry, “Information entropy and thermal entropy: apples and oranges,” *arXiv preprint arXiv:1706.01459*, 2017.
- [82] V. Guruswami and A. Rudra, “Error correction up to the information-theoretic limit,” *Communications of the ACM*, vol. 52, no. 3, pp. 87–95, 2009.
- [83] E. Cho, M. J. Cho, and J. Eltinge, “The variance of sample variance from a finite population,” *International Journal of Pure and Applied Mathematics*, vol. 21, no. 3, p. 389, 2005.
- [84] W. Zhao, K. Bhanushali, and P. Franzon, “Design of a rectifier-free uhf gen-2 compatible rfid tag using rf-only logic,” in *RFID (RFID), 2016 IEEE International Conference on*. IEEE, 2016, pp. 1–6.
- [85] S. Briole, C. Pacha, K. Goser, A. Kaiser, R. Thewes, W. Weber, and R. Brederlow, “Ac-only rf id tags for barcode replacement,” in *Solid-State Circuits Conference, 2004. Digest of Technical Papers. ISSCC. 2004 IEEE International*. IEEE, 2004, pp. 438–537.
- [86] C. E. Shannon, “A mathematical theory of communication,” *ACM SIGMOBILE Mobile Computing and Communications Review*, vol. 5, no. 1, pp. 3–55, 2001.
- [87] H. Dery, P. Dalal, L. Sham *et al.*, “Spin-based logic in semiconductors for reconfigurable large-scale circuits,” *Nature*, vol. 447, no. 7144, p. 573, 2007.
- [88] H. A. Fahmy and R. A. Kiehl, “Complete logic family using tunneling-phase-logic devices,” in *Microelectronics, 1999. ICM’99. The Eleventh International Conference on*. IEEE, 1999, pp. 153–156.
- [89] N. Benvenuto and G. Cherubini, *Algorithms for communications systems and their applications*. John Wiley & Sons, 2002.
- [90] R. Landauer, “Energy requirements in communication,” *Applied physics letters*, vol. 51, no. 24, pp. 2056–2058, 1987.
- [91] P. Teichmann, *Adiabatic logic: future trend and system level perspective*. Springer Science & Business Media, 2011, vol. 34.
- [92] C. E. Shannon, “Communication in the presence of noise,” *Proceedings of the IRE*, vol. 37, no. 1, pp. 10–21, 1949.
- [93] D. F. Morrison, L. C. Marshall, and H. L. Sahlin, “Multivariate statistical methods,” 1976.
- [94] S. Li, “Concise formulas for the area and volume of a hyperspherical cap,” *Asian Journal of Mathematics and Statistics*, vol. 4, no. 1, pp. 66–70, 2011.

- [95] J. Hamkins and K. Zeger, “Asymptotically dense spherical codes i wrapped spherical codes,” *IEEE Transactions on Information Theory*, vol. 43, no. 6, pp. 1774–1785, 1997.
- [96] —, “Asymptotically dense spherical codes. ii. laminated spherical codes,” *IEEE Transactions on Information Theory*, vol. 43, no. 6, pp. 1786–1798, 1997.
- [97] L. Gammaitoni, P. Hänggi, P. Jung, and F. Marchesoni, “Stochastic resonance,” *Reviews of modern physics*, vol. 70, no. 1, p. 223, 1998.
- [98] K. Sri Harsha, Z. Xuan, and C. Shantanu, “Energy-dissipation limits in variance-based computing,” vol. 17, no. 02. World Scientific, 2018, p. 1850013.
- [99] K. Aono, N. Lajnef, F. Faridazar, and S. Chakrabartty, “Infrastructural health monitoring using self-powered internet-of-things,” in *2016 IEEE international symposium on circuits and systems (ISCAS)*. IEEE, 2016, pp. 2058–2061.
- [100] H. Hasni, A. H. Alavi, P. Jiao, N. Lajnef, K. Chatti, K. Aono, and S. Chakrabartty, “A new approach for damage detection in asphalt concrete pavements using battery-free wireless sensors with non-constant injection rates,” *Measurement*, vol. 110, pp. 217–229, 2017.
- [101] S. K Aono, “Self-powered sensors to facilitate infrastructural internet-of-things for smart structures,” in *The 13th International Workshop on Advanced Smart Materials and Smart Structures Technology*, 2017.
- [102] S. H. Kondapalli, O. Pochettino, K. Aono, and S. Chakrabartty, “Hybrid-powered internet-of-things for infrastructure-to-vehicle communication,” in *2018 IEEE 61st International Midwest Symposium on Circuits and Systems (MWSCAS)*. IEEE, 2018, pp. 1000–1003.
- [103] O. Pochettino, S. H. Kondapalli, K. Aono, and S. Chakrabartty, “Real-time infrastructure-to-vehicle communication using rf-triggered wireless sensors,” in *2019 IEEE 62nd International Midwest Symposium on Circuits and Systems (MWSCAS)*. IEEE, 2019, pp. 556–559.

Vita

Sri Harsha Kondapalli

Degrees	Ph.D., Electrical and Systems Engineering, Washington University in St. Louis, Missouri, USA, Nov 2020 M.S., Electrical and Systems Engineering, Washington University in St. Louis, Missouri, USA, Aug 2017 B.Tech., Electrical Engineering, Indian Institute of Technology, Hyderabad, India, May 2014
Professional Memberships	The Institute of Electrical and Electronics Engineers (IEEE) IEEE Council on RFID IEEE Sensors Council IEEE Vehicular Technology Society AARL The National Association of Amateur Radio
Publications	<u>Journal Publications:</u> K. Sri Harsha , et. al. “Sub nanowatt Ultrasonic Bio Telemetry using B-scan Imaging.” <i>submitted to IEEE Open Journal of Engineering in Medicine and Biology</i> . K. Sri Harsha , et. al. “High dimensional Variance based Computation.” <i>Engrxiv</i> , 2019. Z. Liang, K. Sri Harsha , et. al. “Desynchronization of Self-powered FN Tunneling Timers for Trust Verification of IoT Supply-chain.” <i>IEEE Internet of Things Journal</i> , vol. 6, no. 4, 2019. K., Sri Harsha , et. al. “Feasibility of Self-powering and Energy Harvesting using Cardiac Valvular Perturbations.” <i>IEEE Transactions on Biomedical Circuits and Systems</i> , vol. 12, no. 6, 2018.

K. Sri Harsha, et. al. “Energy-Dissipation Limits in Variance-Based Computing.” *Fluctuation and Noise Letters*, 1850013, vol. 17, no. 2, 2018 .

K. Sri Harsha, et. al. “Multiaccess in vivo biotelemetry using sonomicrometry and M-scan ultrasound imaging.” *IEEE Transactions on Biomedical Engineering*, vol. 65, no. 1, pp. 149-158, 2018.

Z. Liang, **K. Sri Harsha**, et. al. “A Fowler-Nordheim Integrator Can Track the Density of Prime Numbers.” *arXiv*, arXivID:1711.11032, 2017.

Conference Publications:

K. Sri Harsha, et. al. “Software-Defined Radio based Interrogator for Infrastructure-to-Vehicular Communication.” *GNU Radio Conference, Huntsville, AL, USA, 2019*.

K. Sri Harsha, et. al. “Long-term, Time-synchronized Temperature Monitoring using Self-Powered CMOS Timers.” *Proceedings of 62nd IEEE International Midwest Symposium on Circuits and Systems, Dallas, USA, 2019*.

Pochettino, Owen, **K. Sri Harsha**, et. al. “Real-time Infrastructure-to-Vehicle Communication using RF-Triggered Wireless Sensors.” *Proceedings of 62nd IEEE International Midwest Symposium on Circuits and Systems, Dallas, USA, Aug 2019*.

K. Sri Harsha, et. al. “Embedded H-gauge with Hybrid-Powered Sensors for Pavement Monitoring.” *Proceedings 9th International Conference on Structural Health Monitoring of Intelligent Infrastructure, St. Louis, USA, Aug 2019*.

M. Darshit, **K. Sri Harsha**, et. al. “Zero-powered Dynamic Authentication based on Quantum Tunneling Timers.” *NSF Cybersecurity Research Transition to Practice Workshop, Chicago, USA, May 2019.*

P. Owen, **K. Sri Harsha**, et. al. “Viability of RF-triggered Embedded Sensors for Infrastructure-to-Vehicular Communication.” *IEEE International Conference on RFID, Phoenix, AZ, USA, Apr 2019.*

K. Sri Harsha, et. al. “Hybrid-Powered Internet-of-Things for Infrastructure-to-Vehicle Communication.” *Proceedings of 61st IEEE International Midwest Symposium on Circuits and Systems, Windsor, Canada, Aug 2018.*

A. Kenji, **K. Sri Harsha**, et. al. “Self-powered Sensors to Facilitate Infrastructural Internet-of-Things for Smart Structures.” *ANCRiSST 13th International Workshop on Advanced Smart Materials and Smart Structures Technology, Tokyo, Japan, July 2017.*

K. Sri Harsha, et. al. “Variance-based digital logic for energy harvesting Internet-of-Things.” *IEEE International Symposium on Circuits and Systems, Baltimore, USA, May 2017.*

Jan 2021